Experience-dependent information processing in biological systems

Maria Sol Vidal Saez

TESI DOCTORAL UPF / 2024

DIRECTORS DE LA TESI:
Jordi García Ojalvo
Óscar Vilarroya Oliver

Department of Medicine and Life Sciences
Dynamical Systems Biology Lab

upf. Universitat
Pompeu Fabra
Barcelona

Agradecimientos

En primer lugar, me gustaría agradecerle a mi director, Jordi. Este camino no podría haberlo hecho sin él. Gracias por haberme enseñado tanto estos tres últimos años. Gracias por confiar en mí, por tenerme tanta paciencia y transmitirme la confianza que me falta en muchas ocasiones. También quiero agradecer a mi co-director, Óscar. Gracias por ayudarme en este camino con una mirada que enriqueció infinitamente el desarrollo de la tesis. Quiero agradecerle a Rosa por la colaboración en el proyecto de habituación. Gracias por estar siempre disponible para intercambiar ideas y por todo lo me enseñaste en el trayecto final de esta tesis.

Gracias al DSB lab: Alda, Maria, Pablo, Gabriel, Keith, Cristina, Niv y Pau. Gracias por todas las discusiones científicas y por todos los cafés para charlar de la vida. No podría haber pedido un mejor grupo para compartir todos los días. Mención especial para la sisterhood por el aguante emocional incondicional. Agradezco haber transitado juntas esta experiencia del PhD.

A mi familia barcelonesa: Caro, Pachu, Pato, Lei, Lou, Sebi y Lu. Con ustedes la vida en Barcelona es mucho más linda y divertida. Gracias por todas las salidas y viajes en familia. Los quiero un montón.

A mis amigas que me acompañan desde Argentina: Pau, Iaru, Veru, Tami, Jules (desde EEUU), Aylu, Gri y Nati. Gracias por estar desde siempre. Ya tenemos más años vividos juntas que sin conocernos. A mis amigos de la facu: Cande, Mati, Tomi, Facu, Agus, Fer y Lean. Agradezco tener amigxs tan geniales e incondicionales siempre.

Gracias a mi familia: vieja, gordo y Cande. Gracias por el apoyo incondicional a la distancia. Son mi sostén incondicional. A mi abuela Alicia y a mi tía Betty. A mis tías Vale y Vir, gracias por el apoyo incondicional y por darme a mis primos tan hermosos. A mi tía Tata y a mi prima Guadi. A la familia Leglise por haberme adoptado como una más.

Gracias Seba, mi compañero incondicional. Gracias por estar siempre. Haber crecido juntos es uno de los regalos más lindos de esta vida.

Gracias a todos los que me acompañaron en esta increíble aventura.

Abstract

Organisms need to integrate its previous experience with its current internal state in order to deliver a suitable response to dynamic changes in their environment. This thesis is devoted to analyze, using a mathematical and computational approach, a variety of experience-dependent aspects of biological computation from a mechanistic point of view. To do so, we have examined three dynamical behaviors at different biological scales. First, we developed different models of habituation, which exhibit all hallmarks related to the habituation response to a single stimulus. Our models are based on common cellular regulatory circuit architectures, therefore providing conceptual insight on learning at the single-cell level. Second, we studied the memory encoding capability of the gene regulatory network of *Escherichia coli* within the framework of reservoir computing. We explored its temporal information processing capabilities from a dynamical approach, focusing on the relevance of the network's local topology. Finally, we used a long-standing collection of elegant experiments to develop a salt chemotaxis model in the roundworm *Caenorhabditis elegans*. Our model integrates the molecular, cellular and organismal levels to reproduce the experimentally observed experience-dependent behavior, where worms migrate up or down the gradient depending on the salt concentration alongside they were previously fed. Together, these studies intend to offer insight on the mechanisms, from the molecular to the behavioral, underpinning the ability of living systems to respond to diverse environmental temporal contexts.

Resumen

Los organismos necesitan integrar su experiencia previa con su estado interno actual para ofrecer una respuesta adecuada a los cambios dinámicos en su entorno. Esta tesis se dedica a analizar, desde un enfoque matemático y computacional, diversos aspectos dependientes de la experiencia de la computación biológica desde un punto de vista mecanicista. Para ello, hemos examinado tres comportamientos dinámicos en diferentes escalas biológicas. En primer lugar, desarrollamos diversos modelos de habituación que exhiben todas las características relacionadas con la respuesta de habituación a un único estímulo. Nuestros modelos se basan en arquitecturas comunes de circuitos reguladores celulares, proporcionando así una comprensión conceptual del aprendizaje a nivel de células individuales. En segundo lugar, estudiamos la capacidad de codificación de memoria de la red de regulación genética de *Escherichia coli* dentro del marco de *reservoir computing*. Exploramos sus capacidades de procesamiento de información temporal desde un enfoque dinámico, así como también centrándonos en la relevancia de

la topología local de la red. Finalmente, utilizamos una serie de elegantes experimentos para desarrollar un modelo de *chemotaxis* en gradientes de sal por parte del nematodo *Caenorhabditis elegans*. Nuestro modelo integra los niveles molecular, celular y del organismo para reproducir las observaciones experimentales, donde los gusanos migran hacia arriba o hacia abajo en el gradiente dependiendo de la concentración de sal a la que fueron alimentados previamente. En conjunto, estos estudios pretenden contribuir al conocimiento sobre los mecanismos, desde los moleculares hasta los conductuales, que sustentan la capacidad de los sistemas vivos para responder a diversos contextos ambientales temporales.

Contents

List of Figures

List of Tables

Chapter 1. Introduction

1.1   Motivation and objectives

Biological systems, ranging from single cells to complex organisms, rely heavily on their ability to process temporal information for survival, adaptation, and optimal functioning. Temporal information processing ensures that biological activities are coordinated in time, allowing for precise responses to dynamic environmental changes. This temporal sensitivity is crucial for various aspects of life, and the presence of memory mechanisms further enhances the adaptability and efficiency of biological systems.

To have a broader picture on the understanding of decision making and behavior we need to consider that organisms orchestrate a biological response to a specific context/situation, but that this response can change accordingly to its previous experience. In other words, in a myriad of situations organisms need to integrate its previous experience with its current internal state in order to deliver a suitable response. In this sense, this thesis is devoted to study these experience-dependent aspects of biological computation from a mechanistic point of view.

We have examined three different biological paradigms at different scales, but in all cases our focus was on the temporal information processing mechanisms. We first examined one of the simplest example of non-associative learning, *i.e.*, habituation. In spite of its simplicity, habituation inherently involves information processing and time perception capabilities, as we will discuss later. In this case, we developed biochemically plausible models, based on enzymatic reactions. We focused on the different architectures that can give rise to a series of known hallmarks of habituation. Our models consisted in minimal circuits made of feedforward and/or feedback building block motifs.

After having analyzed the contribution of a low number of recurrences to the temporal information processing capabilities in the context of habituation, we moved to a system where global feedback is present. We analyzed

memory encoding in the gene regulatory network (GRN) of *Escherichia coli* in the framework of reservoir computing. The GRN we studied has a highly recurrent core, which is fundamental to encode the organism's previous experience.

Finally, we studied the effect of feedback on temporal information processing from a more integrative perspective. To that end, we developed a model of the experience-dependent behavior of chemotaxis in the roundworm *Caenorhabditis elegans*. We use this model to propose and validate, in comparison with experimental observations, the adaptive foraging behavior of the worm in a gradient of salt. Here, the feedback is present as a sensorimotor feedback.

In the following, we will introduce from a broad perspective each one of the topics that we have studied. Then, we will finish this chapter by explaining the thesis structure.

1.2 Learning

The capacity to perceive and adapt to environmental changes stands out as a fundamental characteristic of living organisms. In specific instances, the response to an environmental stimulus may not be solely dictated by the stimulus itself but could also be influenced by the organism's prior experiences. This –a persistent change in response to the same stimulus based on experience– can be considered a basic definition of learning [1].

Two primary forms of learning are commonly identified: associative learning, exemplified by Pavlovian conditioning, and non-associative learning, including habituation and its counterpart, sensitization. In this thesis we specifically concentrate on habituation, characterized by a reversible reduction in response after repetitive stimulation (see Fig. 1.1A). The importance of habituation lies in its capacity to filter out non-harmful and irrelevant information, enabling organisms to conserve resources for more critical cognitive or cellular activities [2]. Thompson and Spencer [3] reviewed an extensive collection of experiments in neuronal organisms to compile a list of ten common characteristics displayed by most, but not necessarily all, habituating organisms. Its minor revision more than 50 years later by Rankin and colleagues [2] not only provided the most up-to-date definition of habituation, but also represents a general consensus in psychology and neurobiology (see Table 1.1). Even though these ten hallmarks of habituation have been crystallized from behavioral research, it is important to note that their definition is operational, and can thus be applied to any organism with the ability to transiently respond to individual stimuli.

#	Name	Description
1	Habituation	Repeated application of a stimulus results in a progressive decrease in some parameter of a response to an asymptotic level.
2	Spontaneous recovery	If the stimulus is withheld after response decrement, the response recovers at least partially over the observation time.
3	Potentiation of habituation	After multiple series of stimulus repetitions and spontaneous recoveries, the response decrement becomes successively more rapid and/or more pronounced.
4	Frequency sensitivity*	Other things being equal, more frequent stimulation results in more rapid and/or more pronounced response decrement, and more rapid spontaneous recovery (if the decrement has reached asymptotic levels).
5	Intensity sensitivity	Within a stimulus modality, the less intense the stimulus, the more rapid and/or more pronounced the behavioral response decrement. Very intense stimuli may yield no significant observable response decrement.
6	Subliminal accumulation*	The effects of repeated stimulation may continue to accumulate even after the response has reached an asymptotic level [...]. This effect of stimulation beyond asymptotic levels can alter subsequent behavior, for example, by delaying the onset of spontaneous recovery.
7	Stimulus specificity*	Within the same stimulus modality, the response decrement shows some stimulus specificity.
8	Dishabituation	Presentation of a different stimulus results in an increase of the decremented response to the original stimulus.
9	Habituation of dishabituation	Upon repeated application of the dishabituating stimulus, the amount of dishabituation produced decreases.
10	Long-term habituation	Some stimulus repetition protocols may result in properties of the response decrement [...] that last hours, days or weeks.

Table 1.1: **Hallmarks of habituation [2]**. The hallmarks investigated in this work are highlighted in grey. Asterisks denote that the naming has been changed by us.
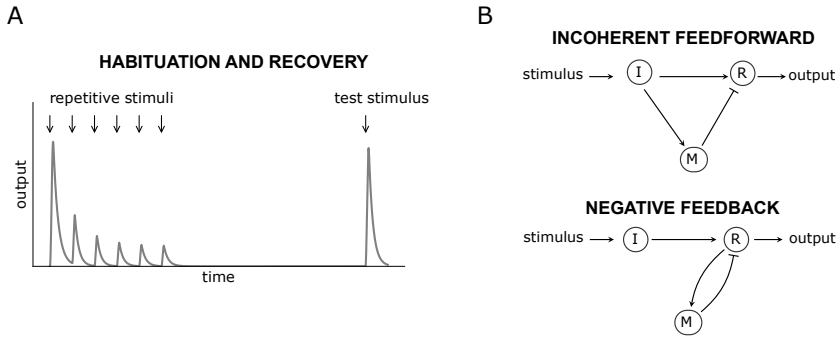
Figure 1.1: **Scheme of habituating behavior.** (A) Exemplary response curve of habituation in response to repetitive stimulation (hallmark #1 in Table 1.1). The response recovers after the stimulus is withheld for some time (hallmark #2 in Table 1.1). (B) The incoherent feedforward and the negative feedback motifs.

Habituation transcends being merely an artifact of sensory/motor fatigue or a cellular depletion mechanism. This is typically illustrated by employing various types of stimuli and checking stimulus specificity [2, 3] (hallmark #7 in Table 1.1). This refers to the fact that within the same stimulus modality, the response decrement (habituation) shows some stimulus specificity. In contrast, if habituation was a more general sensory adaptation or motor fatigue, then it should generalize across a broad range of stimuli within a sensory modality, which is not the case.

A remarkable characteristic highlighting the subtle information processing and time perception inherent in habituation is **frequency sensitivity** (hallmark #4 in Table 1.1), wherein habituation and the subsequent recovery (hallmarks #1 and #2 in Table 1.1, see also Fig. 1.1A) occur more rapidly with more frequent stimulation. This phenomenon implies that habituating organisms assess the significance of a stimulus not solely based on the number of previous stimuli but also gather information about its environmental context. The environment is less likely to change in between two closely spaced stimuli, making it reasonable to disregard a non-harmful stimulus after a brief period of time. Following the same rationale, the absence of stimuli after frequent stimulation leads to a quick recovery [4]. Similarly, it is less dangerous to disregard weaker stimuli, elucidating why habituation occurs faster for less intense stimuli. This constitutes another pivotal characteristic known as **intensity sensitivity** (hallmark #5 in Table 1.1).

While there are instances of associative [5, 6] and habituation-like [7, 8] learning observed in plants, the attribution of learning has predominantly been limited to networks of neurons within nervous systems, particularly

in brains [9]. In these cases, learning has been demonstrated to coincide with alterations in gene expression within the implicated neurons [10]. For instance, the marine slug *Aplysia californica* is a species that, due to its low number of large neurons, has served as a model organism for habituation studies. In *Aplysia*, the long-term habituation of the gill-withdrawal reflex depends on the synthesis of new proteins in the presynaptic neuron, but also involving postsynaptic processes [9]. This stands in sharp contrast to short-term habituation, which is linked to the habituation of neurotransmitter release in the sensory neuron, and is thus exclusively a presynaptic process [11]. This discovery has been corroborated in species other than *Aplysia* [12, 13]. These molecular events suggest that the computations relevant for short-term habituation occur within the sensory neuron—a single cell.

The primary evidence of learning within single cells arises from experimental studies involving unicellular organisms and mammalian cell tissues [14]. Early investigations into classical conditioning in the ciliates *Paramecium aurelia* and *Paramecium caudatum* were conducted in the 1950s and 1970s [15, 16]. Beatrice Gelber executed experiments in which *Paramecia* underwent training through repetitive exposure to a needle coated with bacteria. Following numerous trials, *Paramecium* displayed a swimming response toward the needle, now established as the conditioned stimulus, even in the absence of bacteria. Gelber's experiments are notable not just for their scientific contributions but also for their historical importance, since their controversial perception demonstrates the challenges faced by her and others exploring the unconventional realm of studying learning outside the brain [17, 18]. More recently, the list of organisms exhibiting associative learning has broadened to include *Amoeba proteus* and *Metamoeba leningradensis* [19].

The documentation of non-associative learning in single cells is comparably abundant. Herbert Spencer Jennings conducted studies on *Stentor roeseli*, a trumpet-shaped, sessile ciliate. With repeated irritation, *Stentor* undergoes a hierarchical progression of avoidance reactions, escalating in intensity until it eventually detaches from its holdfast and swims away [20]. This can be regarded as a type of non-associative learning, where behavior undergoes changes in response to a single stimulus. However, this process is more complex than habituation or sensitization, as the organism opts for a different course of action rather than modifying the same behavior in a varied manner. Despite initial skepticism and inadequately executed attempts to refute Jennings' findings, they have recently been effectively replicated [21].

Of particular relevance to our work, habituation has been documented in various single-celled organisms, including the ciliate *Stentor coeruleus* [22, 23] and the slime mold *Physarum polycephalum* [24]. Additionally, it has been observed in non-neuronal mammalian tissue cells, such as human embryonic kidney cells [25] and the rat adrenal pheochromocytoma cell line PC12, where detailed investigations were conducted by Daniel Koshland's group in the 1990s [26, 27]. These cells display habituation of noradrenaline (a neurotransmitter) release upon a variety of repetitive stimuli, including acetylcholine (ACh) [26, 28, 29, 30, 31], high levels of potassium [26, 30], and ATP [27, 29]. Koshland's studies have ruled out the possibility of a simple depletion mechanism by correcting for the loss of internal neurotransmitter during the experiment. The stimulus specificity observed between potassium and acetylcholine [28], along with dishabituation (hallmark #8 in Table 1.1) to phorbol esters (with potassium as stimuli) [26], further allow the exclusion of fatigue as a potential explanation.

From the biochemical examination of PC12 cells, we understand that the habituation of noradrenaline release is a downstream effect of the habituation of internal calcium levels [27, 32]. The existing data for ATP stimulation suggests that this phenomenon may arise from the downregulation of calcium influx through inactivation of the ATP-gated cation channels [27]. However, it is noteworthy that distinct stimuli might engage different pathways, as evidenced by the independence of habituation produced by potassium and acetylcholine stimulation [28, 30]. The pathway activated by potassium stimulation has been proposed to involve voltage-gated calcium channels and protein kinase C [26]. Despite these insights, the comprehensive circuit underlying habituation in PC12 cells has not been meticulously elucidated.

In this sense, developing a theoretical understanding of the general mechanistic principles governing habituation could further aid the search for biochemical mechanisms. From a conceptual point of view, habituation can be implemented by a network including a memory-encoding molecular species, which builds up either proportionally to the input or the response node and has an inhibitory effect on the latter. This corresponds to an incoherent feedforward (IFF) or a negative feedback (NF) loop, respectively (see Fig. 1.1B). The memory-encoding molecule stores information about previous stimulation and accounts for the decrease in response through its inhibitory effect on the response node. While it is relatively easy to construct a model for habituation and recovery, it is not trivial to account for the hallmarks of frequency and intensity sensitivity (hallmarks #4 and #5 in Table 1.1).

The IFF and NF network motifs are ubiquitous in nature [33] and therefore

provide plausible building blocks for models on the cellular level. They have been shown to underlie adaptation; a phenomenon in which a persistent stimulus results in an initial increase in response followed by a subsequent decay back to the original steady state level [34, 35]. Adapting network topologies are a valuable source for the construction of habituating models. Detailed models of adaptation have been proposed in enzymatic [36] and gene regulatory [37] contexts. One of the earliest studied adapting systems is the chemotaxis of *Escherichia coli*, which has been shown to rely on the NF motif, with the inhibitory memory being implemented in the form of multisite post-translational modifications [18, 38].

Taking this into account, in Chapter 2 we provide a biologically plausible model of habituation on a cellular level, which accounts for the nontrivial hallmarks of frequency and intensity sensitivity. We show that concatenation of IFF or NF motifs can generate the desired behavior in a molecular setting at the level of a single cell. The ubiquity of IFF and NF motifs and the resulting generality of our model might facilitate the search for molecular substrates involved in habituation in various organisms. Elucidating the mechanisms of learning from the perspective of single cells not only enhances our understanding of the remarkable signal processing capabilities of cells, but also sheds light on the evolutionary origins of learning.

1.3 Information processing by cellular networks

The perspective taken in the previous section was focused on finding a minimal conceptual model that explains the main features of a temporal information processing-demanding behavior, *i.e.*, habituation on a cellular level. Nonetheless, regulatory circuits are often highly interconnected within the cellular machinery, forming large networks [39, 40]. This large complexity of interactions among diverse types of molecules such as DNA, RNA, proteins and metabolites is what makes the cell able to accurately adapt to the environment conditions [41, 42]. Just as large neuronal networks display emergent dynamical properties that cannot appear in individual cells or small circuits [43], we expect the dynamical properties of larger regulatory networks to be much more complex than what we can expect from the small circuit architectures.

Inspired by this possibility, in Chapter 3 we propose that cellular regulatory networks –gene regulatory networks in particular– can integrate temporal signals and encode memory in a decentralised manner, relying on the inherent structure and dynamics of the whole network, following the reservoir computing paradigm.

Reservoir computing (RC) is a computational scheme based on recurrent neural networks, where temporal computations emerge from the interaction between incoming stimuli and the internal dynamic state of the network. RC was initially articulated independently in the realms of neuroscience as *liquid state machines* [44], and in machine learning as *echo state networks* [45]. This approach seeks to combine the strengths of recurrent neural networks (RNN) and feedforward networks (FFN). By doing so, it aims to make use of the temporal information-processing advantages inherent in RNNs while employing FFNs to address and overcome RNNs' inherent limitations, such as their training process.

Feedforward networks, also known as *multi-layer perceptrons*, stand as one of the pioneering neural network architectures with applications in machine learning. Neurons, the processing elements, are structured in hierarchical layers, facilitating the unidirectional flow of information from one layer to the next (see Fig. 1.2a). This modular arrangement allows for the identification of different neuron types (input, hidden or intermediate, and output nodes), and simplifies the training process, *i.e.* the modification of the network's synaptic strengths so that the desired output is produced. Error backpropagation [46] has become the standard method for training FFNs to perform complex tasks. On the other hand, FFNs lack the capability to represent temporal structures: the system's output, derived from a given input, does not depend on preceding inputs. In essence, while these networks can be efficiently trained to process complex spatial inputs, they fall short in handling temporal information [47, 48].

Compared to FFNs, recurrent neural networks exhibit greater robustness, possess the capacity to process temporal information, and are able to model highly nonlinear systems [49]. Unlike FFNs, RNNs lack a hierarchical organization of neurons, with no topological distinctions between input, output, or intermediate nodes (see Fig. 1.2b). This absence of hierarchy results in recurrent information flow within the network, allowing virtually any node to influence any other. Consequently, RNNs behave as high-dimensional dynamical systems, where an input signal induces a complex dynamical perturbation in the current system state that reverberates and survives within the network for a while. The network's dynamics relies on both external inputs and its internal state, projecting the recent history of the network into the multidimensional space of their dynamics.

The recurrence of connections in RNNs leads in turn to a prominent drawback: the network training process becomes notably inefficient due to the potential influence of any connection on the global dynamics of the network [47]. Error backpropagation has also been extended to RNNs [50, 51], but
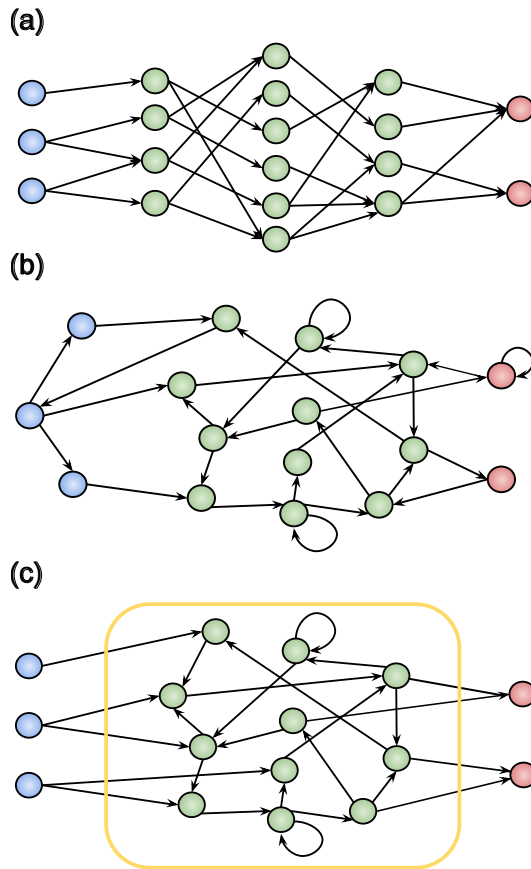
Figure 1.2: **Architectures of neural networks**. (a) Feedforward network. (b) Recurrent neural network. (c) Reservoir computing. The different types of nodes are input nodes (blue) that are the entry point of the external signals into the network, the hidden nodes (green) that are internal to the network, and the readout nodes (red) that must give the appropriate response/output of the system.

only with a partial success. Backpropagation methods for RNNs are more computationally demanding and with slower convergence than the feedforward case, and can also lead to poor local minima. Moreover, there are conceptual limitations to their applicability for RNN. One of them is that bifurcations can make training non-converging [52].

Taking this into account, training RNNs appears to be inherently challenging. On the other hand, they could be an immensely powerful and versatile tool, seamlessly blending extensive dynamical memory with highly adaptable computational capabilities. Moreover, RNNs are the most closely resembling biological networks, which tend to be connected in a highly recurrent manner.

The reservoir computing framework employs an untrained RNN as a reservoir, which is then read out by a simple classification feedforward layer (see Fig. 1.2c). A crucial prerequisite for the reservoir is to satisfy the *echo-state property*: the dynamical state of the reservoir should be uniquely defined by the fading memory of the input [53]. In other words, for a long enough input, the current state of the system should not depend on the initial conditions that were before the input. It is empirically observed that the *echo state property* is obtained for any input if the spectral radius of the network's adjacency matrix (its largest eigenvalue) is smaller than 1.

Downstream of the RNN, a purely feedforward structure is identified, which is then trained to extract pertinent information from the transient multidimensional dynamics of the reservoir. The reservoir computing paradigm offers the advantage of utilizing a RNN without the need to adapt the weights of its internal connections. Instead, only the links towards and between the strictly feedforward output layers need to be trained for learning a new task [47]. Consequently, RC significantly simplifies the training of the RNN, while maintaining its computational powers.

In Chapter 3 we made use of the above introduced reservoir computing framework in order to study the temporal computing power of *E. coli*'s GRN. Specifically, our initial exploration delved into the impact of the network dynamics on its memory capacity. Additionally, we analyzed whether the local topology of biological GRNs plays a role in their memory encoding capacity. An examination was also conducted to ascertain whether a particular balance between activation and repression is requisite to obtain a functional reservoir. Lastly, we endeavoured to identify a smaller set of genes within the *E. coli*'s network capable of performing well in memory-demanding tasks, holding potential significance for experimental validation.

1.4   Context-dependent behavior

So far we have discussed the temporal information processing capabilities of molecular circuits and networks. However, in multicellular organisms, in particular metazoans, the encoding of previous experience is also key to determine their present behavior (what we call experience-dependent behavior). In those situations recurrence also plays a central role, but from a different perspective in comparison to the previous section. Specifically, sensorimotor feedbacks are a key element to determine the organism's behavior, according to its previous history. In what follows, we introduce a specific experimental system that can be considered a paradigm of experience-dependent behavior, namely salt chemotaxis in the nematode *C. elegans*.

In some respects, modern neuroscience began with the quest for the *engram*: the physical trace of a memory in the brain. This is precisely what Eric Kandel set out to find by studying habituation in the marine slug *Aplysia*. The low number and large size of the neurons of *Aplysia* allowed Kandel to physically place electrodes into single neurons and measure their electrical activity. Contrary to the commonly held view at the time that simple organisms were incapable of complex learning, Kandel found that the the slug's gill withdrawal reflex (i.e., it closes its gill if prodded) was amenable to habituation, sensitization and associative conditioning. Using these learning paradigms in several clever experiments, Kandel successfully located the individual neurons involved in the reflex and found the *engram*: the genetic and molecular changes leading to a weakening or strengthening of the connection between two neurons, effectively holding the memory for the strength of the gill withdrawal reflex.

Since those pioneering experiments, we have learned a tremendous amount and created a very powerful set of tools to probe the mysteries of the brain. It is thus that the next big question of neuroscience can be explored: how do brains make decisions? Arguably, behind every behavior lies a decision. In the simplest case whether to perform an action or not, and in other cases a choice between many possible alternatives. Indeed, if they are to maximize their fitness, animals should weigh their options carefully, making sure they find sufficient food, mates and shelter, all while avoiding predators and hazardous environments.

To understand how a nervous system produces complex behavior, minimal organisms that show the behavior of interest are always a good starting point. In this sense, the roundworm *C. elegans* is the only species that has its complete nervous system [54], complete genome [55] and complete cell lineage mapped [56]. While this was not clear to the early pioneers, many

of the molecular, cellular and macroscopic pathways are conserved between worms and humans. Thus, the more we learn about *C. elegans*, the better we understand genetics, development, cognition and their interaction across the animal kingdom and in ourselves.

Despite its relatively simple nervous system, *C. elegans* shows experience-dependent behavioral plasticity in response to a variety of environmental cues, such as odor [57], taste [58], and temperature [59], among others. By the term "experience-dependent behavior" we mean adaptive behaviors that can change accordingly to the worm's previous history.

One of the most studied examples of this type of behavior in *C. elegans* is chemotaxis in a gradient of salt (NaCl). Salt was first identified as a chemoattractant by Ward in 1973 [60]. Its chemoattractant can be traced to the fact that NaCl (as well as other salts) tend to be present in higher concentrations around bacteria, the main food source of *C. elegans*. The response to salt has been proven to be plastic and can be reversed upon pre-exposure. Animals exposed to salt in the absence of food over time scales of ten minutes avoid NaCl at any concentration [61, 62, 63]. This form of plasticity has a reversal time of less than 5 minutes, and is called gustatory plasticity. A second form of plasticity occurs when animals are starved in the presence of NaCl over longer timescales (an hour or longer), and induces stronger avoidance responses that rely on mechanisms that are mostly independent from gustatory plasticity [58, 62, 64].

More recently, chemotaxis to NaCl of well-fed animals has been proven to be a learned behavior in *C. elegans*. Worms migrate up or down salt gradients depending on the NaCl concentration at which they have been previously fed at cultivation [65]. In other words, if a worm cultivated at a high NaCl concentration is set at a lower concentration in the middle of a salt gradient, it crawls up the gradient (top panel of Fig. 1.3). Conversely, if the worm was cultivated at a low NaCl concentration, it crawls down the gradient (bottom panel of Fig. 1.3). In Chapter 4 we present a mechanistic model, strongly grounded in multiple experimental observations at different biological scales, that captures this experience-dependent chemotaxis to NaCl exhibited by *C. elegans*.

Computational models of *C. elegans* have varied considerably in approaches. Some models have focused on the neuronal level [66] while other, high level models, have set out to account for specific behaviors; the latter class of models typically lack or include very simplistic representations of the nervous systems [67, 68]. In this thesis, we are concerned with intermediate level models that include some neuronal and neural circuit details and aim to offer explanatory and predictive power on the neural specification of be-

High salt cultivated animals

Pre-assay cultivation   **Chemotaxis assay**

High salt attraction

High [NaCl]

[NaCl]

Low salt cultivated animals

Pre-assay cultivation   **Chemotaxis assay**

Low salt attraction

Low [NaCl]
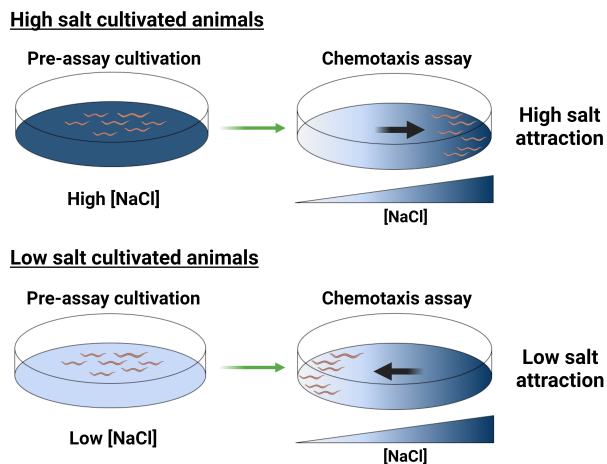
[NaCl]

Figure 1.3: **Experience-dependent salt chemotaxis in *C. elegans***. Worms are cultivated at either a high (top) or low (bottom) concentration of NaCl, then transferred to a plate with a salt gradient. High (low) salt cultivated animals are attracted to high (low) salt concentrations.

havior.

To remain grounded in physiological and behavioral evidence, intermediate-level models tend to focus on a limited subset of the nervous system. This class of models therefore distinguishes itself from models of the entire head nervous system [69], or even the entire nervous system of the animal [70] that focus instead on patterns of connectivity and circuit-level insights.

On the other hand, most intermediate-level models (focusing on specific subcircuits) have focused on a single experimental assay. This can place a significant limitation on a model's predictive power. In other words, it is likely that a model tuned to account for one assay will fail when tested on another. This also applies for models of chemotaxis on a salt gradient [71, 72, 73, 74, 75, 76]. All of these models account for *positive chemotaxis*, *i.e.*, attraction to the peak of the salt gradient. In this sense, a notable feature of our model presented in Chapter 4 is its ability to encompass both context-dependent behaviors—specifically, high- and low-salt attraction—within a unified framework. This is achieved using the same circuit without the need for altering parameter values, highlighting the versatility and adaptability of the model to account for the worm's previous experiences.

In summary, in Chapter 4 we introduce a mechanistic model, rigorously constrained by a multitude of experimental observations across various biological scales, to elucidate the experience-dependent chemotaxis toward

NaCl demonstrated by *C. elegans*. The model integrates sensory elements, spanning molecular and cellular levels, with the observed motor features of the organism's behavior. Grounded in biology, the model incorporates all experimentally identified necessary and sufficient components, steering clear of artificial regulatory mechanisms. Simultaneously, it maintains a balance by avoiding excessive molecular details that might result in over-parameterization.

1.5 Outline of the thesis

This thesis is divided into three chapters, each dedicated to an independent project that explore experience-dependent aspects of temporal information processing in biological systems. In chapter 2 we develop biochemically plausible models of habituation on a cellular level. Our models are based on enzymatic reactions, and we concentrate on the different architectures that can give rise to a series of known hallmarks of habituation.

Chapter 3 focuses on the memory encoding capability of the gene regulatory network (GRN) of *Escherichia coli* within the framework of reservoir computing. The GRN we studied has a highly recurrent core, which is fundamental to encode the organism's previous experience. In particular, we have first investigated the effect of the network dynamics in its memory capacity. Furthermore, we have looked into whether the local topology of GRNs contributes to their memory encoding. Also, we examined if certain balance between activation and repression is needed to have a functional GRN reservoir. Finally, we have sought for smaller set of genes of the *E. coli*'s network that can perform well in memory-demanding tasks, which can be of great value for experimental validation.

Lastly, in chapter 4, we developed a mechanistic model of the experience-dependent behavior of chemotaxis to NaCl exhibited by the roundworm *Caenorhabditis elegans*. The model is based on multiple experimental observations at different levels, and includes the sensory components of the process, at both the molecular and cellular levels, and the motor features of the behavior observed, at the organismal level. The model allows us to bridge the gap between well-controlled experimental observations of the response of a worm to a finite step in salt, and the observed behavior of freely moving worms in continuous gradients. Finally, in chapter 5 we summarize the main results and discuss future outlooks for the presented projects.

Chapter 2. Molecular models of habituation

The molecular bases of learning have remained elusive so far. Classical theories link learning to changes in the strengths of synapses among neurons in nervous systems [77, 78, 79]. However, recent data point to other scenarios. As we mentioned in the introduction (chapter 1), there is evidence for learning in plants [5, 7, 80], for instance. Moreover, learning-like behaviors have been observed in unicellular eukaryotes for decades [14, 15, 16, 19, 20, 21], and recent data suggests learning may occur at the level of individual neurons [81]. Therefore, it is important to understand to what extent and how learning behaviors may be implemented at the cellular level. To this end, here we investigate one of the simplest forms of learning, namely habituation.

Habituation is commonly defined as a reversible decrease in response upon repetitive stimulation (Fig. 1.1A) [3]. It allows organisms to filter out innocuous information and save their cognitive or cellular resources for more relevant tasks. Most habituating organisms share a set of characteristic features which are listed in Table 1.1 [3]. Note that most characteristics in that table involve a single stimulus, except #7, #8, #9. Two hallmarks are especially remarkable when considered together: more tightly spaced stimuli result in faster habituation and faster recovery than when stimuli are further apart (#4 **frequency sensitivity**), whereas more intense stimuli lead to slower habituation than weaker stimuli (#5 **intensity sensitivity**). These two features suggest that it is not just the amount of stimulus over a given time that matters, but that habituation involves subtle information processing and time sensing.

2.1 Modeling habituation

2.1.1 Early models

The hallmarks of habituation were crystallized from the study of habituation in neuronal organisms. However, their definition is operational and can

thus be applied to any organism with the ability to transiently respond to individual stimuli, including single cells. In fact, many of the hallmarks of habituation have been reported in single-cell organisms such as the ciliate *Stentor coeruleus* [23, 82] and *Physarum polycephalum* [24], as well as in cells in culture. Detailed studies were performed by Daniel Koshland and co-workers in the 1990s on PC12 cells [26, 27, 28, 29, 30, 31, 32, 83, 84]. Table 2.1 lists all the hallmarks observed in PC12 cells. The hallmarks #3 to #5 rely on the definition of habituation time. The list presented here is based on the (implicit) definitions used in the respective publications. For a more unified picture on the behavior of PC12 cells, a reevaluation of the presented data may be necessary.

More recently, optogenetics was used to study habituation in embryonic kidney cells [25]. Despite some molecular elements involved in the behavior were identified in some of these systems, the full biochemical mechanism has not yet been worked out in any of them.

As discussed in Chapter 1, habituation can be implemented by a simple network with an input, memory and response node, which could take the form of either an incoherent feedforward (IFF) or a negative feedback (NF) loop (Fig. 1.1B). In order to explain frequency sensitivity, Staddon and co-workers [4, 85] proposed the need for concatenating two IFF or NF motifs, so that the response of the first motif serves as the input of the second motif. Those models, however, were not molecularly realistic, as they were based on general mathematical functions, cast in the language of control theory and in a discrete time setting (in Section 2.3.1 we will discuss one of Staddon's models in more detail). Moreover, the potential for generating the rest of habituation hallmarks was unexplored. In part this has been addressed in more recent work [86, 87] but still relying on seemingly abstract models. This leaves open the question of what behaviors are possible when considering molecular interactions as substrates for habituation. Moreover, these studies do not attempt to model frequency and intensity sensitivity.

The NF and the IFF motifs are widespread in molecular networks [33]. We thus tested molecular implementations of these circuits for their ability to underlie all habituation hallmarks associated to a single stimulus (#1, #2, #3, #4, #5, #6 and #10). Indeed, we find that simple molecular implementations of these circuits can exhibit all these hallmarks. We discuss in what follows the implications of our findings for our understanding of the mechanisms and evolution of information processing and learning, from single cells to neuronal organisms.

#	Hallmarks	Stimulus	Comments
1	Habituation	K^+[26, 30] ACh[28, 29, 30] ATP[27, 29]	
2	Spontaneous recovery	K^+[26]	Only partial recovery.
		ACh[28, 29, 30] ATP[29]	Only partial recovery.
3	Potentiation of habituation	K^+[26]	
		ACh[28, 29, 30] ATP[29]	
4	Frequency sensitivity	K^+[26]	Stronger habituation for higher frequencies. Recovery was not tested. Data has been normalized.
		ACh[28]	Normalized data. Peaks have not fully habituated. Recovery was not tested.
		ATP[27]	Normalized data. Not all peaks have habituated. For higher frequencies habituation is more pronounced and more rapid. Recovery was not tested.
5	Intensity sensitivity	ATP[27]	Normalized data (Fig. 1). Indirect evidence by analogy between habituation and adaptation (Fig. 3).
6	Subliminal accumulation		Not reported.
7	Stimulus specificity	K^+/ACh[28, 30]	K^+ and ACh habituate independently of each other (specificity).
		ATP/K^+[27]	Stimulus generalization between ATP and K^+.
8	Dishabituation	K+[26]	The drug Bay K 8644 and phorbol esters have been used as dishabituating stimuli.
		ACh[28]	Phorbol esters do NOT result in dishabituation to ACh stimuli.
9	Habituation of dishabituation		Not reported.
10	Long-term habituation		Not reported.

Table 2.1: **Reported hallmarks of habituation in PC12 cells.** The measured response variable is norepinephrine release. Tested stimuli are ACh (acetylcholine), ATP (adenosine triphosphate) and K^+ (potassium).

2.1.2   A model with two concatenated IFF motifs

Building up on Staddon's proposition that habituation may be implemented by two concatenated IFF motifs [4], we started by examining a simple molecular implementation of this architecture. The model is generally based on enzymatic reactions (interactions) among molecular species that can be in either an active or an inactive state, and that can activate each other. This can correspond, for example, to proteins in two different states of activation mediated by post-translational modifications, but other biological interpretations are possible. Figure 2.1 shows the cartoon corresponding to the concatenated IFF model.
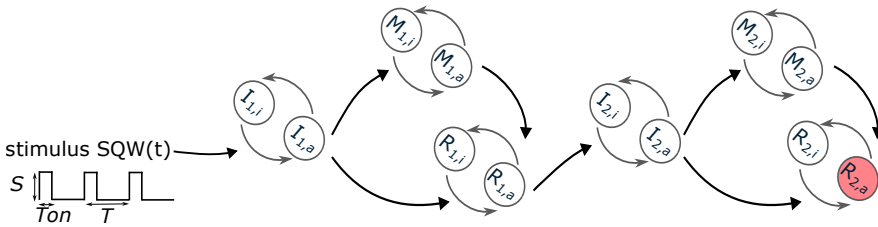
Figure 2.1: **A model with two concatenated incoherent feedforward motifs.** Cartoon of the model, where each pair of circles represents the interconversion between active (labeled with the subindex a) and inactive (labeled with the subindex i) forms of Input (I), Memory (M) and Response (R) molecular species. $R_{2,a}$, in red, is taken as the output on which the habituation hallmarks are examined. In the habituation protocol, the stimulus is simulated as a square wave input function $\text{SQW}(t)$ of period (T), and is maintained at intensity S over T_{on} time units, and at 0 otherwise. In the Appendix, the model equations are given in A.1.1, and the parameter values in Table A.2.

As shown in Fig. 2.1, each IFF motif consists of an input (I) that receives a stimulus and activates a memory species (M) and a response species (R), with the latter being deactivated by the former. The response species of the first motif serves as stimulus to the second motif. We considered all reactions to be linear and following mass action kinetics, except the deactivation of the responses, which exhibits saturation, as detailed in the Appendix A.1.1. Moreover, the total concentration of each species is assumed constant, and we explicitly model (and plot) the time evolution of the active fraction of each species. The repetitive stimulus is simulated as a square wave input function $\text{SQW}(t)$ of period T, with T_{on} time units at amplitude S, and $T - T_{on}$ time units at amplitude 0 (Fig. 2.1). The system starts at its basal steady-state with all species in their inactive form. We examine habituation on the active response species of the second motif ($R_{2,a}$).

2.2 Measures of habituation and recovery time

In order to assess the hallmarks of habituation, it is necessary to quantify how quickly the system habituates (habituation time, ht), and how long it takes for it to recover from the habituated state when the stimulus is no longer present (recovery time, rt). In what follows we define both of these measures.

2.2.1 Definition of habituation time

In agreement with the habituation definition in #1 of Table 1.1, we consider that a system has habituated when the response does not decrease significantly upon further stimulation. We formalized this by calculating the relative difference, d_i, between neighboring peaks:

$$d_i = \frac{p_i - p_{i+1}}{p_i}, \tag{2.1}$$

where p_i denotes the output response at the i-th peak. The habituation time is then defined as the number of applied stimuli applied before the relative difference d_i falls below a fixed threshold. We took the threshold to be 0.01 in general, although the sensitivity to this value was also investigated. We note that habituation time is measured in number of stimuli rather than in units of time. This provides a measure of habituation time which is independent of the stimulation period and therefore does not confound the analysis of frequency-dependent effects of habituation. Given that the hallmark of frequency sensitivity implies slower habituation when stimuli are further apart, if habituation time were just measured in units of time, habituation may require more time just because it takes more time to reach the same stimulus number. This is a simpler behavior than requiring more stimuli to reach habituation. We note that the relationship between stimulation frequency and habituation time in terms of stimulus number was originally noted in the classic habituation review by Thompson and Spencer [3], and has also been used subsequently in the literature (for instance in PC12 cells [27, 28, 32, 83, 84] and *Stentor coeruleus* [22, 23, 82, 88]). Another measure used at times in the literature is the rate of response decay upon fitting an exponential to the response peaks. In general, this definition can be problematic for two reasons. First, not all habituation data can be well approximated by an exponential function. In fact, Rankin *et al.* state that "in many cases, the decrement is exponential, but it may also be linear" [2]. Second, the exponential decay rate is strongly determined by the dynamics of the first few peaks and by how much the response decays in total while changes in later peaks are less significant. Therefore, exponential decay

rates are not informative of the habituating behavior, which is determined by the dynamics of the later peaks.

On the other hand, our simulated responses sometimes were best fit by a combination of exponentials with different rates, therefore making the measurements from that approach unclear.

2.2.2 Recovery time

In order to quantify recovery time (rt), the system is integrated without applying any stimulus, taking as initial condition the variable values at the time it is considered to have habituated. This results in a relaxation trajectory where all active species are degraded and eventually decay to zero. A single test stimulus is then applied at a specific point of the relaxation trajectory and the response peak height is compared to the height of the first peak in the habituation protocol. Recovery time is defined as the time where the test peak reaches 95% of the initial peak height. We use a binary search along the relaxation trajectory to identify this time point accurately and efficiently.

2.3 Frequency sensitivity

2.3.1 Staddon model

Habituation is defined as "a progressive decrease in some parameter of a response to an asymptotic level" that recovers upon stimulus withdrawal (Table 1.1, #1 and #2). Staddon's model [4] already exhibited this property, which we review in what follows, before going into the results shown by our model.

In 1993 Staddon [4] published a recursive, discrete-time model of habituation which should account for frequency sensitivity. The model consists of two concatenated IFF motifs so that the output of the first module serves as the input of the second motif ($R_1(t)$ in the following equations). The model equations are given by:

$$M_1(t+1) = a_1 M_1(t) + (1 - a_1)I(t),$$

$$R_1(t) = \begin{cases} I(t) - M_1(t) & \text{if } I(t) - M_1(t) > \theta_1, \\ 0 & \text{otherwise,} \end{cases}$$

$$M_2(t+1) = a_2 M_2(t) + (1 - a_2)R_1(t),$$

$$R_2(t) = \begin{cases} R_1(t) - M_2(t) & \text{if } R_1(t) - M_2(t) > \theta_2, \\ 0 & \text{otherwise.} \end{cases}$$

Here time is measured in discrete steps $t = 1, 2, 3, ...$ We have maintained the same notation of memory (M) and response (R) species used in our model (see Fig. 2.1). R_2 is taken as the output of the model. Note that in this case the input I is directly the stimulus that has a period of T time steps, with T_{on} time steps at amplitude $S = 1$, and $T - T_{on}$ time steps at amplitude 0. In Staddon's paper [4] the values of the parameters were $a_1 = 0.5, a_2 = 0.95, \theta_1 = \theta_2 = 0, T_{on} = 1$.

Reconsidering the evidence for frequency sensitivity

While the data presented by Staddon in Ref. [4] only includes two different stimulation periods ($T = 1$ and $T = 4$), we examined a broader range of periods in that model. From the replicated results shown in Fig. 2.2 two main observations can be made. First, the habituation curve suggests that habituation is more pronounced for more frequent stimulation. This aligns well with experimental evidence [2]. On the other hand, if we calculate the habituation time (based on our definition given in 2.2.1) we can see that higher stimulation frequencies lead to slower habituation. This is opposed to the frequency sensitivity expectations [2] (see hallmark #4 in Table 1.1).
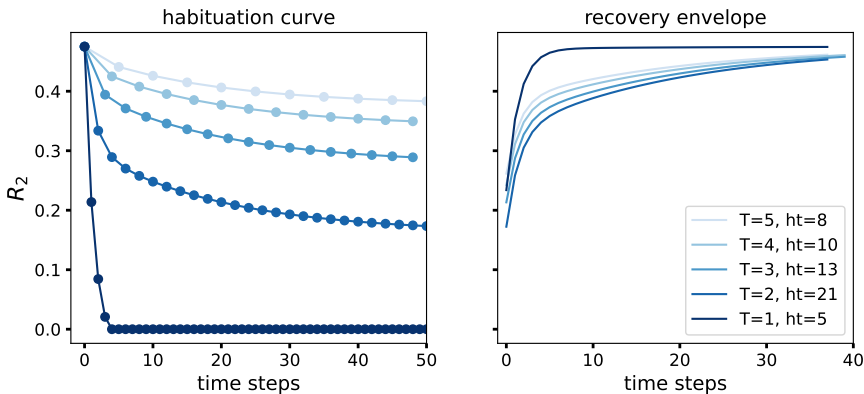
Figure 2.2: **Replication of frequency sensitivity analysis in Staddon's model [4].** Left: habituation curve. Peaks of the model's output R_2 are plotted during repetitive stimulation of different periods (T). Habituation times are calculated using the definition given in section 2.2.1. Right: recovery envelope. Value of R_2 if a test-stimulus is applied to the habituated system after letting the system relax for n time steps. The parameters are: $a_1 = 0.5, a_2 = 0.95, \theta_1 = \theta_2 = 0, T_{on} = 1$.

Second, Staddon claimed that recovery is faster for more frequent stimulation. This holds true only when comparing a stimulation period of $T = 1$ to any single other period. Except for $T = 1$ however, the data suggests that recovery is slower for higher stimulation frequencies, which contra-

dicts the frequency sensitivity hallmark. In conclusion, with the exception of $T = 1$ the general trends of habituation and recovery times are reversed in Staddon's model: more frequent stimulation result in slower habituation and slower recovery. Consequently, the model presented by Staddon [4] is insufficient to claim frequency sensitivity.

The singularity of $T = 1$ may be explained by the discreteness of the model. In a discrete-time setting $T = 1$ implies that a stimulus is applied at every time step. This might be interpreted as a persistent stimulus, which does not correspond to a true habituation protocol.

Mechanistic considerations

A second aspect that we analyzed is the mechanism that Staddon proposes to account for frequency sensitivity in his model [4]. He stated that the main feature of the model is the difference in timescales between the two motifs. Staddon proposes that the first module (peripheral unit) needs to be more rapidly decaying and "forgetful", and the second motif (central unit) should have a slower decaying memory. Following Staddon's argumentation, for high frequency stimuli, the first unit soon habituates, thus limiting the input to the second unit, which therefore habituates little. Hence, **recovery for high frequency stimuli is determined primarily by the first unit**, according to Staddon. Because this unit has more rapidly decaying memory, recovery for high frequency stimulation is rapid.

Conversely, for low frequency stimuli, the first unit has time to recover between stimuli and so they pass the first motif without significant habituation. In this case, the behavior of the system would be dominated by the second motif with its slower decaying memory, which also takes more time to recover. Therefore, **recovery after low frequency stimuli is attributable largely to the second motif and is therefore slow**, within Staddon's framework. The first module is therefore supposed to serve as a low-pass filter by decreasing its output for more frequent stimulation but letting lower frequencies pass unchanged [4].

Having said that, we analyze the memory traces of Staddon's model, which are depicted in Fig. 2.3. The figure shows the memory traces during the habituation protocol and the posterior relaxation when the stimulation is withheld. Looking at the recovery traces (second column) actually reveals that the decay of the memory species of the first motif (M_1) is much faster than that of M_2. Moreover, between the different stimulation frequencies there is almost no difference in their M_1 recovery traces. After 10 time steps M_1 has decayed to its resting value for all the stimuli frequencies
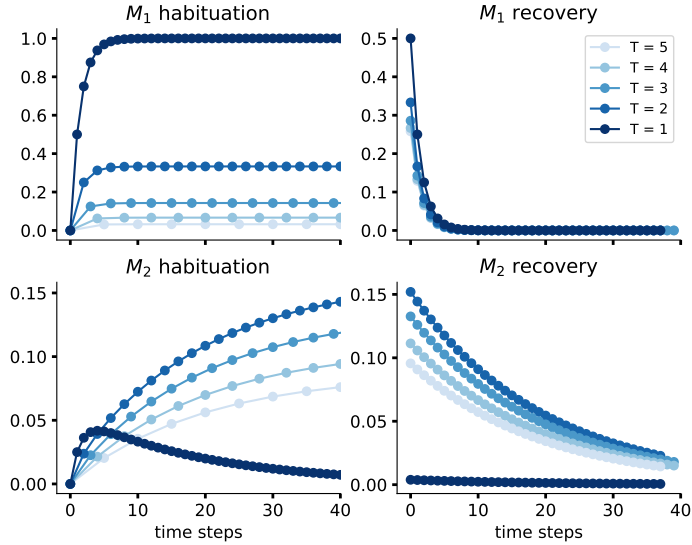
Figure 2.3: **Replication of memory traces in Staddon's model [4].** Data for the variables M_1 (top) and M_2 (bottom) during an habituation protocol (left) and subsequent recovery in the absence of stimuli (right). The parameters are: $a_1 = 0.5$, $a_2 = 0.95$, $\theta_1 = \theta_2 = 0$, $T_{on} = 1$.

considered, but the system needs more time to recover in all cases except $T = 1$ (see recovery envelope in Fig. 2.2). The response will fully recover when the M_2 levels are low enough, which takes much longer. This suggests that in Staddon's model the recovery is determined by the memory dynamics of the slower second motif regardless of the stimulation frequency, which is similar to what we found in our models in a continuous time setting, as we will see in the next section.

2.3.2   Concatenated IFF motifs

By manually choosing parameter sets and simulating the model over time in response to a pulsatile stimulus, we easily found parameter sets satisfying habituation. However, it was less trivial to obtain frequency sensitivity. For this, we searched for appropriate parameter sets and stimulation protocols using a combination of manual exploration and an evolutionary algorithm (Appendix A.3), which returned parameter sets that satisfied these hallmarks as well. The results of the best parameter set are shown in Figs. 2.4 and 2.5.

From the dynamics of the various species, the basic hallmarks of habituation can be understood to arise as follows (Fig. 2.4): upon stimulation, the first input (I_1) becomes activated in a periodic manner (Fig. 2.4, I_1). In turn,

this activates the memory (M_1), and also the response R_1. Importantly, the memory species does not completely relax in between pulses and therefore builds up during the habituation protocol (the level of M_1 reflects previous stimulation, which explains our use of the word "memory"). As a result, the response node (R_1) becomes subsequently less active in response to the input (Fig. 2.4, I_1, M_1, R_1). In turn, this decreasing periodic first response is passed as stimulus onto the second motif. Again, the second memory builds up and the output response (R_2) is progressively lower. At some point, the input received by R_2 is compensated by the inactivation by M_2 and the relative change in R_2 becomes insignificant: the system has habituated.

Figure 2.4: **Frequency sensitivity - habituation time.** Dynamics of the concatenated IFF model during the habituation protocol. The simulation starts with all species inactive, and finishes when the system is considered habituated, for different frequencies, as detailed on the depicted table. S: stimulus intensity. T: stimulus period (in units of time). ht: habituation time, in units of stimulus number. The output variable for this model is $R_{2,a}$ (second row, fourth column). Note that data is plotted as a function of stimulus number. See Appendix A.1.1 and Table A.2 for the model equations and parameter values, respectively.

Once habituated, the repressive memory species reach a non-zero level (see M_1 and M_2 plots in Fig. 2.4, or the first column in Fig. 2.5), and this causes a reduced response in comparison to the one caused by the first stimulus in the habituation protocol. Once the stimulus pulses stop, the memory levels start relaxing back to the inactive state with exponential decay (Fig. 2.5A, second column), and the response to a test stimulus increasingly grows. This is plotted in Fig. 2.5B, which depicts the recovery envelope of the system, i.e. the level of output response to a single test stimulus, applied at different post-habituation times. In Fig. 2.5A (recovery), the levels of the memory species are plotted. As can be seen, the decay of the memory species of the first motif (M_1) is much faster than that of M_2 (deactivation rate $k_{Mi1} = 0.038 \ t.u.^{-1}$ for M_1, vs $k_{Mi2} = 0.001 \ t.u.^{-1}$). This fast relaxation of M_1

causes a quick partial recovery of the response, as once the first memory has sufficiently decayed, some response can occur again (see the initial fast recovery at Fig. 2.5B). Yet, the levels of M_2 are still high enough to prevent the response from fully recovering until they decrease sufficiently, which takes much longer.
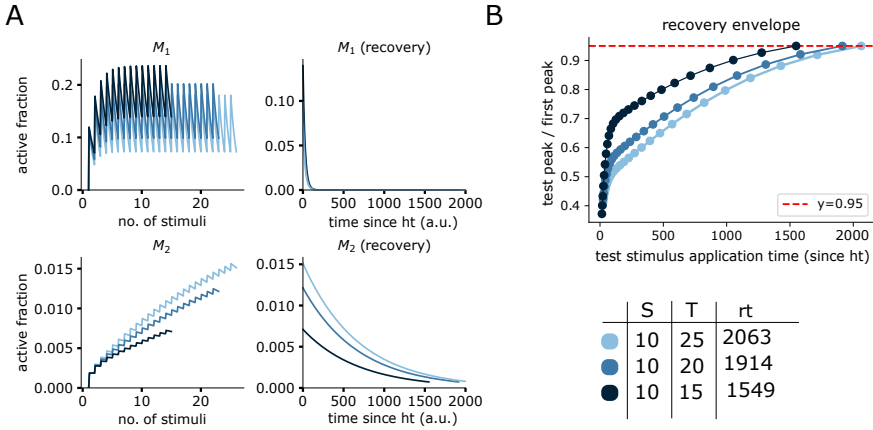
Figure 2.5: **Frequency sensitivity - recovery time.** Recovery dynamics for the concatenated IFF model. (A) Dynamics of the memory variables during the habitation protocol (first column), and during the recovery phase without stimulus (second column), for different frequencies, as detailed on the table on the right. During recovery, each memory starts at the level reached when it is first considered habituated (last point in the first column panels), and until it is considered to be recovered. Note that the data is plotted as a function of time during the recovery. (B) Recovery envelope: dynamics of the output variable $R_{2,a}$ in response to a single stimulus, applied at different post-habituation times, normalized by the height of $R_{2,a}$'s first peak during the habituation protocol. The horizontal red dashed line denotes the recovery threshold (0.95). When the recovery envelope curve crosses this line, the system is considered to be recovered. In the table the recovery time (rt) in units of time is reported for each frequency. See Appendix A.1.1 and Table A.2 for the model equations and parameter values, respectively.

As we can see from the habituation and recovery times depicted in the tables of Figs. 2.4 and 2.5, more frequent stimulation results indeed in more rapid habituation and recovery for the parameter set in question. In other words, the system is frequency sensitive.

In this sense, frequency sensitivity can be understood as arising from two features. The first one is the *separation of timescales* in the dynamics of the two memory species that we just mentioned. As for the second, we found a *reversal of memory levels* between the two motifs: under more frequent stimulation the levels of $M_{1,a}$ are higher compared to less frequent stimulation, whereas the levels of $M_{2,a}$ show an opposite trend in response. This

is because the higher levels of $M_{1,a}$ cause lower levels of the response node of the first motif (Fig. 2.4, M_1, R_1), stimulating with less intensity the second motif and therefore leading to a lower memory build up in the latter (Fig. 2.4, M_2). Given the slow timescale of the second memory species, this dominates the behavior. So, during the habituation protocol, the build-up of the memory to lower levels more rapidly compensates the activation of the output and causes faster habituation. Moreover, when the stimulus is withdrawn, the memory is at a lower initial level, so it takes less time to decay sufficiently for the response to recover (faster recovery, Fig. 2.5B). In conclusion, concatenating two IFF motifs leads to a *reversal of memory levels*, which combined with the slower dynamics of the memory in the second motif enables frequency sensitivity. We found that these two features were present also in the other good parameter sets obtained from the optimization procedure.

We note that the mechanism for frequency sensitivity proposed by Staddon relies on a separation of timescales as well. However, unlike in our model, where recovery is determined primarily by the memory dynamics of the second motif regardless of the stimulation frequency, Staddon suggested that for high frequencies the first memory species, with its fast time constant, would account for the fast recovery (see section 2.3.1). Despite this difference, we find here that concatenation of two IFF motifs can account for frequency sensitivity in a biologically plausible setting and on a continuous time-scale.

2.4   Intensity sensitivity

The same parameter set used above accounts for intensity sensitivity - the fact that stronger stimuli result in slower habituation (Fig. 2.6). In this case, the reversal of memory levels does not happen: at higher intensity, the first response (R_1) receives both a higher input (I_1) and memory (M_1), reaching higher levels of active response species (R_1) which is also passed onto the second motif. Then, the second memory levels also increase more for higher intensities. We see that this leads to more stimuli being required to reach the habituated state, as well as more time for the memory to relax and the system to recover (Fig. 2.6). It is worth remembering that intensity sensitivity comprises only slower habituation for more intense stimuli, but does not impose any condition on the recovery.
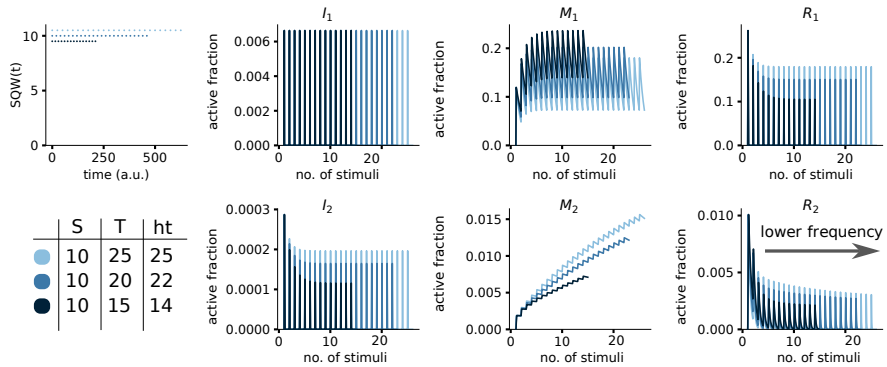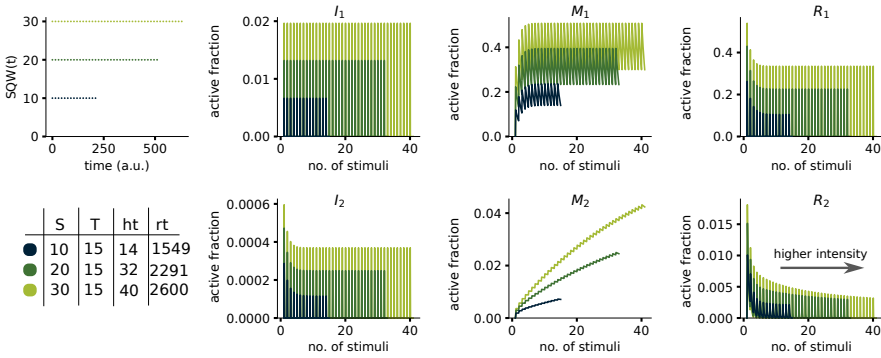
Figure 2.6: **Intensity sensitivity.** Dynamics of the concatenated IFF model during the habituation protocol. The simulation starts with all species inactive, and finishes when the system is considered habituated, for different intensities, as detailed on the left. S: stimulus intensity. T: stimulus period (in units of time). ht: habituation time, in units of stimulus number. rt: recovery time, in units of time. The output variable for this model is $R_{2,a}$ (second row, fourth column). Note that the data is plotted as a function of stimulus number. See Appendix A.1.1 and Table A.2 for the model equations and parameter values, respectively.

2.5 Potentiation and subliminal accumulation

Given these results, we decided to examine whether with the same parameter set, the system could display other hallmarks of habituation. Potentiation (hallmark #3 in Table 1.1) refers to faster habituation when a second train of stimuli is applied after initial habituation and partial recovery. To test for this, we stimulated the system until habituation, and then let it recover for a fraction of its recovery time (for the concatenated IFF this fraction was half of rt). Then we stimulated again with a train of pulses of the same frequency and intensity as the first one. A detailed explanation of the protocol to test potentiation is given in Appendix A.4. Notably, we found that the second time the habituated state was reached with less stimuli for any of the frequency/intensity settings tested previously. For the example shown in Fig. 2.7A the habituation time is $ht = 14$ for the first habituation protocol, and $ht = 10$ for the second train of stimuli. As seen in the plot, there is still a residual amount of active M_2 at the onset of the second train of stimuli, which alters the dynamics of the memory build-up and the response during the stimulation, leading to faster habituation.

A similar argument based on the levels of the memory species explains what we call subliminal accumulation (hallmark #6 of Table 1.1): when additional stimuli are applied to the already habituated system, the active fraction of M_2 keeps accumulating, which consequently needs more time to be

fully degraded when the stimulus is withdrawn. This results in slower recovery, as depicted in Fig. 2.7B. A detail explanation of the protocol to test subliminal accumulation is also given in Appendix A.4.
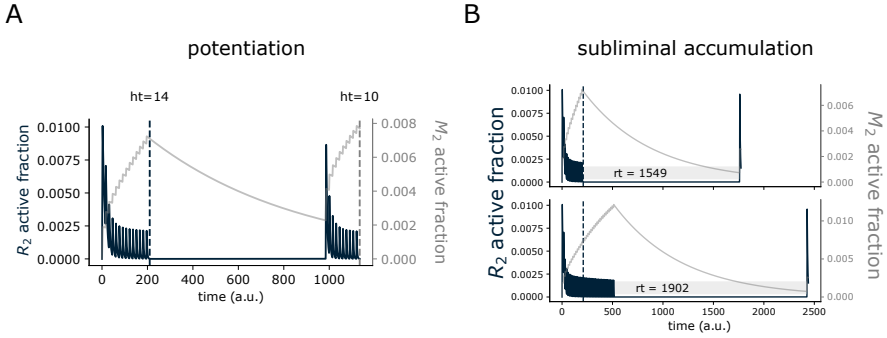
Figure 2.7: **Potentiation of habituation and subliminal accumulation.** (A) Potentiation depicted in the concatenated IFF model. The dynamics of R_2 and M_2 during periodic stimulation until habituation, recovery until half the recovery time, and subsequent re-habituation, with a stimulus of S=10, T=15. The dashed vertical lines denote the habituation time (in stimulus number). (B) Subliminal accumulation depicted in the concatenated IFF model. The dynamics of R_2 and M_2 during habituation and recovery, when the system is stimulated just until habituation (top) or beyond (bottom), which leads to a longer recovery time (rt). The stimulus period and intensity are the same as used in (A). See Appendix A.1.1 and Table A.2 for the model equations and parameter values, respectively.

2.6 Long-term habituation

We found similar results as those of the concatenated IFF model for a setup with two concatenated NF motifs (Appendix A.1.2 and Fig. 2.8). Moreover, we noticed that in both cases, recovery times could be quite long in comparison to the total time taken for the system to habituate. This was especially notable in the NF case, where we found a recovery time of ~6700 time units, in comparison to the total time required for habituation of ~60 time units. The last habituation hallmark is "long-term habituation" (hallmark #10 in Table 1.1), defined as effects lasting "hours, days or weeks". Our results suggest that our models may readily account for this hallmark as well, although given the lack of a clear threshold to consider the response "long-term" we remain cautious about this point.

two concatenated negative feedback motifs

A

frequency sensitivity - ht

B

S	T	ht	rt
15	15	21	7670
15	10	18	7312
15	5	12	6649

C recovery envelope

- - - y=0.95

D intensity sensitivity

S	T	ht	rt
10	10	15	6862
15	10	18	7312
20	10	20	7598

E potentiation

F subliminal accumulation
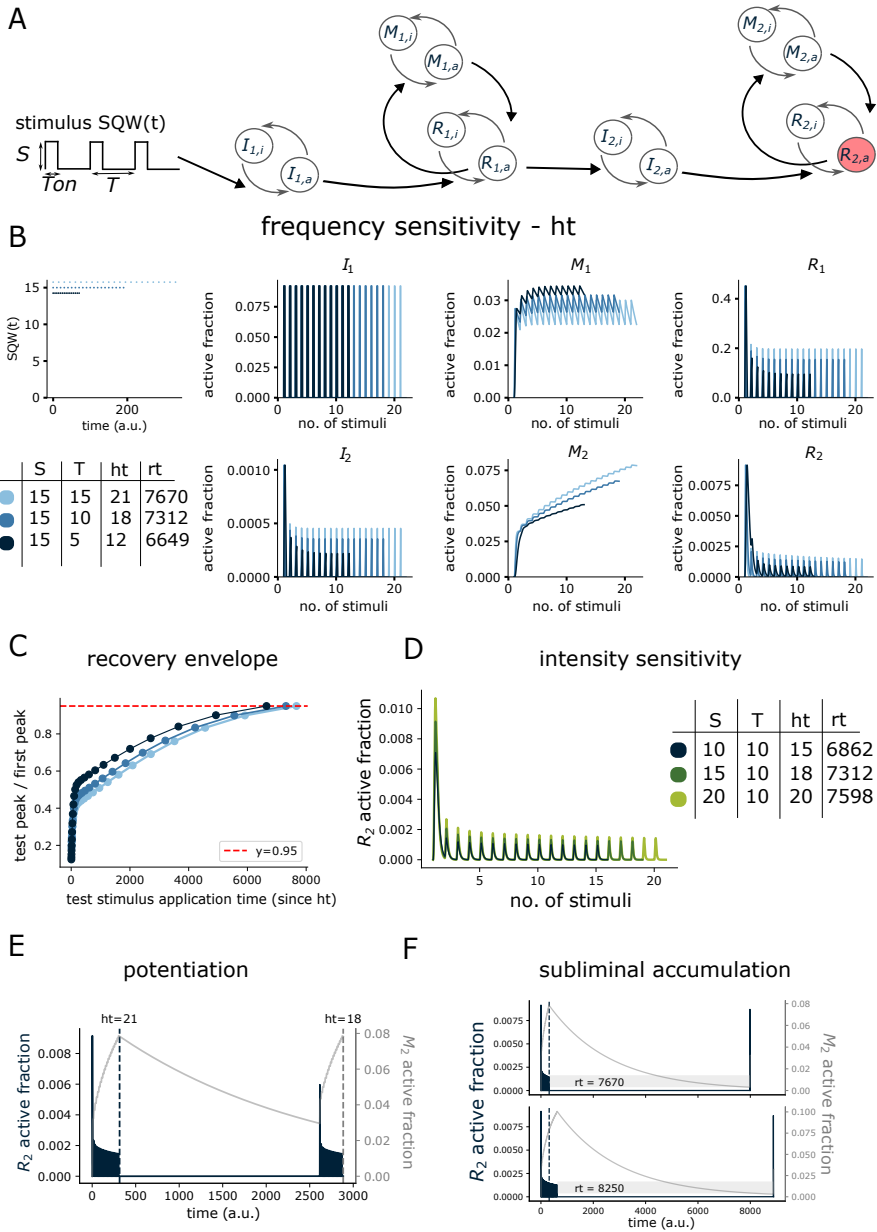
(Caption on next page.)

Figure 2.8: **Habituation mediated by two concatenated negative feedback (NF)
motifs. (A) Cartoon of the model.** Each pair of circles represents the intercon-
version between active ($_a$) and inactive ($_i$) forms of Input (I), Memory (M) and
Response (R) molecular species. $R_{2,a}$, in red, is taken as the output on which the
habituation hallmarks are examined. In the habituation protocol, the stimulus is
simulated as a square wave input function $\mathrm{SQW}(t)$ of period (T), and is main-
tained at intensity S over T_{on} time units, and at 0 otherwise. The model equations
are given in Methods, A.1.2, and the parameter values in Table A.3. **(B) Frequency
sensitivity - habituation time.** Dynamics of the model variables during the habit-
uation protocol. The simulation starts with all species inactive, and finishes when
the system is considered habituated, for different frequencies, as detailed on the
depicted table. S: stimulus intensity. T: stimulus period (in units of time). ht: ha-
bituation time, in units of stimulus number. rt: recovery time, in units of time. The
output variable for this model is $R_{2,a}$ (second row, fourth column). Note that data
is plotted as a function of stimulus number. **(C) Frequency sensitivity - recovery
time.** Recovery envelope: dynamics of the output variable $R_{2,a}$ in response to a sin-
gle stimulus, applied at different post-habituation times, normalized by the height
of $R_{2,a}$'s first peak during the habituation protocol. The horizontal red dashed line
denotes the recovery threshold (0.95). **(D) Intensity sensitivity.** Dynamics of the
$R_{2,a}$ during the habituation protocol, starting with all species inactive, and until the
system is considered habituated, for different intensities, as detailed on the right.
Note that data is plotted as a function of stimulus number. **(E) Potentiation of
habituation.** The dynamics of R_2 and M_2 during periodic stimulation until habit-
uation, recovery until a third of the recovery time, and subsequent re-habituation.
The dashed vertical lines denote the habituation time (in stimulus number). **(F)
Subliminal accumulation.** The dynamics of R_2 and M_2 during habituation and
recovery, when the system is stimulated just until habituation (top) or beyond (bot-
tom), which leads to a longer recovery time (rt). The stimulus for (E) and (F) has
S=15 and T=15.

2.7   Habituation in other architectures

2.7.1   Single motifs

As evident from the trajectories of the concatenated model in Fig. 2.4 for
the IFF motif, and Fig. 2.8 for the NF motif, the response of the first mo-
tif already shows a decrement in peak levels characteristic of habituation.
Therefore, we considered whether just a single IFF or NF motif could suf-
fice to reproduce all hallmarks. To this end, we applied the same parameter
search optimization as previously done for the concatenated models to find a
parameter set that would exhibit habituation, recovery, frequency and inten-
sity sensitivity. Despite habituation and recovery could be easily attained,
we only found parameter sets fulfilling weak intensity sensitivity, but not
frequency sensitivity. Moreover, when the best parameter set was tested for
potentiation of habituation and subliminal accumulation, these hallmarks
were much less apparent (Figs. 2.9 and 2.10). This suggests that the possi-
bility to combine different timescales and/or memory levels, as enabled by
joining together the two motifs, is key.

2.7.2   Non-identical motifs

Despite the IFF and NF architectures are frequently found in nature, they
may appear intertwined but not necessarily with two identical units con-
catenated, as considered above. Moreover, in the context of single cells,
it is very likely that the stimulus is sensed by a receptor on the cell mem-
brane. In order to account for this, we now adapt the concatenated IFF
model by replacing the first motif with a receptor/channel that can toggle
between an inactive, active, and refractory state, which cannot be activated
before returning to the inactive state (Fig. 2.11A). This 3-node receptor ar-
chitecture itself can constitute an habituating unit in which the refractory
conformation (R_r) accumulates during repetitive stimulation and consecu-
tively diminishes the fraction of inactive receptor that can become activated.
As before, we optimized parameter values and found that this model can
also account for all single-stimulus habituation hallmarks (Supplementary
Fig. 2.11). Like in the above presented models, we found a separation of
timescales between the decay of the two memory species and a reversal of
memory levels linked to frequency sensitivity.

single incoherent feedforward loop motif
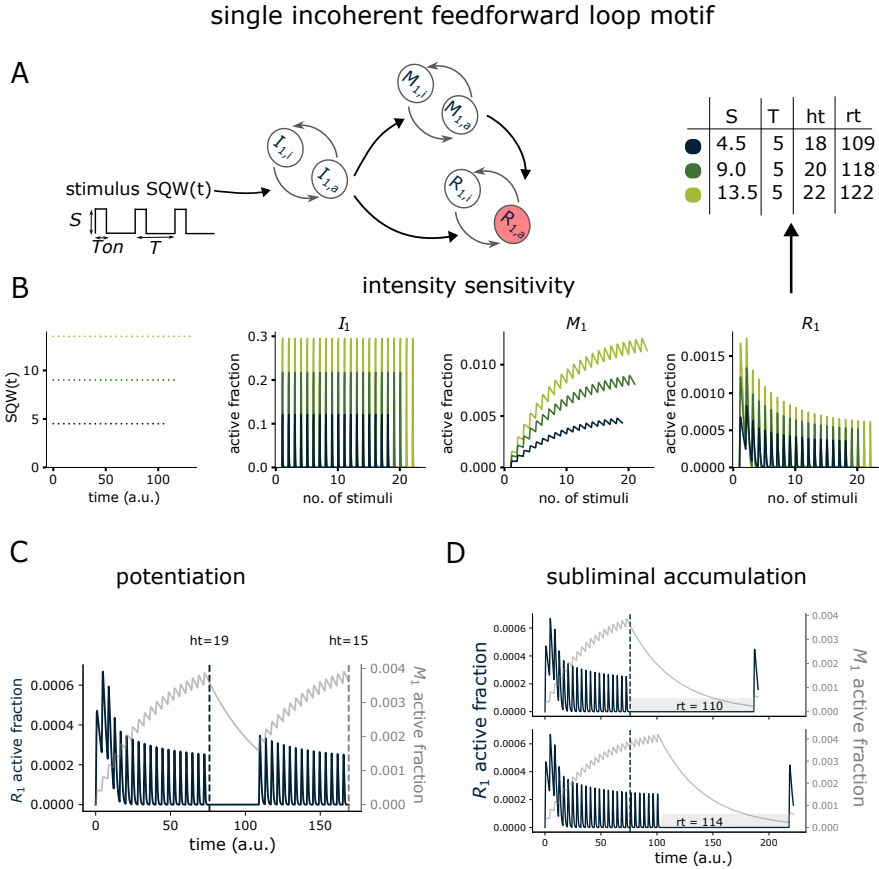
Figure 2.9: **Habituation mediated by a single incoherent feedforward loop motif. (A) Cartoon of the model.** Each pair of circles represents the interconversion between active ($_a$) and inactive ($_i$) forms of Input (I), Memory (M) and Response (R) molecular species. $R_{1,a}$, in red, is taken as the output on which the habituation hallmarks are examined. In the habituation protocol, the stimulus is simulated as a square wave input function $\mathrm{SQW}(t)$ of period (T), and is maintained at intensity S over T_{on} time units, and at 0 otherwise. The model equations are given in Methods, A.1.3, and the parameter values in Table A.4. **(B) Intensity sensitivity.** Dynamics of the model variables during the habituation protocol. The simulation starts with all species inactive, and finishes when the system is considered habituated, for different intensities, as detailed on the depicted table. S: stimulus intensity. T: stimulus period (in units of time). ht: habituation time, in units of stimulus number. rt: recovery time, in units of time. The output variable for this model is $R_{1,a}$ (fourth column). Note that data is plotted as a function of stimulus number. **(E) Potentiation of habituation.** The dynamics of R_1 and M_1 during periodic stimulation until habituation, recovery until a third of the recovery time, and subsequent re-habituation. The dashed vertical lines denote the habituation time (in stimulus number). **(F) Subliminal accumulation.** The dynamics of R_1 and M_1 during habituation and recovery, when the system is stimulated just until habituation (top) or beyond (bottom), which leads to a longer recovery time (rt). The stimulus for (C) and (D) has S=3 and T=4.
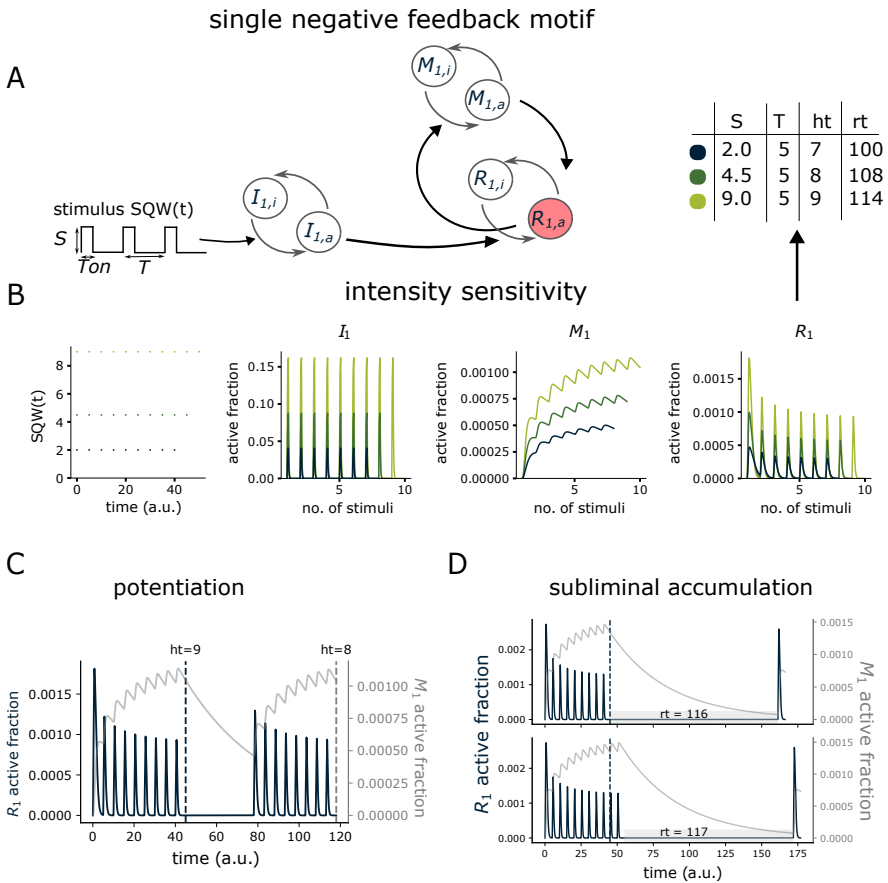
Figure 2.10: **Habituation mediated by a single negative feedback motif. (A) Cartoon of the model.** Each pair of circles represents the interconversion between active ($_a$) and inactive ($_i$) forms of Input (I), Memory (M) and Response (R) molecular species. $R_{1,a}$, in red, is taken as the output on which the habituation hallmarks are examined. In the habituation protocol, the stimulus is simulated as a square wave input function $\mathrm{SQW}(t)$ of period (T), and is maintained at intensity S over T_{on} time units, and at 0 otherwise. The model equations are given in Methods, A.1.4, and the parameter values in Table A.5. **(B) Intensity sensitivity.** Dynamics of the model variables during the habituation protocol. The simulation starts with all species inactive, and finishes when the system is considered habituated, for different intensities, as detailed on the depicted table. S: stimulus intensity. T: stimulus period (in units of time). ht: habituation time, in units of stimulus number. rt: recovery time, in units of time. The output variable for this model is $R_{1,a}$ (fourth column). Note that data is plotted as a function of stimulus number. **(E) Potentiation of habituation.** The dynamics of R_1 and M_1 during periodic stimulation until habituation, recovery until a third of the recovery time, and subsequent re-habituation. The dashed vertical lines denote the habituation time (in stimulus number). The stimulus has S=9 and T=5. **(F) Subliminal accumulation.** The dynamics of R_1 and M_1 during habituation and recovery, when the system is stimulated just until habituation (top) or beyond (bottom), which leads to a longer recovery time (rt). The stimulus has S=15 and T=5.

receptor + incoherent feedforward loop motif

A

B

frequency sensitivity - ht

S	T	ht	rt
5	25	30	3993
5	15	28	3686
5	10	24	3340

C

recovery envelope

D

intensity sensitivity

S	T	ht	rt
2	25	27	3784
5	25	30	3993
15	25	32	3984

E

potentiation

F

subliminal accumulation

(Caption on next page.)

It is common that receptors activate a cascade of signalling molecules that subsequently inactivate or downregulate the receptor. So, we last tested the "receptor + NF cascade model" (Fig. 2.12A) consisting of a three-state channel whose active species activates a cascade of (three) intracellular

Figure 2.11: **Habituation mediated by a receptor + incoherent feedforward loop motif. (A) Cartoon of the model.** The receptor can toggle between an inactive (R_i), active (R_a), and refractory (R_r) state, which cannot be activated before returning to the inactive state. For the IFF each pair of circles represents the interconversion between active ($_a$) and inactive ($_i$) forms of Input (I), Memory (M) and Response (R) molecular species. $R_{2,a}$, in red, is taken as the output on which the habituation hallmarks are examined. In the habituation protocol, the stimulus is simulated as a square wave input function $\mathrm{SQW}(t)$ of period (T), and is maintained at intensity S over T_{on} time units, and at 0 otherwise. The model equations are given in Methods, A.1.5, and the parameter values in Table A.6. **(B) Frequency sensitivity - habituation time.** Dynamics of the model variables during the habituation protocol. The simulation starts with all species inactive, and finishes when the system is considered habituated, for different frequencies, as detailed on the depicted table. S: stimulus intensity. T: stimulus period (in units of time). ht: habituation time, in units of stimulus number. rt: recovery time, in units of time. The output variable for this model is $R_{2,a}$ (second row, fourth column). Note that data is plotted as a function of stimulus number. **(C) Frequency sensitivity - recovery time.** Recovery envelope: dynamics of the output variable $R_{2,a}$ in response to a single stimulus, applied at different post-habituation times, normalized by the height of $R_{2,a}$'s first peak during the habituation protocol. The horizontal red dashed line denotes the recovery threshold (0.95). **(D) Intensity sensitivity.** Dynamics of the $R_{2,a}$ during the habituation protocol, starting with all species inactive, and until the system is considered habituated, for different intensities, as detailed on the right. Note that data is plotted as a function of stimulus number. **(E) Potentiation of habituation.** The dynamics of R_2 and M_2 during periodic stimulation until habituation, recovery until half the recovery time, and subsequent re-habituation. The dashed vertical lines denote the habituation time (in stimulus number). **(F) Subliminal accumulation.** The dynamics of R_2 and M_2 during habituation and recovery, when the system is stimulated just until habituation (top) or beyond (bottom), which leads to a longer recovery time (rt). The stimulus for (E) and (F) has S=5 and T=25.
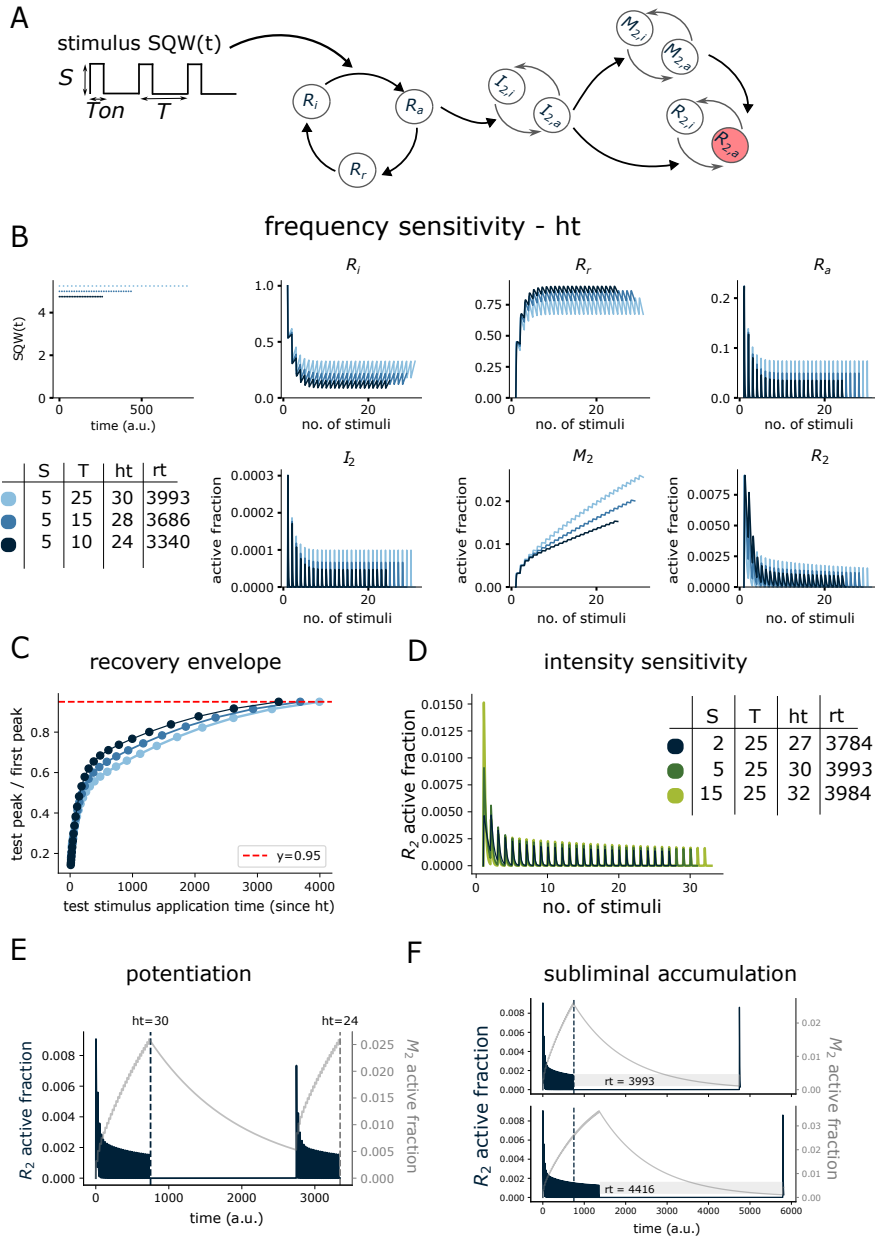
species that interconvert between an active and an inactive state. The last of the three species inactivates the receptor (negative feedback). We optimised the parameters considering as output the active receptor species (Fig. 2.12). We found again two species that accumulate during repetitive stimulation: the refractory channel species and the most downstream molecule of the cascade (C_3). Again, we also find the two features associated with frequency sensitivity: a separation of timescales among the two, and a reversal in their levels across the frequency extremes. The last species of the cascade acts as a memory that feeds back to the receptor and accelerates the inactivation of the active receptor conformation. For lower stimulation frequencies, the level of the cascade memory reaches typically higher levels (reversal), causing more peaks to be required for habituation (slower habituation) and more time for allowing a recovered response (slower recovery). Notably, the receptor-cascade model differs from the other concatenated models in that frequency sensitivity can be achieved already for the more upstream/peripheral habituating node. Moreover, for the same parameter set, we found that the hallmarks also hold when considering as output the second element in the cascade (C_2, a in red in Fig. 2.12A).
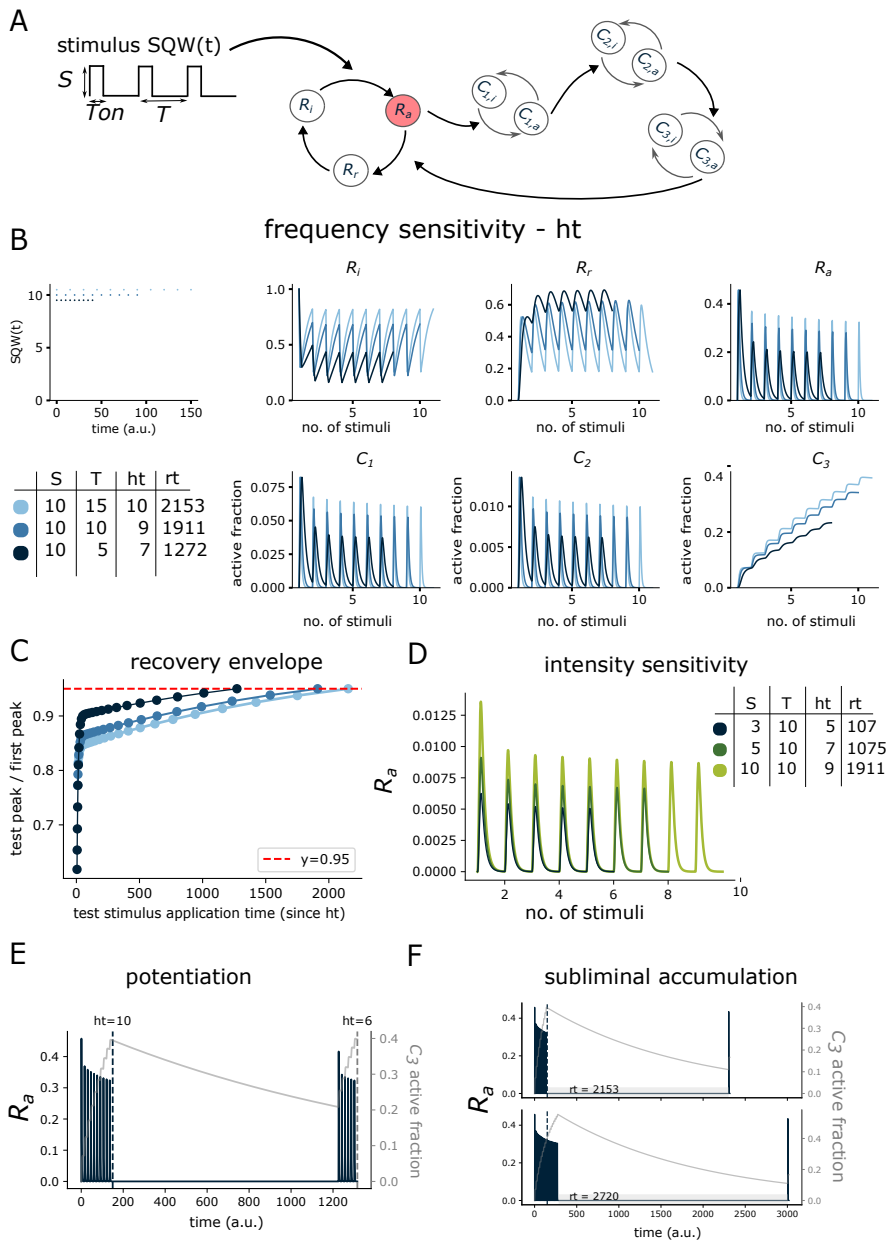
(Caption on next page.)

Figure 2.12: **Habituation mediated by a receptor + NF cascade. (A) Cartoon of the model.** The receptor can toggle between an inactive (R_i), active (R_a), and refractory (R_r) state, which cannot be activated before returning to the inactive state. R_a activates a cascade of three intracellular species that interconvert among active ($_a$) and inactive ($_i$) state. The last of the three ($C_{3,a}$) inactivates the receptor (negative feedback). For the example showed here R_a, in red, is taken as the output on which the habituation hallmarks are examined ($C_{2,a}$ was also tested as output). In the habituation protocol, the stimulus is simulated as a square wave input function $\mathrm{SQW}(t)$ of period (T), and is maintained at intensity S over T_{on} time units, and at 0 otherwise. The model equations are given in Methods, A.1.6, and the parameter values in Table A.7. **(B) Frequency sensitivity - habituation time.** Dynamics of the model variables during the habituation protocol. The simulation starts with all species inactive, and finishes when the system is considered habituated, for different frequencies, as detailed on the depicted table. S: stimulus intensity. T: stimulus period (in units of time). ht: habituation time, in units of stimulus number. rt: recovery time, in units of time. The output variable for this model is R_a (first row, fourth column). Note that data is plotted as a function of stimulus number. **(C) Frequency sensitivity - recovery time.** Recovery envelope: dynamics of the output variable R_a in response to a single stimulus, applied at different post-habituation times, normalized by the height of R_a's first peak during the habituation protocol. The horizontal red dashed line denotes the recovery threshold (0.95). **(D) Intensity sensitivity.** Dynamics of the R_a during the habituation protocol, starting with all species inactive, and until the system is considered habituated, for different intensities, as detailed on the right. Note that data is plotted as a function of stimulus number. **(E) Potentiation of habituation.** The dynamics of R_a (output) and $C_{3,a}$ (memory species that feeds back to degrade R_a) during periodic stimulation until habituation, recovery until half the recovery time, and subsequent re-habituation. The dashed vertical lines denote the habituation time (in stimulus number). **(F) Subliminal accumulation.** The dynamics of R_a and $C_{3,a}$ during habituation and recovery, when the system is stimulated just until habituation (top) or beyond (bottom), which leads to a longer recovery time (rt). The stimulus for (E) and (F) has S=10 and T=15.

2.8 Robustness of the response

2.8.1 Perturbation analysis

To assess the robustness of the response, we looked only at frequency and intensity sensitivity, given that we find the other hallmarks whenever these two appear. A first analysis consisted of performing single-parameter sensitivity analysis (see Appendix A.5.1 for details). We did this analysis for the concatenated models (IFF and NF), the receptor + IFF, and receptor + NF cascade model. We found that some parameters need to be finely tuned, as expected, but there was always some region around each parameter that could still sustain the behavior. In general, for both receptor models (Fig. 2.11A and 2.12A) the region of parameters that maintains frequency and intensity sensitivity happens to be more constrained than for the IFF and NF concatenated models (Fig. 2.1 and 2.8A). The results are displayed in Figs. 2.13, 2.14, 2.15 and 2.16 for the concatenated IFF, concatenated NF, receptor + IFF, and the receptor + NF cascade model, respectively.
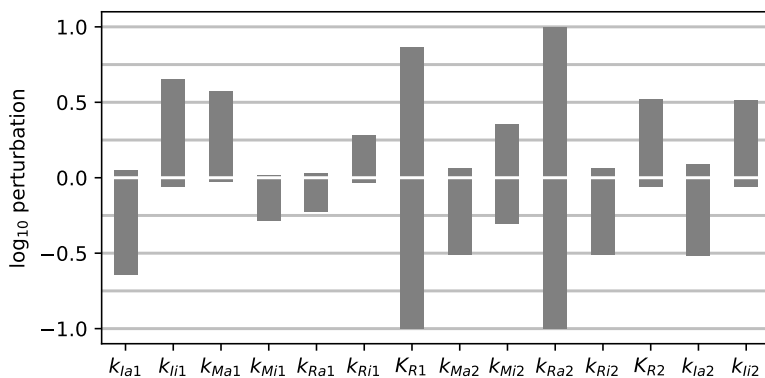
Figure 2.13: **Sensitivity analysis for the concatenated IFF model.** Analysis around the parameter set shown in Fig. 2.4. See Methods A.5.1 for details. Related to Fig. 2.1.
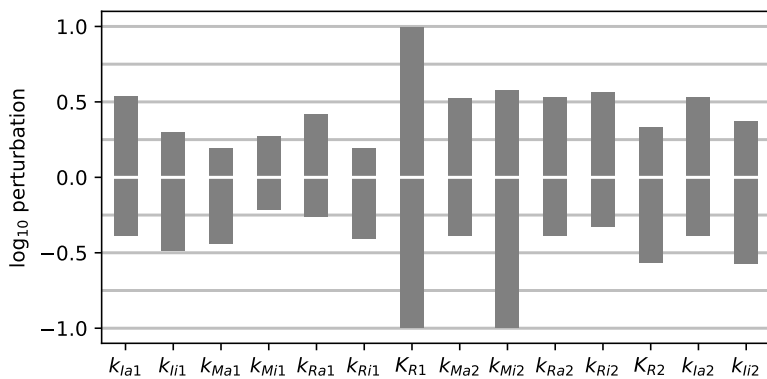
Figure 2.14: **Sensitivity analysis for the concatenated NF model.** Analysis around the parameter set shown in Fig. 2.8. See Methods A.5.1 for details. Related to Fig. 2.8A.
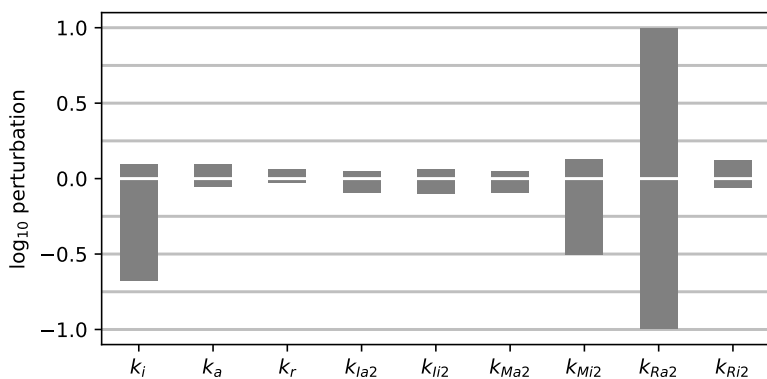
Figure 2.15: **Sensitivity analysis for the receptor + IFF model.** Analysis around the parameter set shown in Fig. 2.11. See Methods A.5.1 for details. Related to Fig. 2.11A.
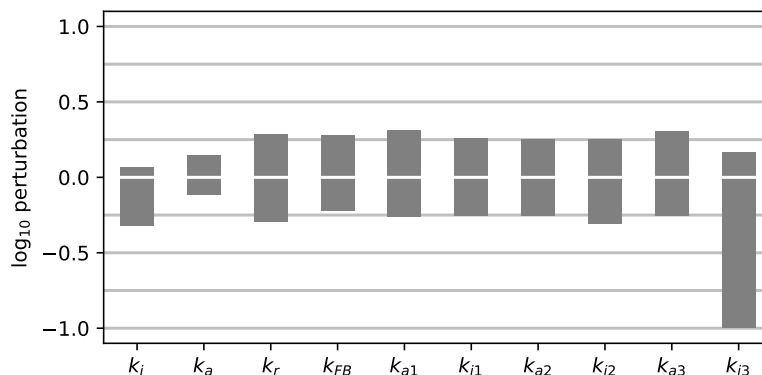
Figure 2.16: **Sensitivity analysis for the receptor + NF cascade model.** Analysis around the parameter set shown in Fig. 2.12. See Methods A.5.1 for details. Related to Fig. 2.12A.

2.8.2 Intermediate frequencies and intensities

We also checked that that the trend of frequency and intensity sensitivity holds for intermediate frequencies and intensities, respectively (see Appendix A.5.2 for details). For frequency sensitivity, we tested if habituation and recovery times were strictly monotonically increasing for intermediate periods of the stimuli in the increasing range used for freq. sensitivity. For example, for the concatenated IFF this range is from T=15 to T=25 (see column labeled T in the Table in Fig. 2.4). Similarly, the habituation time was calculated for intermediate stimulus intensities in the range of intensities previously used (from S=10 to S=30 for the concatenated IFF, see Fig. 2.6). All models considered (concatenated IFF and NF, receptor + IFF, and receptor + NF cascade) maintained the trend of frequency and intensity sensitivity for the tested intermediate frequencies and intensities, respectively.

2.8.3 Habituation threshold

By definition a system has habituated if the peaks do not decrease significantly upon further stimulation. In order to computationally assess this it was necessary to set a fixed threshold for relative peak differences. By default this threshold was set to 0.01 (see Section 2.2). In order to test whether the hallmarks of frequency and intensity sensitivity are robust with respect to the habituation threshold, habituation times were recalculated with different (lower) threshold values (see Appendix A.5.3 for details). We computed the minimum threshold with which frequency or intensity sensitivity is not lost. The results for each of the presented models are shown in Appendix A.5.3. In general, we saw that intensity sensitivity is maintained until lower thresh-

olds than frequency sensitivity. This analysis could be either experimentally irrelevant as it is not possible to distinguish relative changes that are very small. Or it could mean that this habituation threshold is another relevant parameter in the system, with our current output being non-linearly related to a downstream response.

2.9 Discussion

While learning is typically linked to neuronal organisms, there exists substantial evidence of learning in individual cells and single-celled organisms [17, 21, 23, 30]. This raises the question of how learning is executed at the cellular level. In this Chapter we presented mechanistic models of habituation, a form of non-associative learning, which is commonly defined as a reversible decrease in response upon repetitive stimulation. Our models can be interpreted within a cellular context without relying on any specific molecular substrate. Conceptually, habituation and recovery are easily achieved with an incoherent feedforward (IFF) or negative feedback (NF) network motif; both of them common cellular regulatory circuit architectures [33]. However, addressing the nontrivial characteristics of frequency and intensity sensitivity proves to be more challenging. In fact, to the best of our knowledge no model that accounts for intensity sensitivity has been reported so far.

In this study, we demonstrated that the concatenation of two IFF or two NF motifs yields systems that exhibit **all** hallmarks related to the habituation response to a single stimulus, including not only frequency and intensity sensitivity, but also potentiation of habituation and subliminal accumulation (see Table 1.1).

In these concatenated models, frequency sensitivity relies on a separation of timescales and *reversal of memory levels* between the two motifs in response to different stimulation frequencies. Notably, our model indicates that the second motif, characterized by slower decay (less forgetful), plays a pivotal role in determining the recovery dynamics of the entire system. This holds true across all stimulation frequencies examined in our study. This finding is opposed to Staddon's idea that for higher frequencies recovery depends on the memory dynamics of the first module [4]. For our model we find that even for higher frequencies, the recovery dynamics is dependent on the memory dynamics of the second motif.

In our model, with suitable parameter sets, more frequent stimulation results in a higher level of memory species for the first, more peripheral IFF or NF motif, leading to more pronounced habituation. Consequently, less input is

transmitted to the second motif, resulting in a lower memory build-up and faster recovery. This is precisely the *reversal of memory levels* between the two motifs, that we mentioned before.

Beyond frequency sensitivity, the concatenated models also account for intensity sensitivity. In this case, the reversal of memory levels does not happen. At higher intensity, the first response receives both a higher input and memory, reaching higher levels of the response species. This is passed onto the second motif, where the memory levels also increase more for higher intensities. We see that this leads to more stimuli being required to reach the habituated state.

Lastly, the concatenation of two IFF or NF motifs also yields potentiation of habituation (second habituation protocol is faster than the first one), and subliminal accumulation (stimulating the system beyond the habituated state produces alterations such as longer recovery times). In both cases the key point is the memory level build-up of the second motif.

Simplifying the model architecture to a single IFF or NF motif allows for the retention of intensity sensitivity. Potentiation of habituation and subliminal accumulation were much less apparent. Moreover, an exhaustive exploration of the parameter space for the single IFF and single NF models did not yield frequency-sensitive behavior. This indicates that the key point lies in the ability to combine different timescales and/or memory levels, which is made possible by integrating the two motifs.

Lastly, we explored models with non-identical concatenated motifs (IFF or NF), as caused by the presence of a receptor/channel. In a series of very elegant experiments, Cheever and Koshland showed that habituation in PC12 cells upon ATP stimulation is mediated by a downregulation of calcium influx through inactivation of the ATP-gated cation channels [27]. We see with this the importance of a receptor/channel model. Moreover, Cheever and Koshland conducted an initial modeling effort involving receptor/channel activation [29]. They presented a simple receptor/channel model that can toggle between an active and inactive state. However, they did not explore how the habituating behavior could be influenced by the frequency and intensity of stimulation.

In this sense, we developed a receptor/channel model that can toggle between an inactive, active and refractory state, which cannot be activated before returning to the inactive state. This 3-state receptor itself constituted an habituating unit. In order to obtain frequency sensitivity we concatenated this receptor/channel motif with a second circuit. We elaborated two models: in the first one the receptor was concatenated to an IFF motif. The sec-

ond one consisted of the same three-state channel, whose active species activates a cascade of three molecular species. The last of those inactivates the active species of the receptor (negative feedback). In both cases we found appropriate parameter sets that yields systems with frequency and intensity sensitivity, as well as potentiation and subliminal accummulation. Like in the IFF or NF concatenated models, we found a separation of timescales between the two modules and a reversal of memory levels linked to frequency sensitivity.

In sum, in the four models discussed here (concatenated IFF and NF motifs, receptor + IFF, and receptor + NF cascade) the two modules operate on different timescales. This suggests the potential use of different molecular substrates for their implementation. Plausible candidates include receptor modifications, signaling pathways, post-translational modifications, or gene regulatory networks.

Furthermore, IFF and NF motifs have been shown to underlie perfect adaptation in enzymatic [36] and gene regulatory [37] settings. In this work, we showed that a model of habituation can also be implemented with IFF or NF motifs, based on enzymatic transformations. Considering the evidence mentioned for perfect adaptation, a potential future perspective is that a model of habituation could be implemented with IFF or NF motifs based on gene regulation.

While the models presented in this study operate at the single-cell level, broader theories of habituation have been proposed in the context of neuronal systems in the behavioral literature. Generally, two main concepts stand out. Groves and Thompson's dual-process theory emphasizes the existence of two distinct processes —decremental and incremental— that account for habituation and sensitization, respectively [89]. All of our models presented initial sensitization preceding habituation for specific parameter sets (see for example Supplementary Fig. 2.9B for the single IFF model). This tendency is particularly notable at higher stimulation frequencies. A plausible explanation is that if the positive interaction between the input and response node occurs rapidly, the signal might be transmitted before substantial memory build-up. When the stimulation frequency is so high that there is not enough time for the response to fully decay between two stimuli, sensitization may occur. The key distinction from the Groves-Thompson model is the absence of an independent sensitization unit; instead, sensitization is a property inherent to the habituating unit (which can be an IFF, NF or receptor motif).

Sokolov, Konorski, and Wagner [90, 91] developed the second class of theories, which relies on the creation of an internal model formed through repet-

itive stimulation and an arousal system responsible for sensing and amplifying the stimulus. Within this framework, the internal model exerts an inhibitory interaction on the amplifying system. This structure bears evident similarities to our considered habituating units (IFF, NF and receptor/channel motif), where the internal model functions as the inhibitory memory species. The memory accumulation/build-up observed during habituation in our models may be associated with the proposed creation of an internal model. In the context of habituation, this internal model results in a decrement in response, thereby causing a shift in behavior.

In closing, the models introduced in this chapter offer theoretical support for the notion that habituation can be executed at the level of single cells, without necessitating networks of neurons. This not only advances our comprehension of the impressive signal processing capabilities of cells, but also provides insights into the evolutionary roots of learning.

Chapter 3. Experience encoding in gene regulatory networks

The survival of any living system depends on its capacity to sense multiple signals in their surroundings, integrate them, and activate an adequate response. Animals need to extract information not only from the spatial, but also the temporal structure of these signals. At present, our comprehension predominantly leans towards the processing of spatial information. In fact, it remains uncertain whether the spatial and temporal dimensions of stimuli are processed by shared or distinct information-processing systems [47].

Temporal information is crucial to anticipate changes in the environment in order to coordinate a suitable response. For example, in the mammalian brain processing the temporal structure of visual stimuli gives information on the direction and speed of the objects, as well as the duration and time interval between events [47]. In the somatosensory system, the contribution of temporal encoding is not limited to dynamic aspects of the stimulus, such as motion detection, but it is also involved in stationary aspects like object and texture discrimination [92].

The importance of processing temporal information is not limited to neural systems. Bacteria are able to relate groups of events that tend to occur together or in a specific order, what is known as associative memory. For example, *Escherichia coli* prepares itself for low oxygen conditions when it detects a rise in temperature, an indication that it has been ingested by a mammal [93]. Similarly, *Candida albicans* cells, a fungal pathogen, upregulates oxidative stress resistance genes when they detect higher glucose levels, which indicate they have entered a host, preemptively reacting to the immune system of the host [94].

Apart from this associative memory capacity, recent studies indicate that microorganisms display both short- and long-term memory. For instance, the stress response of *Bacillus subtilis* relies not solely on its present growth conditions but also on previous ones [95]. However, the way in which this record of previous history — *i.e.* memory— is integrated and stored in

bacterial cells is not fully understood. We address this issue in what follows.

3.1   Computation with biological networks

It has been postulated that this adaptability relies in general on a complex network of interactions between genes and proteins, frequently at the level of transcriptional regulation [96, 97]. This type of networks are called gene regulatory networks (GRN). Following previous work from [98, 99], in this thesis we hypothesize that the inherent structure and dynamics of these networks establishes how they process temporal information. In other words, we postulate that GRNs work as a reservoir computing system.

Reservoir computing (RC) [49] is a functional neural-network organization that can process temporal information while featuring a very efficient learning process. It was derived from the concepts of Echo State Networks (ESNs) [100] in the field of machine learning and Liquid State Machines (LSMs) [44] in computational neuroscience. The key characteristic of RC is that it separates memory encoding and prediction in different network substructures, as depicted in Fig. 3.1. First, a substructure with recurrent connections is needed to encode history: the reservoir. This structure receives the input signal(s). It is important to keep in mind that the reservoir serves two functions at the same time:

 (i) It acts as a nonlinear high-dimensional expansion of the input signal.

(ii) It allows the network to retain information for a certain time, giving memory to the system [44, 47, 100].

The second substructure, the readout, is a feedforward architecture placed downstream of the reservoir (see nodes in red in Fig. 3.1). The readout substructure uses the history record encoded in the state of the reservoir to make a prediction or a classification. Again, technically it separates the trajectories in the high-dimensional space. Thus, this separation of roles allows to focus the training process, *i.e.* the modification of the network's synaptic strengths so that the desired output is produced, solely on the readout.

In other words, in the classical ESN approach the reservoir is generated randomly, and only the readout is trained. Since feedforward structures are much easier to train than recurrent ones, the RC framework has the computational power of a recurrent network and the ease of training of a feedforward one [47]. Surprisingly, RC demonstrated outstanding performance across various benchmark tasks, e.g. [53, 100, 102, 103, 104].

In this work we have examined the GRN of the bacterial species *E. coli*. We
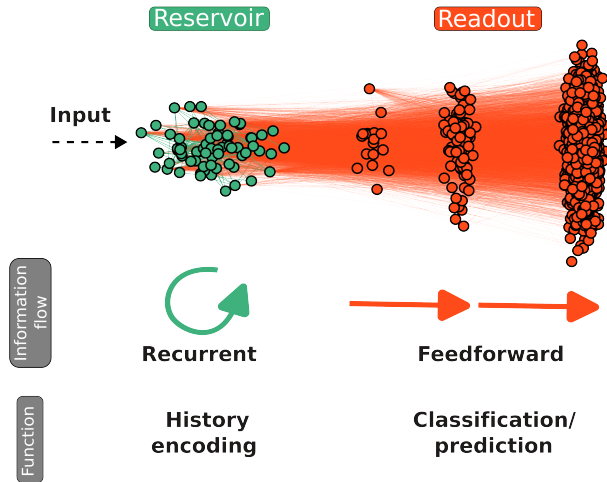
Figure 3.1: **Structural and functional organization of reservoir computing.**. The reservoir (green) is a subgraph with cyclic paths that can maintain a record of the recent history in its dynamics. The readout (red) is a directed acyclic subgraph that reads the information encoded in the reservoir state to perform a given task. The structures shown correspond to the *Escherichia coli* network built in ref. [99] from the database of ref. [101]. The nodes in the readout are grouped by the length of the longest path from the reservoir to them.

have studied its temporal computing power under the framework of reservoir computing. In particular, we have first investigated the effect of the network dynamics in its memory capacity. Furthermore, we have looked into whether the local topology of biological GRNs contributes to their memory encoding. Also, we examined if certain balance between activation and repression is needed to have a functional reservoir. Finally, we have sought for smaller set of genes of the *E. coli*'s network that can perform well in memory-demanding tasks, which can be of great value for experimental validation.

In the following section we will introduce the biological GRN we have studied, *i.e.*, *E. coli*'s network.

3.2 The reservoir computing structure of *E. coli*'s GRN

We analyzed the gene regulatory network of the *E. coli* bacterium. This network was built in ref. [99] using the information available from Eco-Cyc [101], including the sigma factors as transcription factors. One reason to choose a transcriptional network over other types of regulatory networks -*e.g.* protein-protein interaction networks- is that the directionality of the

interactions, and thus of the flow of information, is very well documented. Moreover, in the particular case of *E. coli*, we also count with the information of the effect of the regulation, *i.e.*, if it is an activation or a repression. We consider only the giant component of the GRN. Table 3.1 shows some structural descriptors of the network under study.

	Nodes	Edges	Mean degree
Whole graph	3236	8366	5.17
Reservoir	70	317	9.05

Table 3.1: **General properties of *E. coli*'s whole GRN and its recurrent core.**

Despite the complexity and large size of the network, the subgraph containing recurrent connections or feedbacks is the one considered to be relevant for the temporal computational capabilities of a reservoir [105]. In this direction, the network was simplified by removing all the strictly feed-forward nodes, obtaining a minimal recursive subgraph, *i.e.*, a subgraph containing only the nodes and edges that form recursive structures. To do so, starting from the giant component of the GRN, we *pruned* it by iteratively removing any node that had either in-degree or out-degree equal to zero, until no more nodes could be removed. The resulting subgraph is what will be referred as *core* or *reservoir*. This core is depicted in Fig. 3.1 as the nodes and edges in green. Table 3.1 shows some structural descriptors of the recurrent core.

The resultant reservoir has a higher mean degree than the whole graph. The importance of the reservoir does not rely on a strongly connectivity among its nodes, but rather on its central location in the graph. By construction, there are no recurrences outside the reservoir, and thus all the readout nodes (in red in Fig. 3.1) cannot affect its dynamics. As a consequence of this central location, the dynamics of most of the network is affected by the reservoir. This is what makes the reservoir key for the temporal computational capabilities of GRNs. In the following section we will describe the dynamical model used for the reservoir nodes, as well as its training.

3.3   Reservoir dynamics and training

The dynamics of the *E. coli*'s reservoir was simulated using a discrete time updating rule defined as:

$$\mathbf{x}_t = \tanh(W^{in}\mathbf{u}_t + W\mathbf{x}_{t-1}), \tag{3.1}$$

where $t = 1, ..., T$ are the discrete time points in the training dataset, $\mathbf{x}_t \in \mathbb{R}^{N \times 1}$ is the state vector of the reservoir units (N: the number of reser-

voir nodes) and $\mathbf{u}_t \in \mathbb{R}^{N_{in} \times 1}$ is the input signal vector (N_{in}: the number of inputs), both at time t. Following the notation used in Fig. 3.2, $W^{in} \in \mathbb{R}^{N \times N_{in}}$ is the weight matrix for the input-reservoir connections, and $W \in \mathbb{R}^{N \times N}$ is the weight matrix for the recurrent connections within the reservoir. The values of W^{in} are randomly chosen to be either -0.05 or 0.05. At the same time, the values of the matrix W are real random numbers drawn from a uniform distribution $\mathcal{U}(0,1)$ if the link exists, and 0 otherwise. The sign of the non-zero elements of W is set accordingly to whether the regulation is an activation or a repression. Additionally, the W matrix was normalized to have a spectral radius of 0.9 to ensure the so-called *echo-state property* [48, 100], which we will discuss in some detail in the next section.
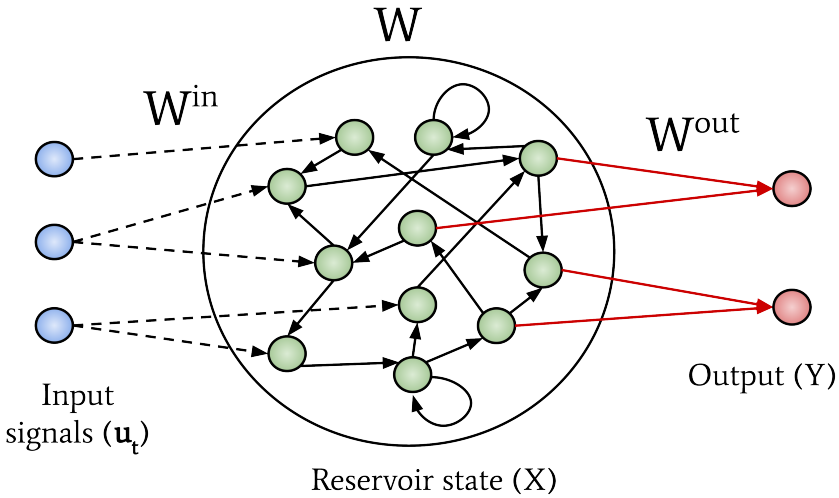
Figure 3.2: **Our ESN model**. The input nodes in blue introduce the external signals ($\mathbf{u}_t$) into random nodes of the reservoir with different strengths, defined by the input weight matrix W^{in}. The reservoir (green nodes) is built with recurrent connections from the *E. coli*'S GRN dataset, defined by the matrix W. The output nodes (red) form a feedforward subgraph that reads the information encoded in the reservoir to make decisions. Only the readout weights W^{out} (red arrows) are trained so that the output Y approximates target output signal(s).

The dynamics of the reservoir is then fed into the readout nodes, which define the output, as depicted in Fig. 3.2. Except where otherwise stated we used as readouts ridge regression nodes. A ridge regression readout computes a weighted sum of the state of the nodes it receives information from as follows:

$$Y = W^{out} X, \tag{3.2}$$

where $Y \in \mathbb{R}^{N_{out} \times T}$ is a matrix with all predicted outputs over time (N_{out}: the number of readout nodes/outputs), $X \in \mathbb{R}^{N \times T}$ is a matrix with the reservoir nodes states over time, and $W^{out} \in \mathbb{R}^{N_{out} \times N}$ is the weight matrix for the reservoir-readout connections, as schematized in Fig. 3.2. To fit the W^{out} weights a ridge regression is used, where the W^{out} weights are obtained from:

$$W^{out} = Y^{\text{target}} X^{\text{tr}} (X X^{\text{tr}} + \gamma^2 I)^{-1} \tag{3.3}$$

Here $Y^{\text{target}} \in \mathbb{R}^{N_{out} \times T}$ is a matrix with all expected/target outputs over time, X^{tr} is the transpose of X, I is the identity matrix, and γ is a regularization coefficient, which helps avoing overfitting (see Sec. 8 of ref. [48] for details).

Ridge regression is a variation of the least squares method that penalizes regression coefficients with large absolute values. In doing so it introduces a certain bias, but on the other hand it also reduces the variance of the estimate. This allows estimating the parameters of a linear regression when the predictor variables are strongly correlated, making it a common readout choice in the context of reservoir computing [106].

Now that we have gone through the details of the *ESN* model we chose, we will look into the first approach we took to study memory encoding in *E. coli*'s GRN: does the dynamical regime of the reservoir have an impact on its memory capacity?

3.4   Memory in *E. coli*'s reservoir: a dynamical approach

It is worth noting that in order to obtain operating reservoirs, some particular design properties are needed. When RC was initially introduced, a series of theorems showed that the reservoir needs to have two fundamental attributes for the proper implementation of the paradigm [44]. Firstly, reservoir dynamics must be able to *separate* different input features that are meaningful for a variety of tasks. Secondly, this same dynamics should be able to *generalize* to unseen examples, thus effectively mapping similar inputs to proximate regions within the dynamical reservoir space.

Legenstein and Maass [107] analyzed how reservoir dynamics contributes to these two desired reservoir properties. Reservoirs with simple attractor dynamics lead to low separability, but large generalization, because large classes of noisy input result in converging reservoir dynamics. On the other hand, when the reservoir presents chaotic dynamics large separability, but very low generalization capabilities, were obtained. This is because chaotic systems are highly sensitive to initial conditions.

In sum, to fulfill the conditions of separability and generalization, reservoirs need to behave somehow in between ordered and chaotic dynamics, *i.e.*, near the so-called *edge of chaos*. This refers to a critical state between ordered dynamics (where disturbances quickly die out into an attractor) and chaotic dynamics (where disturbances are amplified). This property is particularly interesting because of evidence in the literature that cortical circuits, which are hypothesized to operate based on RC, are tuned to criticality (see *e.g.* [108, 109, 110]).

For GRNs there is no evidence suggesting they operate near criticality. Since we are interested in memory encoding in *E. coli*'s network, here we have directly measured the the memory capacity of *E. coli*'s reservoir as it undergoes a phase transition from ordered to chaotic dynamics. With this analysis we seek to see if the dynamical regime of the reservoir has an effect on its memory capacity.

Lastly, although relatively simple, our proposed ESN model has several hyperparameters that can be tuned to affect and change its operating dynamical regime. For example, the spectral radius ρ —largest eigenvalue— of the reservoir weight matrix W of Eq. (3.1) is one of the variables that usually determines the dynamical regime within the reservoir [48]. The spectral radius controls the dynamical stability inside the reservoir when no input is fed into the network. Thus, a spectral radius exceeding unity has been often regarded as a source of instability in ESNs due to the loss of the so-called *echo state property*, a mathematical condition ensuring that the effect of initial conditions on the reservoir states fades away asymptotically in time [45, 100, 111]. Large spectral radius values can lead to reservoirs hosting multiple fixed point, periodic, or even chaotic (when sufficient nonlinearity in the reservoir is reached) spontaneous attractor modes, which all violate the *echo state property*. Taking this into account, we have tuned the spectral radius value in order to obtain reservoirs with ordered as well as chaotic dynamics.

In what follows we analyze the memory capacity of *E. coli*'s reservoir in terms of ρ, and assess whether the reservoir presents ordered or chaotic dynamics. We have chosen a variation of a common benchmark task, namely memory capacity [45] as a memory measure of the network. In order to keep track of the transition from order-to-chaos we have used the Maximum Lyapunov Exponent (MLE), a hallmark indicator of criticality, that has been already applied in the RC framework [107, 112, 113].

We will explain the memory capacity measure and the MLE implementation in the following subsections.

3.4.1   Critical memory capacity

When aiming to quantify the amount of temporal information that a system can store, we can compute the memory capacity of a dynamical network as defined in [45]. We simulated the problem network with a single input node feeding a signal u_t drawn from a random uniform distribution $\mathcal{U}(\text{-}1,1)$. Then a ridge regression node was trained to obtained an output that models a delayed version of the input signal, *i.e.*, output y_t was trained on input u_{t-k}, where y_t is the output Y at time step t (see eq. (3.2)).

To evaluate the short-term memory capacity, we computed the k-delay memory capacity (MC_k) defined as

$$MC_k = \frac{\text{cov}^2(u_{t-k}, y_t)}{\sigma^2(u_{t-k}) \cdot \sigma^2(y_t)}. \tag{3.4}$$

The actual short-term memory capacity is defined as $MC = \sum_{k=1}^{\infty} MC_k$, where the infinite summation is approximated to a long enough finite one [45]. The limitation, though, is that the time series needs to be orders of magnitude longer than the size of the network to ensure that MC_k tends to 0 as k increases. Otherwise, MC_k will never reach 0 and MC will never converge. Since we are dealing with a fairly large biological network, computing the short-term memory capacity with a reasonable precision was not feasible. As an alternative measure we defined the critical memory capacity k^* as the maximum delay k that fulfills $MC_k > 0.5$. A similar modification of the short-term memory capacity has been made in [113].

In order to measure MC_k for each k, 10 input-output series (input: u_t, output: u_{t-k}) of 1000 steps were generated, using 9 of them for the training phase of the ridge regression, and the one remaining to test its performance by measuring the corresponding MC_k of Eq. (3.4). In the next subsection we will define the measure we have chosen to characterize the order-to-chaos transition in the reservoir.

3.4.2   Measuring chaos in reservoirs

Traditionally, to determine whether a dynamical system has ordered or chaotic dynamics, it is common to look at the average sensitivity to perturbations on the initial conditions [112, 114]. The rationale behind this is that small differences in the initial conditions of two otherwise equal systems should eventually die out if the system is in the ordered phase, or persist (and amplify) if it is in the chaotic phase. A measure for the exponential divergence of two trajectories of a dynamical system in state space with very small initial separation is the Lyapunov (characteristic) exponent (LE). Although a

whole spectrum of Lyapunov exponents is defined, the rate of divergence is dominated by the largest exponent (maximum Lyapunov exponent or MLE). It is defined as:

$$\lambda = \lim_{k \to \infty} \frac{1}{k} \ln(\frac{\gamma_k}{\gamma_0}), \tag{3.5}$$

with γ_0 being the initial distance between the perturbed and the unperturbed trajectory, and γ_k being the distance at time k. Thus, chaotic dynamics is typically associated with a positive MLE ($\lambda > 0$), while for sub-critical systems (ordered phase) $\lambda < 0$. A transition thus occurs at $\lambda \approx 0$. Since this is an asymptotic quantity, it has to be estimated for most dynamical systems. For a detailed explanation of the algorithm used to compute the MLE see Appendix B.

3.4.3 Maximal memory capacity at the *edge of chaos*

As explained before, we computed the critical memory capacity of the *E. coli*'s recurrent core for different values of the spectral radius ρ. At the same time, we calculated the MLE of the reservoir dynamics for each value of ρ. These results are displayed in Fig. 3.3. In the first place, the figure shows
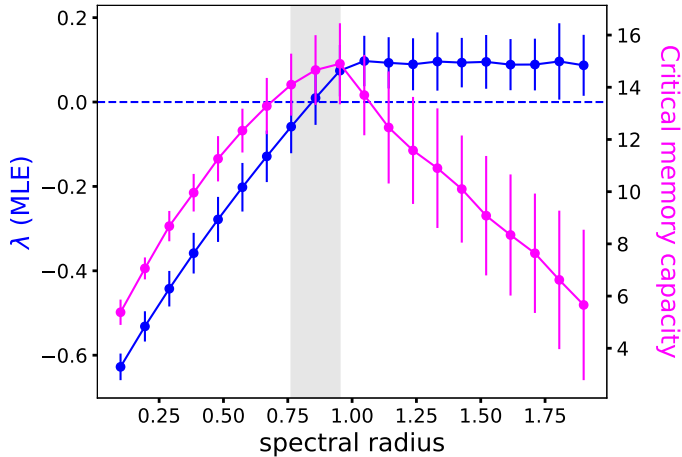
Figure 3.3: **Maximal memory capacity at the *edge of chaos*.** Maximum Lyapunov exponent (blue) and critical memory capacity (pink) as a function of the spectral radius of the reservoir. The maximal critical memory capacity occurs in the vicinity of the transition from ordered to chaotic dynamics (when $\lambda \approx 0$, horizontal dashed line in blue). The values shown are the mean over 50 realizations. Errors were estimated as the standard deviation over 50 realizations of the ESN with different random W^{in} and W (see eq. (3.1)).

that the system transitions from a sub-critical ($\lambda < 0$) to a super-critical

($\lambda > 0$) state for a spectral radius $\rho \approx 0.88$. In order to see more clearly this transition from order to chaos we can look directly at the activities inside the reservoir, which are shown in Fig. 3.4.
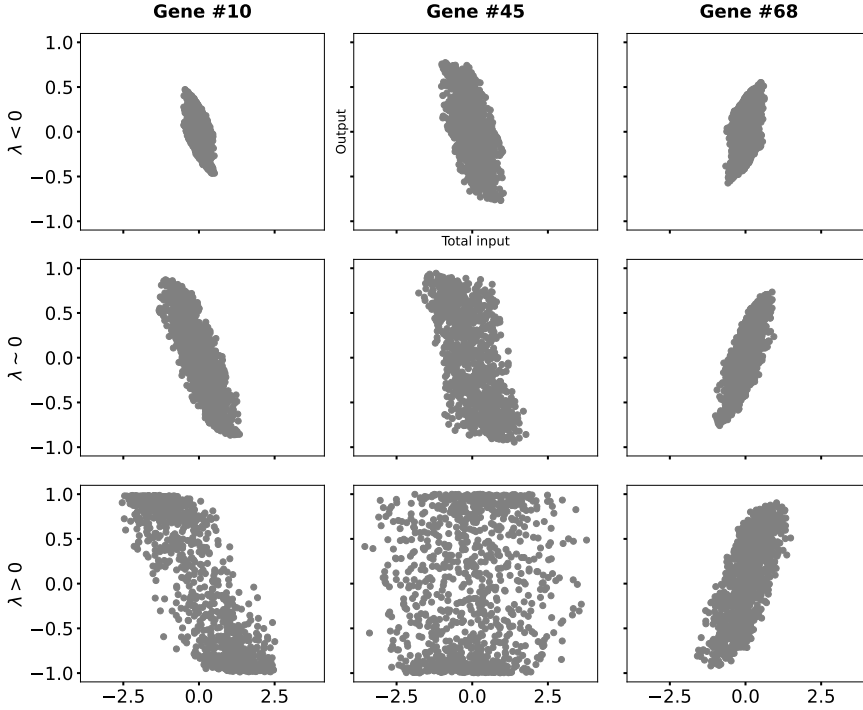
Figure 3.4: **Gene activities across different dynamical regimes.** Activity of three different reservoir nodes operating in the sub-critical, critical and super-critical regimes (from top to bottom) when presented with an input signal drawn from a uniform distribution $\mathcal{U}(-1,1)$. Each point in the panels represents the activity $x_{t,i}$ of gene i at a different time step t as a function of the total input $f_{t,i} = [W^{in}\mathbf{u}_t + W\mathbf{x}_{t-1}]_i$ arriving to it.

The columns in Fig. 3.4 correspond to three different randomly chosen single genes. The rows correspond to three different choices of spectral radius that set the network in different dynamical regimes (ordered, critical and chaotic states). Each point in the panels of Fig. 3.4 represents the state $x_{t,i}$ of a single gene i at a different time step t as a function of the total input $f_{t,i} = [W^{in}\mathbf{u}_t + W\mathbf{x}_{t-1}]_i$ arriving to it. The plots show that when the network is in an "ordered" state, with $\lambda < 0$ (upper row), the responses of the nodes present differences when compared among them, but they are highly localized within each gene, *i.e.*, individual units experience a limited response to stimuli. On the other hand, dynamical states characterized by $\lambda > 0$ (bottom row) have genes whose response extends across the full range

of the non-linearity (with higher probability along with the tails, reflecting a saturated behavior), but it is this same "phase space expansion" that makes units almost indistinguishable from each other. It is only around the critical point or *edge of chaos* ($\lambda \approx 0$, middle row), that we find a compromise between dynamical richness in individual units and variability across them.

Coming back to Fig. 3.3, the maximal critical memory capacity of the *E. coli* reservoir is found just above the onset of chaos when $\rho \approx 0.95$. Taking this into account, our biological reservoir has maximal memory at the vicinity of the order-to-chaos transition.

In closing, the variation of the spectral radius ρ explored in Fig. 3.3 could be accomplished experimentally by altering in a global manner the gene expression potential of cells (varying in a controlled manner the levels of resource cellular components such as RNA polymerases, housekeeping sigma factors, or ribosomes). Thus if *E. coli*'s cell processes information according to the reservoir computing paradigm, its memory capacity should vary non-monotonically with its global expression capacity, considering the results of Fig. 3.3. Another interest open question in this case will then be if natural networks are tuned to operate near the maximum memory capacity, which occurs at the *edge of chaos*, as we have seen in this work.

3.5 Effect of local topology on memory capacity

In the previous section we analyzed the impact of the dynamical regime of the *E. coli*'s reservoir on its memory capacity, following previous studies on artificial ESNs that showed improved performance at the *edge of chaos* [107]. In the following we take a different perspective: does the local topology of biological reservoirs have an influence on its memory capacity?
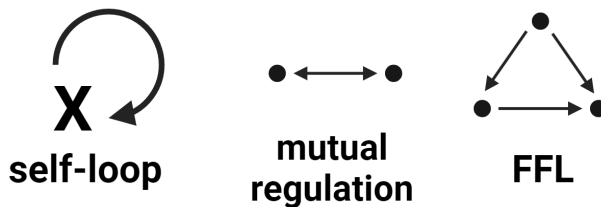
Figure 3.5: **Memory motifs in *E. coli*'s GRN.** Local topology patterns analyzed. From left to right: self-loop, mutual regulation and feedforward loop (FFL). The sign of the interactions (arrows) is ignored.

As we know, *E. coli*'s GRN patterns of nodes and arrows are not random: they have been shaped by evolution [33]. To look for *meaningful* patterns,

we can compare the real network to an ensemble of randomized networks. The randomized networks are networks with the same characteristics as the real network (equal number of nodes and edges), but where the connections between nodes are made at random. Patterns that occur in the real network significantly more often than in randomized networks are called network motifs [115, 116].

In our work we have focused on three circuits: self-loops, mutual regulation circuits and feedforward loops (FFLs), which are displayed schematically in Fig 3.5. The arrows of the motifs in Fig. 3.5 can represent either activation or repression. Self-loops and FFLs have been reported to be network motifs of *E. coli*'s GRN [33]. The mutual regulation circuit has been included, since we hypothesize that some local recurrence is needed to have a network with memory. From now on we will refer to the these three circuits as *memory motifs*.

Tables 3.2 and 3.3 show the number of each memory motif for the whole network and the reservoir, respectively. We compare these numbers with the expected motifs in its correspondent randomized networks, and compute the z-score.

Whole graph	Real network	Randomized network	z-score
self-loops	126	3 ± 2	79
mutual reg.	28	3 ± 2	14
FFL	4798	17 ± 4	1167

Table 3.2: **Number of motifs in the whole graph.** The number of motifs in the real network is compared to the expected number in randomized networks with the same number of nodes and edges (mean $\pm$ s.d. computed over 1000 realizations). The z-score is computed as z-score$= \frac{N_{\text{real}} - \langle N \rangle_{\text{rand}}}{\sigma_{\text{rand}}}$.

Reservoir	Real network	Randomized network	z-score
self-loops	55	5 ± 2	26
mutual reg.	28	10 ± 3	5.8
FFL	147	73 ± 10	7.6

Table 3.3: **Number of motifs in the reservoir.** The number of motifs in the real network is compared to the expected number in randomized networks with the same number of nodes and edges (again, mean $\pm$ s.d. computed over 1000 realizations). The z-score is computed as shown in the caption of Table 3.2 above.

Comparing Tables 3.2 and 3.3 reveals that the z-score of FFL is reduced

by a factor of 154 between the whole graph and the reservoir. This proves that the whole graph is much more enriched with FFLs than the reservoir. This result makes sense if we think that the whole graph comprises both the reservoir and the readout. The latter is a feedforward architecture with 98% of the nodes, which is locally enriched with feedforward loops (FFL) motifs.

The self-loop's z-score decreases by a factor of 3 between the whole graph and the reservoir. However, looking at both z-scores, self-loops are a significantly relevant motif in both the reservoir and the whole graph. Similarly, the mutual regulation's z-score is reduced by a factor of 2.4 between the whole graph and the reservoir. It is worth mentioning that all 28 mutual regulation motifs of the whole graph are part of the reservoir.

3.5.1 Memory capacity of the memory motifs

To assess the relation of the three memory motifs in question with the reservoir memory capacity, we have sampled ≈ 2400 sub-reservoirs of different sizes from the whole *E. coli*'s reservoir of 70 genes. For that purpose, we started by removing a random node from the reservoir. Then, we pruned the resulting network to make sure it is still a reservoir, and kept only its giant connected component. We iterated this process until we reached a reservoir of only 3 nodes (minimum size considered). We repeated this process 100 times starting from different nodes, and ended up with a total of 2394 sub-reservoirs. To illustrate this, in Fig. 3.6 some small size examples of the sub-reservoirs obtained are depicted. We obtained reservoirs with sizes from 3 to 69 nodes. Figure 3.7 shows the distribution of the reservoir sizes.
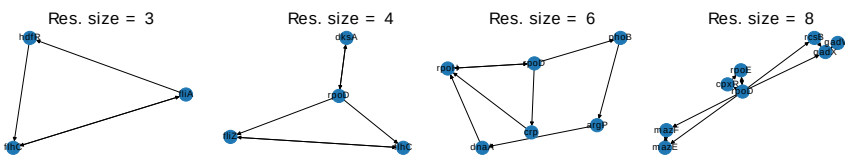
Figure 3.6: **Sub-reservoirs of *E. coli*'s recurrent core.** Small size examples of the sub-reservoirs studied. For a clearer visualization the sign of the edge is not highlighted, and self-loops are omitted. We obtained a sample of a total of 2394 sub-reservoirs with sizes from 3 to 69 nodes.

As a next step, we counted the number of each of the three memory motifs in every reservoir. The distributions of network motifs is depicted in Fig. 3.8. Besides, for all 2394 reservoirs we measured their critical memory capacity, as defined in subsection 3.4.2. The results are shown in Fig. 3.9. Panels a, b and c in this figure show the critical memory capacity as a function of the
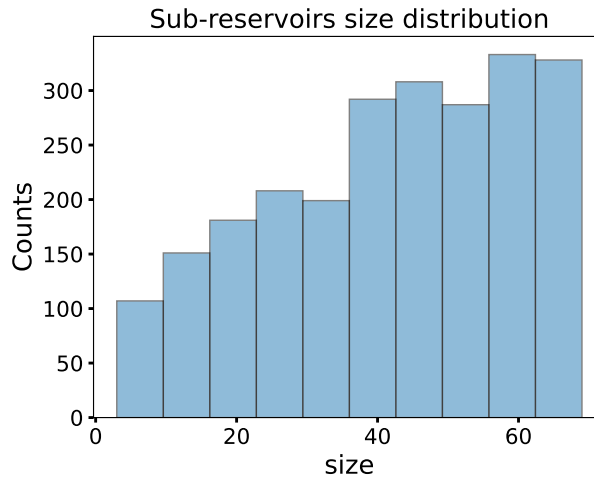
Figure 3.7: **Size distribution of sub-reservoirs.** They were generated from the *E. coli* reservoir. The total number of sub-reservoirs is 2394. Related to subsection 3.5.1.
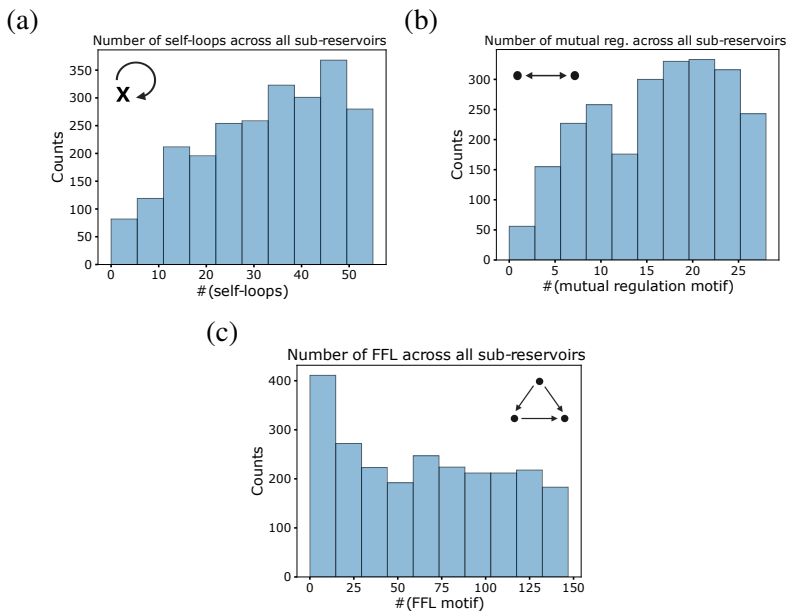
Figure 3.8: **Distribution of network motifs across all sub-reservoirs** (size from 3 to 69 nodes/genes). (a) Self-loops. (b) Mutual regulation motif. (c) Feedforward loop motif. Related to subsection 3.5.1.
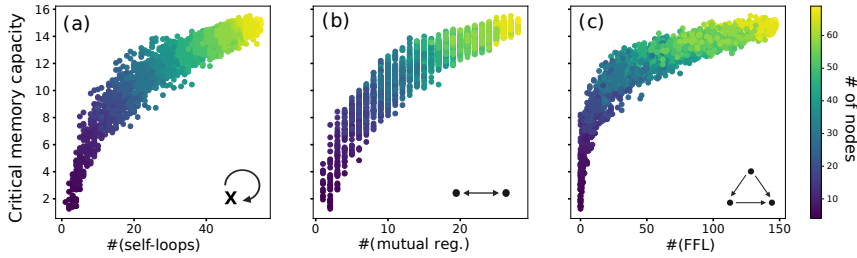
Figure 3.9: **Critical memory capacity vs number of memory motif for sub-reservoirs.** (a) x-axis: number of self-loops. (b) x-axis: number of mutual regulation. (c) x-axis: number of FFL. The critical memory capacity for each reservoir was computed as the average over 50 realizations. Point color represents the number of nodes of the reservoir (from 3 to 69).

number of self-loop, mutual regulation and FFL motifs, respectively. Each point represents a sub-reservoir, and the color reflects its number of nodes. For the three cases we see an increasing relationship between the number of motifs and the memory capacity. Also, as expected, the amount of motifs grows with the size of the reservoir. On the other hand, by looking at the x-axis we can see that the number of memory motifs range is different: for self-loop is 0-55, for mutual regulation is 0-28 and for FFL is 0-147. For example, networks with $\sim$ 30 mutual regulation motifs have a memory capacity of $\sim$15.5, while networks with $\sim$ 30 self-loops have a memory capacity of $\sim$12, and reservoirs with $\sim$ 30 FFLs have a memory capacity of $\sim$10. This suggests that mutual regulation is the motif that contributes the most to memory, followed by self-loops, and then FFL.

In order to have more similar scales, we can analyze the memory capacity in terms of the number of memory motifs normalized by the expected number in randomized networks. For that purpose, for each reservoir we simulated its correspondent random network with the same quantity of nodes and edges. We counted the number of self-loops, mutual regulation and FFL in the random network. We repeated the process 1000 times, and then computed the expected number as the mean of the 1000 realizations. The results are depicted in Fig. 3.10.

In Fig. 3.10 we continue seeing the increasing relationship between the normalized number of motifs and the memory capacity for the three patterns: self-loops (Fig. 3.10.a), mutual regulation (Fig. 3.10.b) and FFL (Fig. 3.10.c). We can see that the the sub-reservoirs are more enriched by self-loops than mutual regulation and FFL motifs, as it was already noted for the whole reservoir in Table 3.3. In the x-axis, the value $x = 1$ means the reservoir has the same number of motifs as its corresponding random
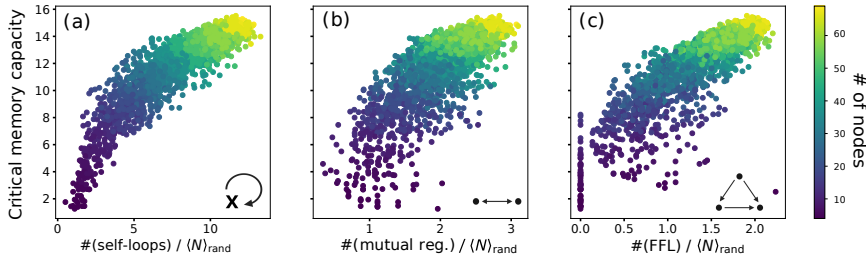
Figure 3.10: **Critical memory capacity vs number of memory motif normalized by expected number in randomized networks.** (a) x-axis: norm. number of self-loops. (b) x-axis: norm. number of mutual regulation. (c) x-axis: norm. number of FFL. The critical memory capacity for each reservoir was computed as the average over 50 realizations. Point color represents the number of nodes of the reservoir (from 3 to 69). The expected numbers of motifs were calculated in random network with the same number of nodes and edges (mean over 1000 realizations).

network. We can see sub-reservoirs can have up to 10 times more self-loops than the randomized graph. For mutual regulation and FFL this factor goes down to 3 and 2, respectively.

Another interesting feature of Fig. 3.10 is that FFLs do not determine the reservoir's memory capacity, since even networks with 0 FFLs have reservoirs with memory capacity in a broad range (from 0 to 8). Clearly, these networks have other memory motifs that give them memory. Moreover, observe that this broad range at 0 does not happen for self-loop or mutual regulation motifs.

Coming back to the results in terms of the absolute number of motifs of Fig. 3.9, we looked at the memory capacity distribution filtering for networks with less number of memory motifs than a threshold. The thresholds used were 28 (maximum number of mutual regulation) and 55 (maximum number of self-loops). The results are depicted in Fig. 3.11. This figure shows that reservoirs with 28 or less mutual regulation motifs tend to have more memory capacity than networks with an equivalent number of FFL or self-loops. This suggests that from the three motifs studied, the one that contributes the most to the temporal processing power of the recurrent core is the mutual regulation motif. Analogously, if we compare the two remaining motifs, we can see that self-loops make a greater contribution to memory than FFL (see Fig. 3.11b).

Overall, we have investigated the memory capacities of the *E. coli*'s reservoir in terms of its local topology, which has not been done so far to our knowledge. Firstly, what we have seen is that while the whole graph is

(a)   (b)
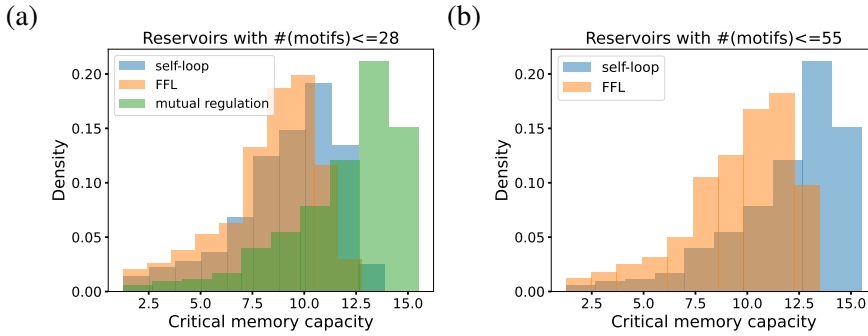
Figure 3.11: **Critical memory capacity distributions for reservoirs with less motifs than an imposed threshold.** (a) threshold = 28. Networks with 28 or less mutual regulation motifs tend to have higher memory than reservoirs with 28 or less self-loops or FFL. (b) threshold = 55. Networks with 55 or less self-loops tend to have higher memory than reservoirs with 55 or less FFLs. The critical memory capacity for each sub-reservoir was computed as the average over 50 realizations.

highly enriched in FFL, in the reservoir this enrichment is decreased by a factor of 154 (see Tables 3.2 and 3.3). This result is logical if we take into account that the whole graph is in its majority conformed by the readout, *i.e.* a feedforward architecture. Besides, by analyzing a sample of sub-reservoirs of varied sizes, we have seen that FFLs do not determine the memory capabilities of the reservoir. Contrarily, the mutual regulation is the strongest indicator of memory capacity of the reservoir, followed by the self-loops.

Looking at the broader picture, this last remark goes in line with the idea that recurrences, in this case within one (self-loop) and two (mutual regulation) genes of the *E. coli* reservoir, grant systems with temporal information processing capabilities. Opposite to this, strictly feedforward motifs like FFL do not contribute to memory acquisition.

3.6 Activation/repression balance in GRNs

As previously mentioned, the dataset that we studied [101] reports the nature of the transcriptional regulations, *i.e.* whether each arrow represents an activation or repression. The proportion of repression in the whole graph is 24%, while in the reservoir is 41%. In this sense, we wanted to investigate if this activation/repression balance has an effect on the performance of the network. Has evolution tuned the activation/repression ratio in natural reservoirs to operate near optimal performance? Is the memory capacity of the network affected if we modify this ratio?

This idea has been explored in the context of biological neural networks

[117], but not in the field of gene regulatory networks. In that case, the excitatory/inhibitory (E/I) balance, defined as the balance between excitation and inhibition of synaptic activity in a neuronal network, plays a crucial role in maintaining the regular functionality of the brain. This equilibrium, responsible for regulating normal spike rates, is disrupted in numerous pathological conditions, resulting in either excessive or diminished excitation relative to inhibition, termed E/I imbalance [118, 119].

Our protocol to study the effect of the activation/repression balance in gene regulatory networks consisted on randomizing only the signs of the reservoir edges, while maintaining a certain proportion of inhibition. The performance of the *E. coli*'s reservoir was studied for seven repression/activation ratios. For this purpose we have chosen the 10th-order Nonlinear Autoregressive Moving Average (NARMA) task, a memory-demanding benchmark commonly used in the context of neural networks [120]. In the next subsection we will summarize the details of this task.

3.6.1   10th-order NARMA task

The task consists in training a network to reproduce the output of the 10th-order NARMA system [121]. This is a discrete time system where the input values s_t are drawn from a random uniform distribution $\mathcal{U}(0, 0.5)$, and the output $y^{\mathrm{NRM}}(t)$ is defined by:

$$y^{\mathrm{NRM}}(t+1) = 0.3 y^{\mathrm{NRM}}(t) + 0.05 y^{\mathrm{NRM}}(t) \sum_{i=0}^{9} y(t-i) + 1.5 s(t-9) s(t) + 0.1$$

$$(3.6)$$

To test if the dynamics of *E. coli*'s reservoir can represent the temporally correlated NARMA input, the network was simulated with a single input node (in blue in Fig. 3.2) feeding the $s(t)$ series in the system.

Then, a readout node was trained (in red in Fig. 3.2) to reproduce the output $y^{\mathrm{NRM}}(t)$ of the 10th-order NARMA system using only the instantaneous state of the network (reservoir state in Fig. 3.2). For each realization, 10 NARMA series of 1000 steps were generated, using 9 of them for the training phase and the remaining one to test the performance.

The challenge of the NARMA task is that the output of the 10th-order NARMA time series depends on the input and output values of the last 10 time steps (see $y^{\mathrm{NRM}}(t)$ in Eq. (3.6)). This information about the past must be encoded in the reservoir state for the predicted output of the readout node to be able to accurately model the input.

To quantify the network performance, we used the Normalized Root Mean Squared Error (NRMSE) between the predicted and target output signals, which is defined as

$$NRMSE = \sqrt{\frac{\langle (y(t) - y^{\text{target}}(t))^2 \rangle_t}{\langle (y^{\text{target}}(t) - \langle y^{\text{target}}(t) \rangle_t)^2 \rangle_t}}, \tag{3.7}$$

where $y(t)$ is the output predicted by the readout, $y^{\text{target}}(t)$ is the target output ($y^{\text{NRM}}(t)$ in this case), and $\langle \cdot \rangle_t$ indicates the mean over time.

In the next subsection we will show the results of *E. coli*'s reservoir performance when confronted with the NARMA task for varied activation/repression proportions.

3.6.2   Activation/repression ratio and reservoir performance

Having explained the details of the task in question, we have confronted *E. coli*'s reservoir with the NARMA task varying the proportion of activation/repression. For that purpose, we randomized the signs of the edges, while maintaining certain proportion of repression. The obtained results are displayed in Fig. 3.12a. The results show that the performance of the *E.*
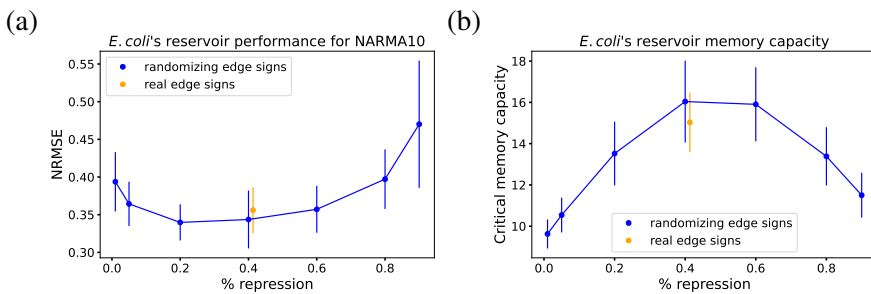
Figure 3.12: ***E. coli*'s reservoir performance in terms of activation/repression ratio.** (a) Results for the 10th-order NARMA task. (b) Results for the critical memory capacity. The results for networks with randomized edge signs (conserving a fixed repression proportion) are shown in blue. In turn, the result for the network with the edge signs from the dataset [101] is depicted in orange. The values shown are the mean over 100 realizations. Errors were estimated as the standard deviation over 100 realizations.

coli's reservoir for the NARMA task varies non-monotonically with respect to the repression proportion across the network. In fact, the best performance is observed when the percentage of repression is aorund 40%. In orange, the performance of the network with the edge signs from the biological dataset [101] is shown. As we can see, the biological reservoir operates near the activation/repression ratio that yields optimal performance. In

short, when the repression percentage deviates from 40% (above or below) the performance worsens.

We checked if this effect also holds for the critical memory capacity task, as defined in Section 3.4.1. The results for this second task are shown in Fig. 3.12b. Similarly to the case of the NARMA task, the memory capacity is maximal at around a 40% repression rate, which is very close to the ratio observed in biological networks.

In sum, by evaluating two memory-demanding tasks we can say that a certain balance between activation and repression is needed in the *E. coli*'s reservoir in order to grant it with temporal-information processing capabilities.

3.7 Smaller *memorious* GRNs

In this last section, the aim was to search for sub-networks of the *E. coli*'s reservoir that perform well in memory-demanding tasks. This would be of a great value for experimental validation. The smaller the number the genes, the easier it is to obtain experimental evidence that the gene regulatory network works as a reservoir computing system.

In this sense, we confronted the 2394 sub-reservoirs (introduced in Section 3.5.1) with the memory capacity and the 10th-order NARMA tasks defined above, and also with a biologically inspired task, *i.e.* a delayed AND, which we will explain in the next Section. Having done so, we looked for networks with a good size-performance trade-off across the three tasks. Before continuing with the results we first describe the delayed AND task.

3.7.1 Delayed AND task

The goal of developing a delayed task was to have a more biologically realistic problem, in comparison with the critical memory capacity and the NARMA task. In this sense, the delayed AND task was inspired on the example of associative memory of *E. coli* studied by Tagkopoulos et al. [93]. In that paper, the authors showed that *E. coli* is capable of associate groups of events that tend to occur together or in a specific order. This kind of association, for instance, allows the bacterium to prepare for low oxygen conditions when it detects a rise in temperature, an indication that it has been ingested by a mammal [93]. One way of conceptualizing this behavior is that *E. coli* has learned that if an increase in temperature is followed by a decrease in oxygen levels, then an appropriate response is needed in order to survive the low oxygen condition.

With this in mind we have designed the delayed AND task. The reservoir is simulated with two input nodes: the first one would be representative of temperature conditions and the second one of oxygen levels. The input signal for each node consists of a 600 time step series with randomly distributed pulses of unit height with a duration of three time steps, as depicted in Fig. 3.13 (top row). The output of the delayed AND task is calculated as
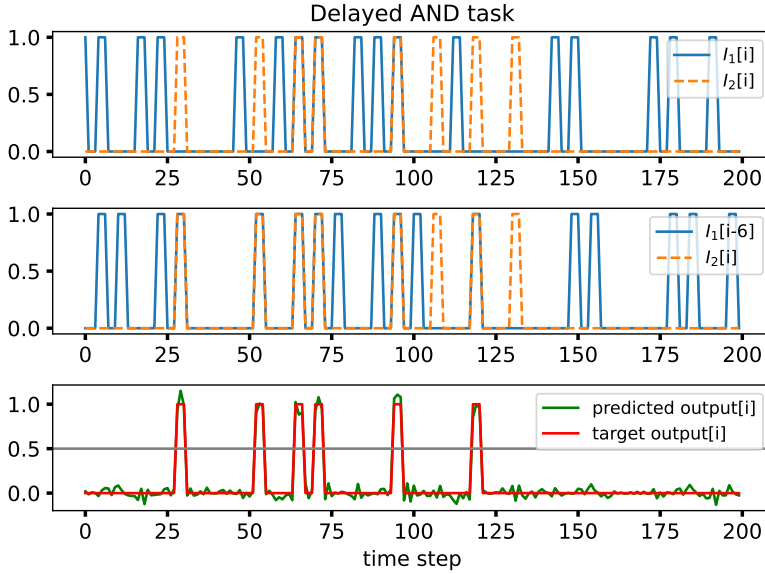
Figure 3.13: **A delayed AND task.** Top row: time series of the two input signals ($I_1[i]$ and $I_2[i]$). Middle row: the input I_1 delayed 6 time steps ($I_1[i-6]$) in relation to input $I_2[i]$. Bottom row: the target output (red) at time step i is calculated as an AND gate between $I_1[i-6]$ and $I_2[i]$. In green the predicted output by the whole *E. coli*'s reservoir is shown.

the AND gate of input I_1 at time step $i - 6$ and input I_2 at time step i. In other words, if at time step i $I_2 = 1$ and at time step $i - 6$ $I_1 = 1$, then the output $y^{\text{target}} = 1$ (see Fig. 3.13 middle and bottom row).

The bottom row of Fig. 3.13 shows the output predicted by the whole *E. coli*'s reservoir (70 genes) in green. To quantify the network performance, we first binarize the output as follows:

$$\text{output}^{\text{bin}} = \begin{cases} 0 & \text{if output}^{\text{pred}} < 0.5, \\ 1 & \text{if output}^{\text{pred}} > 0.5. \end{cases} \tag{3.8}$$

The chosen threshold is shown as a grey line in Fig. 3.13 (third row). Once binarized, the performance is computed by the NRMSE between the bina-

rized predicted and target output signals ($\text{output}^{\text{bin}}$ and y^{target}), which has been defined in Eq. (3.7).

3.7.2 Candidates for experimental validation

We confronted the sub-reservoirs introduced in Section 3.5.1) with the memory capacity, the 10th-order NARMA task, and the introduced delayed AND task introduced in the previous Section. The results, filtering only reservoirs whose performance is within 1.25 standard deviations from the mean value across all sub-reservoirs, are depicted in Fig. 3.14. As shown in red in the
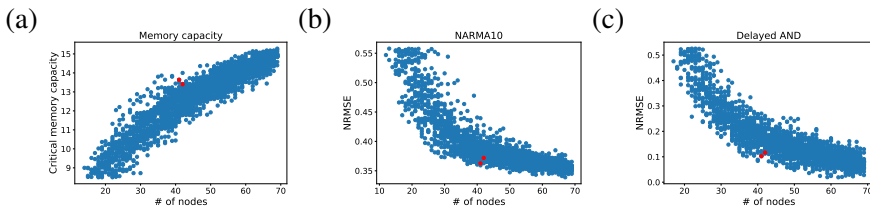
Figure 3.14: ***E. coli*'s sub-reservoirs performance in terms of network size.** (a) Results for the critical memory capacity. (b) Results for the 10th-order NARMA task. (c) Results for the Delayed AND task. The performance for each sub-reservoir was computed as the average over 50 realizations for each one of the three tasks. In red we show the two identified networks with a good size-performance compromise across the three tasks.

figure, we were able to find two sub-reservoirs of size ≈ 40 genes that have a good size-performance trade-off across the three tasks considered. These networks have really good performances in the three tasks in comparison with other reservoirs of equal or similar size. In Tables 3.4 and 3.5 we report their number of motifs and the correspondent z-scores.

Res. #591	Real network	Randomized network	z-score
self-loops	32	4 ± 2	14
mutual reg.	18	9 ± 3	3
FFL	69	54 ± 9	1.67

Table 3.4: **Number of motifs in reservoir #591.** This reservoir has a good size-performance trade-off for the memory capacity, NARMA10 and delayed AND tasks. It has 42 genes and 181 edges. The number of motifs in the real network is compared to the expected number in randomized networks with the same number of nodes and edges (mean $\pm$ s.d. computed over 1000 realizations). The z-score is computed as defined in Table 3.2.

The sub-reservoirs of Tables 3.4 and 3.5 have 57% of the nodes from the

Res. #678	Real network	Randomized network	z-score
self-loops	30	4 ± 2	13
mutual reg.	17	8 ± 3	3
FFL	75	48 ± 8	3.38

Table 3.5: **Number of motifs in reservoir #678.** This reservoir has a good size-performance trade-off for the memory capacity, NARMA10 and delayed AND tasks. It has 41 genes and 171 edges. The number of motifs in the real network is compared to the expected number in randomized networks with the same number of nodes and edges (again, mean $\pm$ s.d. computed over 1000 realizations). The z-score is computed as defined in Table 3.2.

whole reservoir. Furthermore, they proved to have good performances across three different memory-demanding tasks. Taking these facts into account, they are good potential candidates for experimental validation on temporal information processing in *E. coli*.

3.8 Discussion

In this Chapter we have analyzed the temporal information processing capabilities of the gene regulatory network of the bacterium *Escherichia coli* within the reservoir computing (RC) framework. In RC, memory encoding and decision making are processed in two different structures of the network. The first structure, the reservoir, has recurrences that provide a *fading memory* property so that it can efficiently encode recent history. The other structure, the readout, has a feedforward structure and uses the information it receives from the reservoir to make a classification or prediction. This separation of roles allows the system to process temporal information while still being very efficient at learning new tasks [47].

We first examined the GRN built originally by Gabalda-Sagarra et al. [99] from dataset [101], confirming that its topology matches the RC structural organization. We then focused on the dynamics of the reservoir, due to its relevance in temporal information processing. We explored whether the dynamical regime of the reservoir affects its memory capacity. This was inspired by work done on artificial ESNs, where it has been seen that the performance of reservoirs are optimal at the critical point of an order-to-chaos transition, also known as *edge of chaos* [107, 122]. Beyond artificial neural systems, cortical circuits have also been suggested to operate at a critical state [108, 109, 110]. For GRNs we did not find any study on the impact of reservoir dynamics on its processing capabilities. Here we saw

that the *E. coli*'s reservoir has maximum memory capacity just above the onset of the transition to chaos, *i.e.* in the vicinity of the critical point (*edge of chaos*). In this sense, it would be interesting to study experimentally whether GRNs are tuned to operate near optimal memory capacity. For this purpose, a means of making the system undergo an order-to-chaos transition is needed. A possible way of doing this would be to alter in a global manner the gene expression potential of cells, as it has been previously suggested [99].

Additionally, we delved into whether the local topology of GRNs contributes to their memory-encoding capabilities. In this sense, network motifs are significantly relevant patterns of nodes and edges across the network, which were introduced by Alon and co-workers [115, 116]. In those studies, network motifs in *E. coli*'s GRN were analyzed as simple building blocks of networks, and the dynamic features of each network motif is examined. Here we took a different approach: we constructed a sample of ≈2400 sub-reservoirs from the full *E. coli*'s reservoir. Then we simulated their dynamics in the framework of a memory-capacity task, and we aimed to find a relation between the number of motifs in the sub-reservoirs and their memory capabilities. We focused on three network motifs: self-loops, mutual regulation and feedforward loops (FFL). We saw that network motifs with recurrences (self-loops and mutual regulation) are more important for the reservoir's memory capacity than feedforward circuits, such as FFL. For example, a sub-reservoir with a fixed number of mutual regulation motifs has in average more memory than another sub-reservoir with the same number of FFLs. This approach to the temporal capabilities of genetic reservoirs has never been analyzed before, to our knowledge, and we believe it may help to reach a wider understanding on how biological networks process temporal information.

We also explored whether the balance between transcriptional activation and repression is relevant in order to obtain a functional GRN under the RC framework. This approach was inspired on studies in biologic neural networks, where the excitatory/inhibitory balance has been proven to be fundamental in maintaining the regular functionality of the brain [118, 119, 123]. The repression percentage in the reservoir built from the dataset of [101] is 41%. By varying this percentage artificially we saw that the optimal performance for two different memory-demanding tasks (memory capacity and 10th-order NARMA) are obtained for a repression percentage near 40%. This reinforces the idea that regulations in GRN have been shaped by evolution. Moreover, in future explorations on temporal signaling processing in GRNs we need to take into account this activation/repression balance in order to have a full picture.

Lastly, we looked for *E. coli*'s sub-reservoirs with a good size-performance compromise. We identified two different sub-networks that exhibit high performance in three memory-demanding tasks: memory capacity, 10th-order NARMA task, and the more biologically plausible delayed AND task. These networks could be of great value, since searching for experimental validation on RC for *E. coli*'s 70 genes reservoir is indeed challenging. The networks we identified have almost half the size of the full reservoir, while maintaining a really good performance on temporal processing tasks. In this sense, they may make empirical verification way more approachable.

Chapter 4. Experience-dependent behavior in a minimal animal

Every organism makes decisions many times a day, and innumerable times in their lifetime. These decision-making events are crucial for survival. This is the case, for example, when animals navigate their complex and dynamic environment in search of food, a mate or a breeding site, or to escape from predators. In order to make decisions, animals usually evaluate signals from their current external environment and integrate them with their past experiences (which are encoded in their internal state) [124, 125, 126]. This results in experience-dependent behaviors, where the individual's past experiences (or context) affect their present actions. One of the most important topics of current research is to identify the molecular and cellular mechanisms that underpin these adaptive behaviors.

The nematode *Caenorhabditis elegans* is an ideal organism in which to explore the neural basis of experience-dependent behaviors. *C. elegans* has been an important model system for biological research over the years in a variety of fields including genomics, cell biology, developmental biology, and neuroscience [127, 128, 129, 130, 131]. Importantly for neuroscience, in particular, the *C. elegans* connectome is by far the most complete to date, comprising 302 neurons and over 7000 connections for the hermaphrodite [54]. Despite its relatively simple nervous system, *C. elegans* shows experience-dependent behavioral plasticity in response to a variety of environmental cues, such as odor [57], taste [58], and temperature [59], among others.

A series of elegant experiments performed over the years by the group of Prof. Yuichi Iino at the University of Tokyo [65, 132, 133, 134] have demonstrated that chemotaxis of *C. elegans* to sodium chloride (NaCl) is an experience-dependent behavior. Specifically, animals migrate up or down salt gradients towards the concentration that they have previously experienced during cultivation [65]. In other words, if a worm cultivated at a high NaCl concentration is set at a lower concentration in the middle of a salt gradient, it crawls up the gradient (top panel of Fig. 1.3). Conversely, if

the worm was cultivated at a low NaCl concentration, it crawls down the gradient (bottom panel of Fig. 1.3).

In this Chapter we present a mechanistic model, strongly grounded in multiple experimental observations at different levels, that captures the above-described experience-dependent chemotaxis to NaCl exhibited by *C. elegans*. The model includes within an integrative framework the sensory components of the process, at both the molecular and cellular levels, and the motor features of the behavior observed, at the organismal level. The model is biologically grounded, including all necessary and sufficient components identified experimentally, without introducing artificial regulatory mechanisms. At the same time it is not too overly detailed, avoiding unnecessary molecular details that could lead to over-parameterization. One of the highlights of the model is that within a single framework we can account for the two context-dependent behaviors, i.e. high- and low-salt attraction, according to the worm's previous experience, with the same circuit and without changing parameter values.

4.1   Neuronal determinants of experience-dependent chemotaxis

The neural and molecular mechanisms that underlie the experience-dependent behavior schematized in Fig. 1.3 have been studied experimentally in a series of landmark articles by the Iino group [65, 132, 133, 134]. These studies have revealed several key players at both the cellular and molecular levels. At the cellular level, the amphid sensory neuron right (ASER) has been found to be necessary and sufficient for the behavior to occur. Specifically, functional inhibition or genetic ablation of ASER completely impairs the plasticity of salt chemotaxis, whereas disruption of the activity of other chemosensory neurons has no substantial effect [65]. This demonstrates that sensory input to ASER is critical for this adaptive behavior. Taking this into account, in our model we limit the sensory aspects of the system to this neuron.

The key question is how ASER drives this bidirectional reorientation behavior, i.e. how it leads to high- and low-salt attraction in high- and low-salt cultivated animals, respectively. It has been suggested that ASER generates experience-dependent chemotaxis by altering the magnitude of excitatory and inhibitory signals to its downstream interneurons AIA, AIB, AIY, and AIZ [65, 135]. In our model, we consider for simplicity a single ASER target, namely AIB, which is by far the most studied in this context.

AIB is a turn neuron, i.e. its activation leads to an increase in the probability
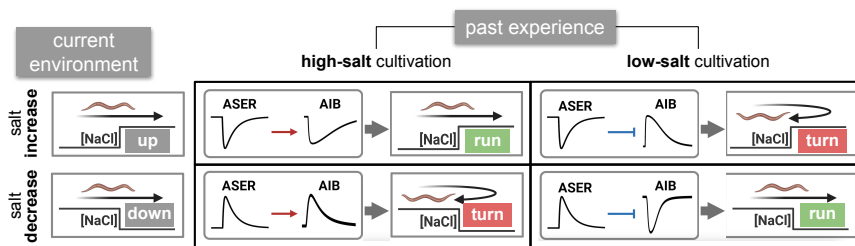
Figure 4.1: **Dual AIB response to ASER enables experience-dependent behavior**. This $2\times$ cartoon matrix shows schematically the responses of the two neurons considered in our model (the sensory neuron ASER and the turn interneuron AIB) and the resulting behavior of the worm for two binary sets of environmental and experiential conditions (rows and columns, respectively). Low AIB activity implies enhanced turn probability (matrix cells labeled "turn" in red), while high AIB activity implies decreased turn probability (matrix cells labeled "run" in green). As a result the worm always tends to move towards the salt levels that it had previously experienced.

that the worm re-orients its crawling direction [136, 137]. In that sense, here we focus on the *C. elegans* locomotion strategy known as klinokinesis, consisting of a biased random walk characterized by periods of forward motion interrupted by sharp turns, in which the worm changes its orientation in a random manner [138, 139]. Within that context, increased activity of the AIB interneuron leads to more turns, and thus to a decreasing ability to maintain the current course. Oppositely, AIB inhibition would compel the worm to keep moving in the same direction.

How do the activities of the ASER and AIB neurons regulate the experience-dependent chemotaxis shown in Fig. 1.3? A large body of experimental knowledge has been amassed in recent years [65, 132, 133, 134, 135] to put together a picture of what happens. ASER is an OFF sensory neuron, i.e. it is activated (it depolarizes) upon decreases in NaCl concentration [140]. This can be seen in the bottom row of the 2×2 cartoon matrix shown in Fig. 4.1, where the activity of ASER is shown schematically in response to a down-step in salt. ASER activation in response to such stimulus occurs in both high- and low-salt cultivation conditions (left and right columns of the cartoon matrix, respectively). Conversely, ASER hyperpolarizes (it is inhibited) by an increase in NaCl, again under both cultivation conditions (top row in Fig. 4.1). We note that the changes in ASER activity in response to salt steps need to be transient, to prevent the worm from being stuck in the same direction of motion for long periods of time. Experiments show that the timescale of these activity changes is of the order of seconds [65,

140, 141].

It is worth emphasizing from the discussion above that the response of ASER to a change in salt concentration is the same irrespective of whether the worm had been previously cultivated in high or low salt conditions (compare the behavior of ASER across a given row in the left and right columns in the matrix of Fig. 4.1, respectively). How are then past experiences encoded in the system? What changes between the two cultivation conditions is the effect that ASER has on its target neuron AIB [65, 133]: under high-salt cultivation ASER *activates* AIB (red arrows, left column in the matrix of Fig. 4.1), whereas cultivation in low salt leads to ASER *inhibiting* AIB (blue blunt-end arrows, right column in the figure). The nature of the neuronal connection does not depend on whether the current environmental conditions correspond to an up-step or a down-step of salt. Additionally, the timescale of the changes in the nature of connection from ASER to AIB (from excitatory to inhibitory) has to be long enough to maintain a "memory" of the past experiences (on the order of minutes [132], not shown in the figure).

In summary, the combination of two orthogonal effects (current salt changes affecting the activity level of ASER, and past experiences affecting the way in which ASER acts upon AIB) enables combinatorially the four different actions that underlie experience-dependent salt chemotaxis in *C. elegans*:

- A salt up-step after high-salt cultivation leads to ASER inhibition and an excitatory connection between ASER and AIB, which in turn leads to AIB inhibition and motion forward (top left panel in the matrix of Fig. 4.1).

- A salt up-step after low-salt cultivation leads to ASER inhibition and an inhibitory connection between ASER and AIB, which in turn leads to AIB activation and increased turns (top right panel in the figure).

- A salt down-step after high-salt cultivation leads to ASER activation and an excitatory connection between ASER and AIB, which in turn leads to AIB activation and increased turns (bottom left panel in the figure).

- A salt down-step after low-salt cultivation leads to ASER activation and an inhibitory connection between ASER and AIB, which in turn leads to AIB inhibition and motion forward (bottom right panel in the figure).

These four situations lead to the expectation that the worm should be able to move towards or away from high salt concentrations depending on whether

it had previously experienced high- or low-salt conditions, respectively. However, it is still unclear whether this behavior would take place in a gradient, where the perceived changes in salt concentrations are continuous instead of consisting of finite steps. Filling this gap can be accomplished by modeling mathematically the neural dynamics described above in an *in silico* gradient, and quantifying statistically the trajectories of simulated worms undergoing biased random walks. In order to implement this model in a biologically realistically manner, however, we first need to establish the molecular mechanisms underlying the neural dynamics previously outlined.

4.2 Molecular determinants of experience-dependent chemotaxis

As discussed above, the plasticity of salt chemotaxis in *C. elegans* relies on two types of encoding, which need to be explained molecularly: the encoding of the current environment in the activity of ASER, and the encoding of past experiences in the nature of the connection between ASER and AIB. In what follows we discuss the two processes separately.

4.2.1 Molecular encoding of current environmental conditions

We explained in Section 4.1 above that ASER responds to steps in NaCl by transiently depolarizing (hyperpolarizing) in response to a down-step (up-step) in salt. No explicit molecular mechanisms underlying such a response have been reported yet, to our knowledge. The ASER response to a salt step is an instance of perfect adaptation, since after the transient, the activity of the neuron goes back to the level it had prior to the change in salt concentration (even though the NaCl level is now different). This property can be used as a constraint when searching for a potential molecular circuitry that exhibits this response [34, 35, 142]. In what follows we hypothesize a specific molecular mechanism based on a systematic search of the *C. elegans* literature on chemosensory signal transduction, constrained by the need of explaining perfect adaptation.

ASER senses salt stimuli through guanylyl cyclase receptors (rGCs) [143]. These membrane proteins consist of two parts: an extracellular receptor domain and an intracellular guanylyl cyclase activity domain. When salt binds the extracellular domain of rGC, cyclase activity is inhibited and signaling is silenced. Conversely, signaling is initiated when salt is removed and the intracellular cyclase domain induces the production of cyclic guanosine monophosphate (cGMP) [143]. cGMP binds to and opens cGMP-gated calcium channels in ASER, leading to an influx of calcium ions, and con-

sequently to neuronal depolarization. In parallel, cGMP activates PKG (a cGMP-dependent protein kinase, also called EGL-4 in the *C. elegans* literature). PKG is known to be required in ASER for calcium signals to arise in response to salt [143], but its targets and role are unknown. One of the proposed hypothesis is that PKG inhibits cGMP-gated channels, thereby inhibiting the influx of calcium ions [143]. Together, these interactions take the form of an incoherent feedback circuit between cGMP, PKG and Ca^{2+}, with NaCl acting as upstream input. This is shown in Fig. 4.2 (molecular circuit inside the triangle representing ASER, top of the figure). Incoherent feedforward circuits are among a handful of molecular circuits that can exhibit perfect adaptation [34, 35, 142], which makes this hypothesis potentially attractive. In the following section we will include this feedforward circuit in our integrative model of experience-dependent behavior.
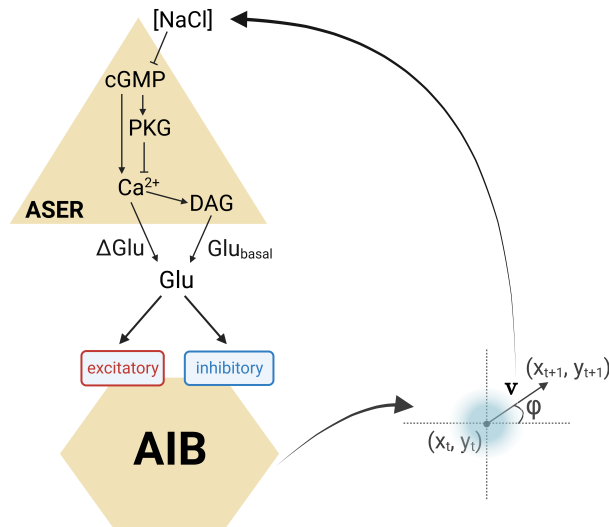
Figure 4.2: **NaCl chemotaxis sensorimotor circuit**. Salt inhibits the activity of the sensory neuron ASER (triangle), which in turn affects the activity of the interneuron AIB (hexagon). The state of AIB controls the motion of the worm by modulating the probability at which random reorientations of its motion occur. Finally, the motor activity of the organism feeds back on the level of salt that it senses, since the salt concentration will depend on the worm's location. The molecular components considered in our integrative model, and the interactions between them, are shown.

4.2.2 Molecular encoding of past experiences

The experience-dependent change of synapse polarity between ASER and AIB shown schematically in Fig. 4.1 is known to arise through glutamate signaling. ASER releases glutamate upon activation, which is sensed by

AIB through two types of glutamate receptors: an excitatory glutamate-gated cation channel and an inhibitory glutamate-gated chloride channel [133, 134]. Crucially, these two receptors have different sensitivities: the inhibitory receptor has a smaller glutamate threshold than the excitatory one [134]. This leads to a U-shaped response of AIB to glutamate, as shown in Fig. 4.3.
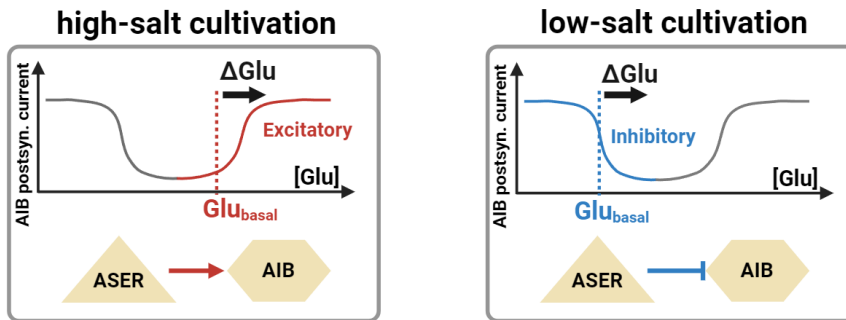
Figure 4.3: **Dual regulation of AIB by ASER encodes past experiences.** Response of AIB in terms of its postsynaptic current as a function of glutamate levels. Top: under high-salt cultivation conditions, the synapse operates in the right-hand side of the U curve, thus acting in an excitatory manner. Bottom: under low-salt cultivation conditions, the synapse operates in the left-hand side of the U curve, thus acting in an inhibitory manner.

Given this non-monotonic response of AIB to ASER, the worm can set the nature of the synaptic connection to be either excitatory or inhibitory by operating in high or low glutamate concentration ranges, respectively. Recently it was proposed, on the basis of experimental observations, that this can be achieved by controlling the level of basal glutamate release by ASER [134]. This strategy is based on the way in which synaptic transmission occurs in *C. elegans*: unstimulated sensory neurons release a basal amount of neurotransmitter, which gradually increases or decreases based on sensory perception [144, 145, 146].

In our case, when basal glutamate is low, the synapse operates in a predominantly inhibitory mode (blue section of the response curve in Fig. 4.3, bottom panel). Conversely, when basal glutamate is high, the effect of ASER's additional glutamate release will be excitatory (red section of the postsynaptic current curve in Fig. 4.3, top panel). The intriguing question now is how the level of basal glutamate released by ASER is regulated in an experience-dependent manner: for high-salt cultivated animals the basal release should be high, while under low-salt cultivation basal glutamate should be low.

Glutamate release by *C. elegans* sensory neurons is known to be up-regulated by the DAG/PKC-1 signalling pathway [144]. In particular, DAG/PKC-1 has been found to up-regulate glutamatergic transmission by ASER [134]. Furthermore, it has been shown that DAG levels in ASER are dynamically regulated in response to step changes in NaCl concentration [132], with DAG increasing (decreasing) transiently in a response to down-step (up-step) in salt. Taken together, these features suggest a possible explanation of how basal glutamate release is regulated in an experience-dependent manner. Specifically, high-salt cultivated animals face a down-step in salt, and thus a transient increase in DAG, when placed in the middle of a gradient [132]. Such an increase in DAG would produce an increase in basal glutamate, leading to an excitatory connection between ASER and DAG, as expected (left column in Fig. 4.1 and top panel in Fig. 4.3). Conversely, for low-salt cultivated animals NaCl concentration is increased when transferred to the gradient plate, which lowers DAG levels [132]. This decreases basal glutamate release, leading to an inhibitory postsynaptic response in AIB (right column in Fig. 4.1 and bottom panel in Fig. 4.3). Notably, DAG levels are maintained for tens of minutes in the ASER neuron [132], which coincides with the time span necessary to guide the worm towards the cultivation concentration [134].

The molecular and cellular processes described above seem to explain the experience-dependent character of salt chemotaxis in *C. elegans*. On the other hand, the connection between the two modes of encoding is still unclear, as is the extrapolation of responses to step changes in salt to a gradient, as mentioned in Section 4.1 above. To put all the ingredients together and bridge the gap between molecular/cellular mechanisms and behavior, we now implement an integrative mathematical model that bridges the molecular, cellular and organism scales.

4.3   An integrative model of experience-dependent behavior

In this Section we describe how we built our mathematical model based on the previously described experimental observations. As depicted in Fig. 4.2, our model includes a sensory neuron, ASER, that affects the activity of an interneuron, AIB, which in turn regulates the motor system of the worm. This cellular description is complemented at the molecular level by specific circuits regulating the responses of the two neurons, and at the behavioral level by a description of how the activity of AIB affects the motor output of the organism, which leads to motion changes (or lack thereof) in a gradient, and thus to changes in the sensed NaCl, closing the loop.

4.3.1   An intracellular sensory feedforward circuit

We begin with the dynamics of the sensory neuron ASER. As mentioned above, ASER produces Ca^{2+} transients in response to NaCl concentration changes [140]. Our aim is to model this response with a biologically grounded yet simple circuit. We have not found in the literature this kind of model for ASER, or for any other *C. elegans* sensory neuron. There are effective models that use explicit derivative-like operations to account for the transduction of a salt step into a Ca^{2+} pulse [73, 74]. The advantage of those frameworks is that they are easy to construct and tune, but they do not provide a molecular basis for the derivative-like operations mentioned above. On the other hand, there are physiologically grounded models for *C. elegans* sensory neurons, such as the neurons AWC [147] and ASH [148], but they are overly detailed models, which are difficult to tune and lack experimental evidence to support some of the assumptions made and the parameter values.

In that context, a parsimonious framework is missing, biologically-grounded and yet not too complex. The feedforward circuit proposed in Section 4.2.1 above is an adequate choice for such a model. As we described there (see also Fig. 4.2), cGMP activation in ASER affects Ca^{2+} influx in two ways: directly via the opening of cGMP-gated channels (leading to an increase in Ca^{2+} influx), and indirectly via the activation of the cGMP-gated channel inhibitor PKG (leading to a decrease in Ca^{2+} influx). The dynamics of this incoherent feedforward circuit can be represented by the following system of coupled differential equations:

$$\frac{dcGMP}{dt} = \alpha \frac{1}{1 + [\text{NaCl}]/K} - \delta_{\text{GMP}} \cdot cGMP, \tag{4.1}$$

$$\frac{dPKG}{dt} = \gamma \cdot cGMP - \delta_{\text{PKG}}PKG, \tag{4.2}$$

$$\frac{dCa^{2+}}{dt} = \beta\sigma(cGMP - PKG) - \delta_{\text{Ca}}Ca^{2+}, \tag{4.3}$$

The first term in Eq. (4.1) represents the inhibition of rGC-mediated cGMP production by NaCl, as discussed in Section 4.2.1 above [143]. To model this we have chosen a standard repressing Michaelis-Menten function [33]. The first term in Eq. (4.2) represents the activation of PKG by cGMP, assumed to be linear. Equation (4.3) corresponds to the dynamics of the variable Ca^{2+}, which represents the change in calcium levels relative to its baseline (thus Ca^{2+} can assume positive and negative values). In particular, the first term in Eq. (4.3) represents the calcium influx due to the opening of cGMP-gated channels, which are inhibited by PKG. According to this expression, calcium influx increases (with respect to its baseline) when cGMP

surpasses PKG according to a threshold function given by the sigmoid function

$$\sigma(x) = \tanh(bx)\,. \tag{4.4}$$

The last terms in Eqs. (4.1)-(4.3) represent the decay of the three species. The values of these decay rates (see Table 4.1) are chosen such that the timescale of calcium dynamics is fast enough (on the order of seconds) to avoid locking the organism in a fixed direction of motion for too long. The resulting time traces of Ca^{2+} levels inside ASER in response to NaCl steps are shown in Fig. 4.4.

All parameter values can be found in Table 4.1. We estimated the concentration units of the model variables per cell from the available literature: for cGMP (μM) [149], PKG (μM) [150], Ca^{2+} (μM) [151], DAG (lipid concentration in μM) [152] and Glu (mM) [153].

Param.	Value	Eq.	Param.	Value	Eq.
α	825 μM $\cdot$ s^{-1}	4.1	θ	0 μM	4.7
K	300 mM	4.1	τ	0.1 s	4.9
δ_{GMP}	50 s^{-1}	4.1	ω_{inh}	10.0 mV	4.9
γ	0.12	4.2	ω_{exc}	50.0 mV	4.9
δ_{PKG}	0.12 s^{-1}	4.2	V_{rest}	-55.0 mV	4.9
β	1.0 μM $\cdot$ s^{-1}	4.3	b_{exc}	27 mM^{-1}	4.11
δ_{Ca}	1.0 s^{-1}	4.3	θ_{exc}	1.481 mM	4.11
b	2.0 μM^{-1}	4.4	b_{inh}	92 mM^{-1}	4.10
β_{DAG}	0.7 s^{-1}	4.5	θ_{inh}	0.054 mM	4.10
δ_{DAG}	0.001 s^{-1}	4.5	ω_{low}	0.03 s^{-1}	4.13
α_{Glu}	1.345 mM	4.7	ω_{high}	50.3 s^{-1}	4.13
β_{Glu}	0.055 mM	4.7	V_{low}	-50.035 mV	4.13
α_{Δ}	1000	4.7	v	0.022 cm/s	4.12

Table 4.1: Parameter values of the experience-dependent chemotaxis model in *C. elegans*.

Figure 4.4 shows that ASER depolarizes (its Ca^{2+} levels increase) in response to a NaCl decrease, and hyperpolarizes when NaCl increases. Experimentally, the Ca^{2+} response to a NaCl downstep is more pronounced than to an upstep [140]. However, in our model the responses are considered symmetric, as show in Fig. 4.4. This simplification has already been used in other models of *C. elegans* navigation [141], for the same parsimonious reasons as ours. The parameters of Eqs. (4.1)-(4.4) were chosen to match the experimental response time of ASER's Ca^{2+} levels upon a NaCl decrease (defined as the time to reach half the distance between the peak

Figure 4.4: **Simulated response of ASER's activity to NaCl steps**. The intracellular Ca^{2+} concentration of ASER is shown for a NaCl upstep (a) and downstep (b). The response time of the model is in agreement with the one measured experimentally [134] ($\tau_{1/2} \sim 10$ s).

and resting level) [134]. Specifically, the response time to a 25 mM NaCl step is ~ 10s, as depicted in Fig. 4.4.

4.3.2   A dual neuronal signaling process

The response of DAG to changes in NaCl concentration that we described in Section 4.2.2 above has been shown to be caused to changes in the neural activity of ASER [132]. Specifically, ASER's intracellular Ca^{2+} enhances DAG production, most likely via the PLC-β/EGL-8 pathway [134]. We represent this effect in our model via the following equation:

$$\frac{d\text{DAG}}{dt} = \beta_{\text{DAG}}Ca^{2+} - \delta_{\text{DAG}}\text{DAG}, \qquad (4.5)$$

where DAG up-regulation by Ca^{2+} is modeled as a linear activation, and the variable represents changes in DAG levels relative to its baseline (and thus it can assume positive or negative values). The simulated responses of DAG activity in the ASER neuron for both a salt upstep and downstep are shown in Fig. 4.5.

Figure 4.5 shows that DAG levels decrease upon a sudden NaCl increase (panel a), while they rise upon a sudden NaCl decrease (panel b), in both cases mediated by Ca^{2+}. Similarly to the case of the sensory feedforward circuit discussed in Section 4.3.1 above, the parameters of Eq. (4.5) were chosen to match the experimentally observed decay time of DAG [132, 134], which is ~ 10 min.

The next step in our model is to describe the effect of the sensory neuron ASER on the turn neuron AIB. As discussed in Section 4.2.2, ASER com-
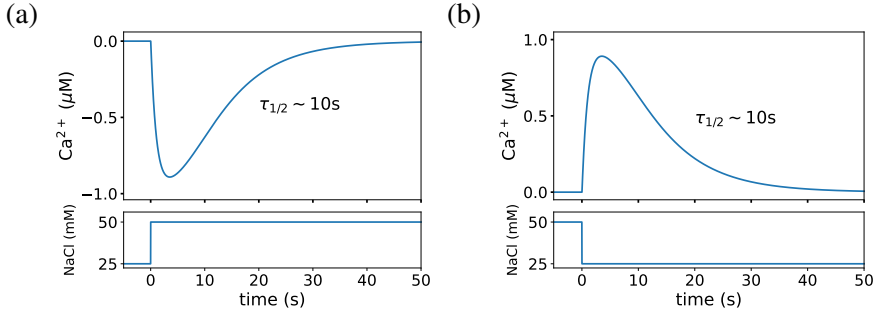
(a)

(b)
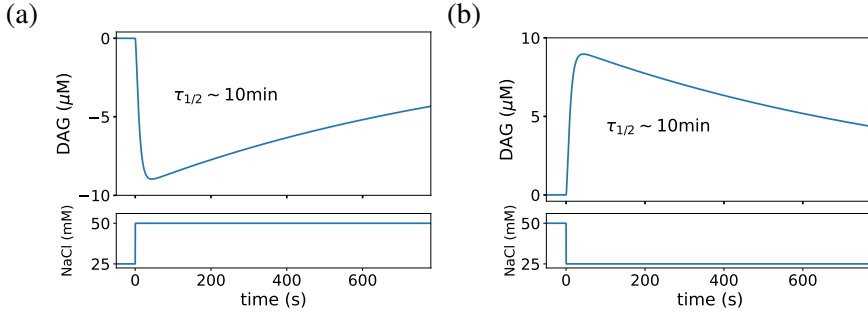
Figure 4.5: **Simulated response of DAG levels to NaCl steps.** The intracellular DAG concentration in ASER is shown for a NaCl upstep (a) and downstep (b). The model response time is in agreement with the measured in Ref. [132] ($\tau_{1/2} \sim 600$ s).

municates with AIB synaptically via the neurotrasmitter glutamate. The glutamate released by ASER has two components: a slow basal level $\text{Glu}_{\text{basal}}$ controlled by DAG, and a fast instantaneous level ΔGlu controlled by the intracellular calcium concentration of ASER [134]:

$$\text{Glu} = \beta_{\text{Glu}} + \text{Glu}_{\text{basal}} + \Delta\text{Glu} \tag{4.6}$$

$$= \beta_{\text{Glu}} + \alpha_{\text{Glu}}\text{H}(\text{DAG} - \theta) + \alpha_{\Delta}\text{Ca}^{2+}, \tag{4.7}$$

where β_{Glu} is a (small) background glutamate level. We assume that basal glutamate is produced when DAG exceeds a threshold value θ, as described by the Heaviside step function H(x) (which is 1 when $x \geq 0$ and 0 otherwise). The instantaneous excess glutamate, ΔGlu, is assumed in turn to increase linearly with the intracellular Ca^{2+} levels of ASER. It is worth mentioning that $\text{Glu}_{\text{basal}}$ and ΔGlu have different timescales, corresponding to those of their activating factors: $\text{Glu}_{\text{basal}}$, regulated by DAG, has a characteristic time ~ 10 minutes [132], whereas ΔGlu operates in time scales on the order of ~ 10 seconds, corresponding to the Ca^{2+} dynamics of ASER [65, 140, 141].

The total glutamate released by ASER acts upon AIB via the excitatory and inhibitory synapses discussed in Section 4.1, such that the dynamics of AIB's membrane potential is given by:

$$\tau\frac{dV_{\text{AIB}}}{dt} = \omega_{\text{inh}}S^{\text{inh}}(\text{Glu}) + \omega_{\text{exc}}S^{\text{exc}}(\text{Glu}) \tag{4.8}$$

$$- (V_{\text{AIB}} - V_{\text{rest}}), \tag{4.9}$$

where the first and second terms in the right-hand side represent the inhibitory and excitatory currents, respectively [133], with ω_{inh} and ω_{exc} denoting the weights of the corresponding connections. The synaptic currents

are assumed to depend on glutamate through the sigmoid functions

$$S^{\text{inh}}(x) = \frac{e^{-b_{\text{inh}}(x-\theta_{\text{inh}})}}{1 + e^{-b_{\text{inh}}(x-\theta_{\text{inh}})}} \tag{4.10}$$

$$S^{\text{exc}}(x) = \frac{1}{1 + e^{-b_{\text{exc}}(x-\theta_{\text{exc}})}}, \tag{4.11}$$

where b_j and θ_j ($j = \text{exc}, \text{inh}$) correspond to the steepness and threshold of each synaptic function. The inhibition threshold is smaller than the excitation threshold (see Table 4.1), and as a result the overall response of V_{AIB} to glutamate is U-shaped, as shown in Fig. 4.3 above. This enables two different responses to the fast transient pulse in glutamate, ΔGlu, caused by present changes in NaCl such as a downstep (Fig. 4.6a). For low-salt cultivated animals $\text{Glu}_{\text{basal}}$ is 0, so the postsynaptic response is inhibitory (Fig. 4.6b, blue curve). On the contrary, for high-salt cultivated animals $\text{Glu}_{\text{basal}}$ is high, giving rise to an excitatory postsynaptic response (red curve).
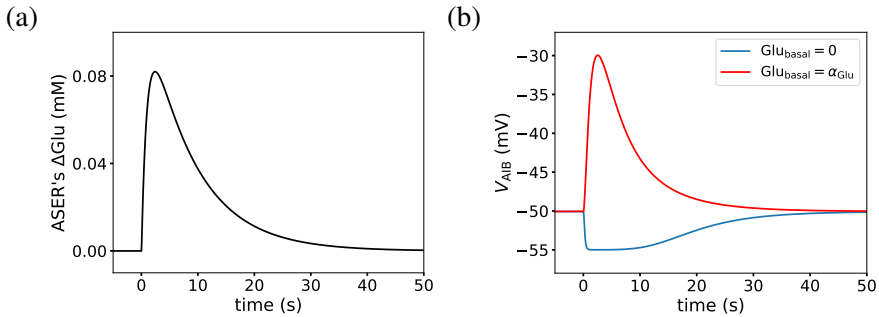
Figure 4.6: **Experience-dependent V_{AIB} response.** (a) Instantaneous change of glutamate released by ASER ($\Delta\text{Glu} = \alpha_\Delta \text{Ca}^{2+}$) in response to a NaCl downstep. (b) corresponding AIB response to the ΔGlu depicted in the left panel. Blue curve: inhibitory response for high salt cultivation ($\text{Glu}_{\text{basal}} = 0$). Red curve: excitatory response for low salt cultivation ($\text{Glu}_{\text{basal}} > 0$).

4.3.3   Effect on the worm's motion

Finally we need to couple the molecular and cellular dynamics described about to the worm's motion. To that end we take into account that AIB activation determines motor output, by producing instantaneous turning events that underlie the worm's pirouettes [154]. In this sense, our model assumes that during locomotion the body follows the head, allowing us to focus on the sensory-motor control of a point worm. At each point in time the worm is modeled as a point at coordinates $(x(t), y(t))$, with its head being directed

towards an angle $\varphi(t)$, as depicted in Fig. 4.2 and expressed mathematically by

$$\frac{d(x, y)}{dt} = (v \cos \varphi, v \sin \varphi), \tag{4.12}$$

where we assume that the worm moves at a fixed speed v.

Pirouettes are executed by resetting the orientation angle φ. The probability of a pirouette per unit time P_Ω is determined by the activation of the AIB turn neuron. We represent this by the following piece-wise monotonically increasing function of V_{AIB}:

$$P_\Omega = \begin{cases} \omega_{\text{low}} & \text{if } V_{\text{AIB}} \leq V_{\text{low}}, \\ \omega_{\text{high}} & \text{if } V_{\text{AIB}} > V_{\text{low}}, \end{cases} \tag{4.13}$$

where the parameters ω_{low} and ω_{high} represent base pirouette rates. When a pirouette is executed, the heading φ is instantaneously set to a random angle, drawn from a uniform distribution between 0 and 2π.

When the worm's position changes according to Eq. (4.12), *C. elegans* will sense a new NaCl concentration value, which will serve as new sensory input to ASER neuron (see Eq. (4.1) and curved arrows in Fig. 4.2). We now put all these pieces together to model the behavior of *C. elegans* in a NaCl concentration gradient for our two different past experiences (high and low salt cultivation).

4.4   Behavioral modeling

Having studied the response of the different molecular and cellular model variables to NaCl steps, we now aim to see whether this minimal sensory system, alongside with the simplified motor system also described above, can give rise to the behaviors observed experimentally when worms are placed in a continuous gradient, instead of facing sharp NaCl steps. To that end, we have followed the chemotaxis assay protocol depicted schematically in Fig. 1.3 and previously described in [65, 134]. In the experiment, worms were cultivated at a constant concentration of NaCl (25 mM, 50 mM, or 100 mM) for 6 hours. In those conditions, any perturbations in DAG levels during the pre-cultivation phase fully vanish and DAG activity returns to baseline. The animals are then transferred to the center of a plate with a salt gradient, and allowed to move freely for about ∼10 min. We have used a virtual gradient similar to the experimental one [65, 134], which has a low (∼30 mM) and high (∼95 mM) NaCl area, with a background salt concentration in the rest of the plate of 50 mM, as shown in Fig. 4.7. The
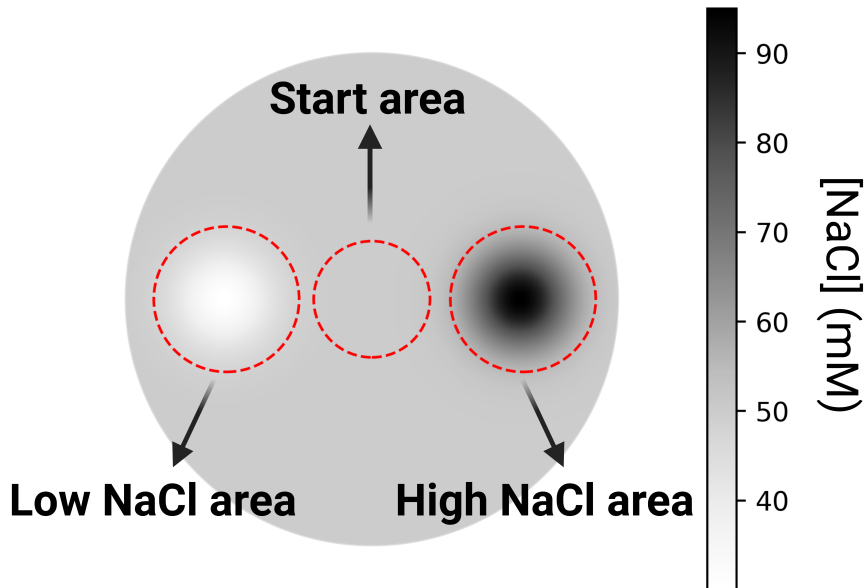
Figure 4.7: **Chemotaxis assay.** Virtual agar plate with NaCl gradient used in our simulations. The virtual worms are placed initially inside the start area, and the number of worms that reach the low and high NaCl areas by the end of the simulation are counted.
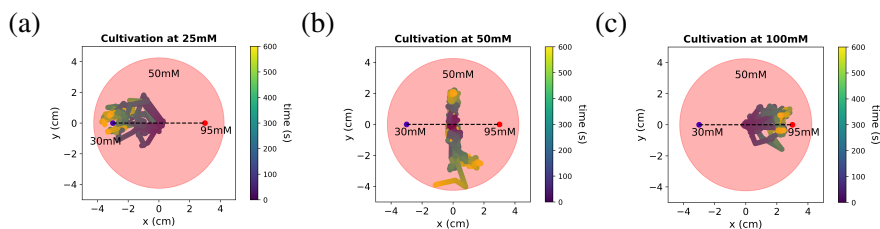
Figure 4.8: **Behavioral traces**. Trajectories of ten virtual worms during the chemotaxis assay. Animals are placed at the center of the gradient plate and allowed to move for 600 s. Trace color represents time. (a) Worms cultivated at low [NaCl] (25 mM) move towards the low NaCl area (∼30 mM). (b) Worms cultivated at the background [NaCl] of the gradient plate (50 mM) move around areas where [NaCl]=50 mM. (c) Worms cultivated at high [NaCl] (100 mM) migrate to the high NaCl area (∼95 mM).
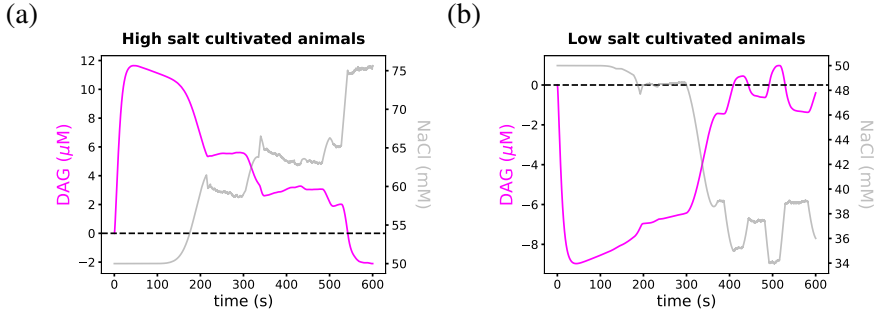
Figure 4.9: **DAG dynamics and perceived NaCl concentration during the chemotaxis assay.** Example time series of DAG levels during the chemotaxis assay. The dashed line shows the threshold θ of Eq. (4.7). (a) For high-salt cultivated animals DAG levels increase at the start of the assay due to the sensed decrease of [NaCl]. Increased DAG levels ensure an excitatory synapse between ASER and AIB, which guides the worm to higher [NaCl] areas. (b) For low-salt cultivated animals DAG decreased levels enable an inhibitory synapse between ASER and AIB, which guides the worm towards lower [NaCl] areas.

simulated gradient is given by the following equation:

$$[\text{NaCl}](x, y) = C_{\text{back}} + C_{\text{max}} e^{-\frac{(\mathbf{x} - \mathbf{x}_{\text{max}})^2}{2\sigma^2}}$$
$$- C_{\text{min}} e^{-\frac{(\mathbf{x} - \mathbf{x}_{\text{min}})^2}{2\sigma^2}} \tag{4.14}$$

We also tested our model using other NaCl gradient shapes, such as a unimodal gaussian and a conical function (linear with distance to the peak). In all cases, we obtained consistent results, which shows our results are not dependent on the particular shape of the gradient.

Figure 4.8 shows typical trajectories of ten virtual worms place in the gradient (4.14), as generated by our integrative model, with different initial orientations (φ in Eq. (4.12)), for pre-assay cultivations at 25 mM, 50 mM and 100 mM, respectively. As shown in the figure, cultivation with different salt concentrations leads to correspondingly different [NaCl] preferences in the chemotaxis assay, as seen experimentally [65]. The different behavioral preferences of Fig. 4.8 arise from the same minimal sensorimotor system of Fig. 4.2, without any change in the model parameters.

As explained before, the essential mechanism underlying this experience-dependent behavior is that DAG levels in ASER are dynamically regulated according to salt changes. To see this more clearly, Fig. 4.9 shows DAG levels during the chemotaxis assay for an representative virtual worm. For high-salt cultivated animals DAG increases at the start of the assay due to

the sensed [NaCl] decrease when they are transferred from the cultivation plate (where [NaCl] is 100 mM) to the center of the gradient plate (where [NaCl] is ∼50 mM). This increase in DAG levels above the threshold θ of Eq. (4.7) (dashed line in Fig. 4.9a) leads to an excitatory synapse between ASER and AIB, which gives rise to high salt attraction. As we can see in Fig. 4.9a, as the worm migrates to higher [NaCl] areas in the plate, DAG levels decrease accordingly.

The situation is reversed in the case of low-salt cultivated animals. There, DAG decreases at the start of the assay due to the worm being transferred from its cultivation plate (where [NaCl] is 25 mM) to the center of the gradient plate (where [NaCl] is ∼50 mM). Decreased DAG levels lead to an inhibitory synapse between ASER and AIB, which gives rise to low salt attraction. As we can see in Fig. 4.9b, DAG levels increase according to migration towards lower [NaCl] areas.

4.5   Chemotaxis assay for simulated mutant worms

To validate quantitatively the model described so far, we now compare the behavior of wild-type worms with mutants where some system components are altered or eliminated altogether. Some of the mutants studied have been characterized experimentally, and thus are here used as validations of the model, while others have not been studied in the laboratory, and can thus be considered model predictions.

To quantify the behavior of the worms we use the chemotaxis index (C.I.), defined as [65]

$$\text{C.I.} = \frac{N_{\text{High}} - N_{\text{Low}}}{N - N_{\text{Start}}}, \tag{4.15}$$

where N_{High} (N_{Low}) denotes the number of animals in the high (low) NaCl area, i.e. within a 1.05 cm radius from $\mathbf{x}_{\max}$ ($\mathbf{x}_{\min}$) –see Eq. (4.14)–, at the end of the assay. N is the total number of simulated worms, and N_{Start} is the number of animals within a 1-cm radius from the start point at the end of the assay (the center of the plate). We consider $N = 100$ worms in every assay.

A C.I. of 1 and -1 represents total preferences for high and low concentrations, respectively. A C.I. of 0, on the other hand, can represent a preference for the background concentration (50 mM), equal distribution of the population between both end areas, or a random distribution. All the parameters characterizing the NaCl gradient and the C.I. areas are given in Table 4.2.

Figure 4.10 shows the chemotaxis indices exhibited by the wild-type (WT) worms and eight mutants for low and high NaCl pre-cultivation concen-

Parameter	Value
C_{max}	45.0 mM
C_{min}	20.0 mM
C_{back}	50.0 mM
$\mathbf{x}_{\text{max}}$	(3.0, 0.0) cm
$\mathbf{x}_{\text{min}}$	(-3.0, 0.0) cm
σ	0.7 cm
R	4.25 cm

Table 4.2: Parameter values of the salt gradient of eq. (4.14).

trations, and for the control case in which the worms are cultivated at the intermediate assay concentration (50 mM). In the WT case, the chemotaxis indices confirm the behavior reported in Fig. 4.8: worms cultivated at low [NaCl] (25 mM) are attracted to low salt concentrations (C.I. $\sim$-1), whereas animals cultivated at high [NaCl] (100 mM) are attracted to high salt concentrations (C.I. $\sim$1). Lastly, for worms cultivated at the background concentration of the gradient plate (50 mM), the C.I. $\sim$0, which corresponds in this case to a preference for that same concentration. These chemotaxis indices are in close agreement with the experimental results of Ref. [134].
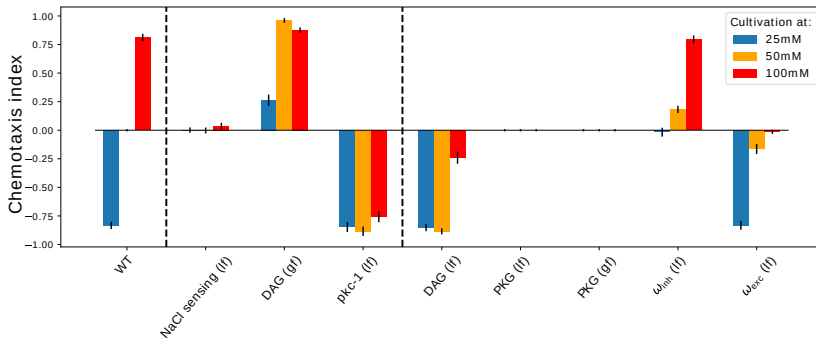
Figure 4.10: **Chemotaxis index for different pre-assay cultivations**. Results for wild-type worms (WT) and eight mutants are displayed. Mean $\pm$ s.e.m.; $n = 6$ assays. 100 worms were simulated within each assay.

Besides the wild-type worms, Fig. 4.10 shows the chemotaxis indices for two types of mutants. Specifically, the three cases shown in the middle section of the figure correspond to animals that have been previously studied experimentally in a gradient similar to the one of Fig. 4.7. Additionally, the five cases at the right of the plot correspond to mutants for which there are not experimental measurements, to our knowledge.

The first mutant corresponds to NaCl sensing loss-of-function (lf), which is associated with the inhibition on cGMP production by NaCl. We have modeled this situation by decreasing the value of the parameter α in Eq. (4.1). As can be seen in Fig. 4.10, the C.I. for this mutant is close to zero irrespective of the pre-assay cultivation. This result coincides with the one reported in Ref. [65], where the authors examined a mutant strain severely impaired in its ability to sense chemicals (*dyf-11*).

Next we aimed at replicating a gain-of-function (gf) mutation on the DAG/PKC-1 signalling pathway, which corresponds to a higher baseline level of DAG. To that end, we added in Eq. (4.5) a constant production rate α_{DAG} (independent of Ca^{2+} levels):

$$\frac{d\mathrm{DAG}}{dt} = \alpha_{\mathrm{DAG}} + \beta_{\mathrm{DAG}}Ca^{2+} - \delta_{\mathrm{DAG}}\mathrm{DAG} \qquad (4.16)$$

As shown in Fig. 4.10 for DAG (gf), these mutant worms migrate towards higher NaCl concentration regardless of the at pre-assay cultivation concentration. This can be understood by taking into account that as DAG levels are increased, the worms are mostly in the regime of an excitatory synapse between ASER and AIB for all pre-assay conditions, which explains the resultant overall high salt attraction. This behavior agrees with experimental results of a gf mutant in the DAG pathway (*egl-30*) [65].

The DAG/PKC-1 signalling pathway has been further explored experimentally with a PKC-1 loss of function (lf) mutant [134]. PKC-1 is a protein kinase downstream of DAG, which regulates the basal glutamate release in ASER ($\mathrm{Glu}_{\mathrm{basal}}$ in our model) by modulating the phosphorylation of a target protein. We simulated this lf mutant by setting $\alpha_{\mathrm{Glu}} = 0.0$ in Eq. (4.7), which leads to a constitutively low level of $\mathrm{Glu}_{\mathrm{basal}}$. In this case, the model predicts (fourth set of bars in Fig. 4.10) that worms with this mutation have a preference for low salt concentrations irrespective of the pre-assay cultivation conditions. These results are in agreement with the ones reported in Ref. [134] for PKC-1 lf mutants.

Another way of decreasing the activity of the DAG/PKC-1 signalling pathway is by acting directly on DAG. We implemented this perturbation by adding a constant degradation rate in Eq. (4.5). Similarly to the PKC-1 lf mutant (and oppositely to the DAG gf mutant) the DAG baseline is decreased, which leads to a predominantly inhibitory synapse between ASER and AIB. Consequently, the model predicts again that worms will move toward lower NaCl concentrations for all pre-assay conditions, as shown in Fig. 4.10. This is similar to the behavior of the PKC-1 lf mutant described above, but in this case the behavior is due to low DAG levels, instead of low

Glu_{basal} release from ASER. Interestingly, in the DAG lf mutant worms cultivated at high salt concentrations (100 mM), the attraction to low salt concentration is weaker than in PKC-1 lf mutants discussed above.

To explore our hypothesis that NaCl sensory transduction takes place via a feedforward circuit mediated by PKG, we next simulated loss- and gain-of-function PKG mutants. We did so by setting the value of γ in Eq. (4.2) to zero or by rising its value, respectively. In both cases, worms are predicted to move randomly for all cultivation conditions, as shown in Fig. 4.10. The fact that these opposite mutants lead to the same behavior can be explained from the symmetric response of the AIB neurons to low and high glutamate levels, as given by the U-shaped response curve discussed in Section 4.3.2 and shown in Fig. 4.3 above. Low PKG levels in the lf mutant lead to consistently high Ca^{2+} levels, which places the operating point of the neuron in the saturating region to the right of the AIB response curve shown in Fig. 4.3, for which high AIB activity and consequently high turn probability (and random motion of the worm) irrespective of how sensed NaCl is changing. In the PKG gf mutants, in turn, Ca^{2+} levels are consistently low, which places the neuron in the saturating region to the left of the AIB response curve (see again Fig. 4.3), for which AIB activity is also high, leading once again to frequent turns and random motion in the NaCl gradient.

Finally, we used the model to probe the relevance of the dual synaptic character in the experience-encoding, by considering loss-of-function mutants that alter the inhibitory and excitatory strengths of glutamate signaling from ASER to AIB. Our simulations show that when the inhibitory current in AIB is eliminated by setting $\omega_{inh} = 0.0$ in Eq. (4.9), worms cultivated at low [NaCl] lose their low-salt attraction (next-to-last case in Fig. 4.10), while high-salt attraction is retained for worms cultivated at high [NaCl]. In turn, when the excitatory current in AIB is eliminated by setting $\omega_{exc} = 0.0$, high-salt cultivated worms do not have a [NaCl] preference, while the behavior of low-salt cultivated worms stays the same as the WT (last case in Fig. 4.10). All the modified parameter values used for the mutants can be found in Table 4.3.

4.6   Discussion

In this work we have developed a mechanistic model that captures experience-dependent chemotaxis to NaCl in *C. elegans*. Specifically, we wanted to model how worms migrate to the salt concentration at which they have been previously fed [65]. Through a set of elegant experiments, Yuichi Iino and collaborators have identified the key molecular and cellular factors associ-

Mutant	Parameter	New value	Equation
NaCl (lf)	α	$0.0825\ \mu\mathrm{M}\cdot\mathrm{s}^{-1}$	(4.1)
DAG (gf)	α_{DAG}	$0.01\ \mu\mathrm{M}\cdot\mathrm{s}^{-1}$	(4.16)
pkc-1 (lf)	α_{Glu}	$0.0\ \mathrm{mM}$	(4.7)
DAG (lf)	α_{DAG}	$-0.01\ \mu\mathrm{M}\cdot\mathrm{s}^{-1}$	(4.16)
PKG (lf)	γ	0.0	(4.2)
PKG (gf)	γ	1.0	(4.2)
ω_{inh} (lf)	ω_{inh}	$0.0\ \mathrm{mV}$	(4.9)
ω_{exc} (lf)	ω_{inh}	$0.0\ \mathrm{mV}$	(4.9)

Table 4.3: Parameter values for the *C. elegans* mutants.

ated with this behavior. In particular, DAG levels in the salt-sensing neuron ASER are regulated in response to the difference between the previously and currently perceived NaCl levels. DAG activity, in turn, affects the glutamate-modulated connection between ASER and the motor neuron AIB, which can be switched between excitatory and inhibitory. By this mechanism, animals are guided toward the NaCl concentration they have previously experienced.

Based on these experimental observations, we have built a minimal integrative sensorimotor model of the experience-dependent chemotaxis to NaCl. The model covers the molecular, cellular and behavioral scales within a parsimonious framework: it is biologically grounded yet not too overly complex. One of the salient features of our model is that we can explain the two experience-dependent behaviors, high-salt and low-salt attraction, with a single framework without any modification in the model parameters. Salt preference arises from dynamically regulating DAG levels according to changes in the perceived NaCl concentration. Besides being able to reproduce the observed chemotaxis behavior of wild-type worms, our minimal model also reproduces the behavior of mutants involving molecular elements of both the sensor and actuator components of the system. Additionally, we have simulated untested mutations in ASER circuitry and in post-synaptic AIB neuron, whose behavior constitute model predictions to be tested experimentally.

While our work is based on experimental measurements of ASER's calcium and DAG dynamics in response to step changes in NaCl concentration [132, 134, 140], the results of our model show that the proposed mechanism can also explain the observed behavior in continuous salt gradients. The model is also relevant because its essential principle, i.e. the modulation of the DAG signalling pathway, is not specific of chemotaxis to NaCl,

but is also involved in experience-dependent behaviors in response to other sensory cues such as temperature (thermotaxis) and volatile odorant (odor chemotaxis), among others [155, 156].

Finally, our model of NaCl chemotaxis is a suitable starting point to explore the interplay between different stimuli, such NaCl and nutrients. It has been shown that pairing starvation with exposure to NaCl reverses the well-fed behavior [58]: after being starved in the presence of high (low) NaCl, *C. elegans* moves towards low (high) concentrations if set in a gradient [65]. DAG dynamics is known to be located downstream of the insulin signaling pathway [132, 157], which is in turn required for the starvation response [64]. This could explain why the DAG response to NaCl changes is diminished in starved worms in comparison with the well-fed case [132]. Similarly to what we have done in this chapter, mathematical modeling could be used to put together these observations to provide us with an integrative perspective on how living organisms respond to multivariate time-dependent signals from their environment.

Chapter 5. Conclusions

Living systems, across the wide spectrum from single cells to multicellular organisms, have complex temporal information processing capabilities. Nevertheless, we are far from fully understanding their underlying mechanisms. In this Thesis we have analyzed how biological systems process information depending on their previous experiences, a feat that naturally requires taking into account the time-dependent character of an organism's environment. Our main interest was to try to help in the comprehension of how temporal information, such as the previous experience of the organism, or sensory stimuli that has some temporal statistics, is encoded in biological systems. To do so we have explored a wide range of dynamical behaviors. In the following, we provide an overview of the conclusions obtained in the three different systems we studied, and potential future directions of research for each one of them.

5.1 Habituation

Arguably one of the most remarkable information processing capability of living organisms is learning, which enables them to modify their behavior in response to past stimuli. The ability to learn has typically been attributed to neuronal organisms and the connectivity of their multicellular nervous systems. However, there is evidence for learning in unicellular eukaryotes. This raises the question of how learning is implemented outside the brain, in single cells. In Chapter 2, in order to provide conceptual insight in this direction, we investigate plausible molecular mechanisms underlying habituation, a kind of non-associative learning behavior.

We investigate models based on common cellular regulatory circuit architectures –the negative feedback and the feedforward motif– and plausible biochemical interactions among molecular species. We find that a combination of two such motifs yields systems that exhibit all hallmarks related to the habituation response to a single stimulus, including frequency and intensity sensitivity, potentiation of habituation and subliminal accumulation [2].

This work emphasises the remarkable capabilities of cells for processing information, with implications for unicellular and multicelluar organisms, and the evolution and mechanisms of learning. Apart from this, the study of habituation itself has recently re-emerged, since it was proven its relevance in intellectual disorders. Specifically, it was seen in *Drosophila* that habituation is related to intellectual disability, and it can serve as a potential target for pharmacologic intervention to treat it [158].

Concerning open perspectives for this project, a straightforward direction is to extend our habituation model to include the remaining hallmarks of habituation, which involve more than one type of stimuli (hallmarks #7, #8 and #9 of Table 1.1). In this case, two different stimuli would arrive to our system, but only one of them activates our habituation circuit. This would account for the stimulus specificity hallmark. To account for dishabituation, *i.e.* presentation of a different stimulus resulting in an increase of the decremented response to the original stimulus, we could consider an additional species that degrades the memories of our system. Lastly, habituation of dishabituation can be incorporated by considering a second habituation model for the new memory degrading species.

Another interesting perspective is to study differential signatures that could help discerning which of the four different circuit architectures we proposed is underlying habituation for a specific organism. This was done in the context of adaptation in order to discern single negative feedback (NF) and incoherent feedforward loop (IFF) motifs [159]. In that case, it was proven that oscillating stimuli help differentiate which of the both architectures is underlying adaptation for different living organisms. For habituation we would need to extend this, since we are considering concatenated NF and IFF, and also receptor/channel models.

5.2   Recurrent biological networks

In Chapter 3 we employed the reservoir computing paradigm to investigate the computational capabilities in the gene regulatory network (GRN) of *Escherichia coli*. Originating from the fields of machine learning and computational neuroscience, this paradigm defines a system comprising a network of interacting elements capable of processing complex temporal information, and simultaneously, being efficiently trainable. More specifically, the system consists of a reservoir, which is a subnetwork featuring recurrences —*i.e.*, cyclic paths— that encodes temporal information through its complex dynamics. The readout is a component downstream the reservoir, constituting a simple feed-forward structure capable of extracting pertinent

information from the transient multidimensional dynamics of the reservoir to make predictions or classifications. The key point of reservoir computing is that for the network to learn a certain task, it is only necessary to train the readout, and not the recurrent sub-network. In this sense, we worked under the assumption that the integration of information in regulatory networks operates based on the reservoir computing paradigm, *i.e.* it occurs dynamically at the system-wide scale, without the need for a specialized architecture but rather in a decentralized manner.

We found that the gene regulatory network of *E. coli* follows the reservoir computing structure: a small proportion of genes with recurrent regulatory interactions is upstream of most of the rest of the network, which has a fully feedforward topology (readout). We then focused our study in analyzing the temporal processing capabilities of the network's reservoir. We have first investigated the effect of the network dynamics in its memory capacity. In this regard, we saw that the *E. coli*'s reservoir has maximum memory capacity just above the onset of a transition from order to chaos, *i.e.* in the vicinity of the critical point (*edge of chaos*).

Furthermore, we have looked into whether the local topology of the GRN contributes to their memory encoding. We focused on three significant motifs of the reservoir: self-loops, mutual regulation (mutual feedback between two nodes) and feedforward loops (FFL). We saw indeed that network motifs with recurrencies (self-loops and mutual regulation) are more decisive for the reservoir's memory capacity than feedforward patterns, such as FFL. This goes in line with the idea that strictly feedforward architectures are incapable of awarding memory to a system.

An examination was also conducted to ascertain whether certain balance between activation and repression is needed within the reservoir in order to perform well in memory-demanding tasks. By artificially varying the activation/repression ratio of the reservoir, we saw that the optimal performance in two different tasks was encountered when the repression percentage was very close to the real one (40%). This phenomenon has been seen in cortical neural networks [117], but it has not been explored before in a gene regulatory setting.

Lastly, we identified smaller groups of genes within the *E. coli*'s reservoir, which have a good compromise between their size and performance across three different memory-demanding tasks, holding potential significance for experimental validation.

Related to this last point, a future outlook entails the pursue of experimental validation on gene regulatory networks working as computational reser-

voirs. Searching for evidence on reservoirs with a large number of genes is quite a challenging endeavour. This effort becomes a simpler task if we deal with a smaller-sized reservoir. On the other hand, in our study the nonlinear dynamics of the network has been largely simplified with a formalism used for neural networks. The real gene regulatory dynamics, with more realistic interactions and different time scales for each gene, would add more complexity to the network behavior and increase the memory of the system [160, 161, 162]. In this sense, this can consist of a possible direction to extend our present model.

5.3 Behavior

Lastly, in Chapter 4 we use a series of previously published experimental results to build a mechanistic model that captures the experience-dependent salt chemotaxis behavior in the nematode *C. elegans*. Specifically, when worms are set in a salt gradient, they migrate to the salt concentration (high or low) at which they have been previously fed [65]. Our model integrates the sensory aspects of the process, encompassing both molecular and cellular levels, with the motor features of the observed behavior at the organismal level, all within a unified framework. It is biologically grounded, including all experimentally identified necessary and sufficient components, without introducing artificial regulatory mechanisms. Simultaneously, it avoids unnecessary molecular details that could result in over-parameterization.

The model proposes specific molecular mechanisms for the encoding of current conditions and past experiences in key neurons associated with this response. A notable feature of the model is its ability to encompass both experience-dependent behaviors —specifically, high- and low-salt attraction— within a unified framework. This is achieved using the same circuit and without any alterations to parameter values based on the worm's prior experiences.

In addition to accurately replicating the chemotaxis behavior observed in wild-type worms, our minimal model also mimics the behavior of mutants affecting molecular elements in both the sensor and actuator components of the system. Furthermore, we have conducted simulations involving untested mutations in the ASER circuitry and post-synaptic AIB neuron. These simulations provide model predictions that can be experimentally tested.

Two separate branches of follow-up work can be distinguished. First, the model predictions can be tested experimentally. Second, the model can be further extended in several (non-exclusive) ways.

Regarding the first point, we have proposed a particular minimal circuit for the sensory neuron involved in chamotaxis, *i.e.* ASER. It consists of a molecular circuit with an incoherent feedforward loop architecture. In this sense, a next step can be pursuing experimental validation of such circuit. On the other hand, as we said before, we have simulated the behavior of untested mutants worms in the chemotaxis assay, which hopefully can be tested experimentally too.

Secondly, our model can be extended following different directions from its current state. One possibility is to extend the present model in order to include the two orientation strategies of the worm. In our work, we only modeled *klinokinesis*, which consists of a biased random walk characterized by periods of forward motion interrupted by sharp turns, in which the worm changes its orientation in a random manner [138, 139]. The second mechanism is called *klinotaxis* or steering, and is based on gradual (continuous) reorientations towards preferred directions by sampling in space [138]. Klinokinesis has been suggested to have a greater effect on experience-dependent chemotaxis, but the behavior is best achieved with both mechanisms acting together [65]. The minimal klinotaxis model by Izquierdo *et. al.* [73] has been implemented by us (data not shown), and can be easily incorporated to our model. Second, the model can be extended to look closer at the NaCl sensing circuit, adding the first layer interneurons downstream of ASER. This would give a more comprehensive view of the chemotaxis neuronal circuit.

Lastly, our NaCl chemotaxis model serves as a suitable starting point for exploring the interaction between different stimuli, such as NaCl and nutrients. Previous studies have demonstrated that associating starvation with exposure to NaCl can reverse the well-fed behavior [58]. Specifically, after experiencing starvation in the presence of high (low) NaCl, *C. elegans* migrates towards low (high) concentrations when placed in a gradient [65]. Moreover, the insulin signaling pathway, necessary for this starvation response [64], has a downstream target that is part of our proposed molecular circuit for the well-fed behavior.

Looking back, with these three projects we investigated a wide range of aspects in experience-dependent biocomputation. In that sense, this Thesis represents a small contribution to the exciting landscape of open avenues in the study temporal information processing in living systems.

Appendix A. Modeling habituation

A.1 Model equations

The network topologies investigated in this work are implemented as Ordinary Differential Equations (ODEs), assuming Michaelis Menten or mass action kinetics for the molecular reactions. Each molecular species can be either in its active (X_a) or inactive (X_i) state. We assume that the total concentration of each molecular species $X_{tot} = X_a + X_i$ is constant. We explicitly model the time evolution of the relative concentration of the active form of each species (X_a), normalized to this total (set to 1). Unless indicated otherwise, subscripts $_1$ and $_2$ refer to each of the two motifs in the model, k_i are the reaction rates, and K_i the Michaelis-Menten constants. S is the input. $\dot{x}$ stands for dx/dt.

For simplicity in what follows for all the species we drop the subscripts X_a and X_i. Instead, we call the active species X and the inactive one $(1 - X)$.

A.1.1 Concatenated IFF model

$$\dot{I}_1 = \text{SQW}(t) \times k_{Ia1}(1 - I_1) - k_{Ii1}I_1$$
$$\dot{M}_1 = I_1 \times k_{Ma1}(1 - M_1) - k_{Mi1}M_1$$
$$\dot{R}_1 = I_1 \times k_{Ra1}(1 - R_1) - Mk_{Ri1}\frac{R_1}{K_1 + R_1}$$
$$\dot{I}_2 = R_1 \times k_{Ia2}(1 - I_2) - k_{Ii2}I_2$$
$$\dot{M}_2 = I_2 \times k_{Ma2}(1 - M_2) - k_{Mi2}M_2$$
$$\dot{R}_2 = I_2 \times k_{Ra2}(1 - R_2) - M_2k_{Ri2}\frac{R_2}{K_2 + R_2}$$

A.1.2   Concatenated NF model

$$\dot{I}_1 = \text{SQW}(t) \times k_{Ia1}(1 - I_1) - k_{Ii1}I_1$$
$$\dot{M}_1 = R_1 \times k_{Ma1}(1 - M_1) - k_{Mi1}M_1$$
$$\dot{R}_1 = I_1 \times k_{Ra1}(1 - R_1) - Mk_{Ri1}\frac{R_1}{K_1 + R_1}$$
$$\dot{I}_2 = R_1 \times k_{Ia2}(1 - I_2) - k_{Ii2}I_2$$
$$\dot{M}_2 = R_2 \times k_{Ma2}(1 - M_2) - k_{Mi2}M_2$$
$$\dot{R}_2 = I_2 \times k_{Ra2}(1 - R_2) - M_2k_{Ri2}\frac{R_2}{K_2 + R_2}$$

A.1.3   Single IFF model

$$\dot{I}_1 = \text{SQW}(t) \times k_{Ia1}(1 - I_1) - k_{Ii1}I_1$$
$$\dot{M}_1 = I_1 \times k_{Ma1}(1 - M_1) - k_{Mi1}M_1$$
$$\dot{R}_1 = I_1 \times k_{Ra1}(1 - R_1) - Mk_{Ri1}\frac{R_1}{K_1 + R_1}$$

A.1.4   Single NF model

$$\dot{I}_1 = \text{SQW}(t) \times k_{Ia1}(1 - I_1) - k_{Ii1}I_1$$
$$\dot{M}_1 = R_1 \times k_{Ma1}(1 - M_1) - k_{Mi1}M_1$$
$$\dot{R}_1 = I_1 \times k_{Ra1}(1 - R_1) - Mk_{Ri1}\frac{R_1}{K_1 + R_1}$$

A.1.5   Receptor + IFF model

$$\dot{R}_r = k_aR_a - k_rR_r$$
$$\dot{R}_i = k_rR_r - \text{SQW}(t) \times k_iR_i$$
$$\dot{R}_a = \text{SQW}(t) \times k_iR_i - k_aR_a$$
$$\dot{I}_2 = R_a \times k_{Ia2}(1 - I_2) - k_{Ii2}I_2$$
$$\dot{M}_2 = I_2 \times k_{Ma2}(1 - M_2) - k_{Mi2}M_2$$
$$\dot{R}_2 = I_2 \times k_{Ra2}(1 - R_2) - M_2k_{Ri2}R_2$$

A.1.6   Receptor + NF cascade model

$$\dot{R}_r = k_a R_a + k_{FB} C_3 R_a - k_r R_r$$
$$\dot{R}_i = k_r R_r - \text{SQW}(t) \times k_i R_i$$
$$\dot{R}_a = \text{SQW}(t) \times k_i R_i - k_{FB} C_3 R_a - k_a R_a$$
$$\dot{C}_1 = R_a \times k_{a1}(1 - C_1) - k_{i1} C_1$$
$$\dot{C}_2 = C_1 \times k_{a2}(1 - C_2) - k_{i2} C_2$$
$$\dot{C}_3 = C_2 \times k_{a3}(1 - C_3) - k_{i3} C_3$$

A.2   Model simulations and habituation protocol

Given a model and a set of parameters (see A.3) we investigate the response and recovery of the model to trains of repetitive stimulation with different frequencies and intensities, in order to test for the various hallmarks of habituation. The repetitive stimulus is simulated as a square wave input function $\text{SQW}(t)$ (see equation in the previous section and Fig. 2.1) with fixed intensity (S) for the duration of stimulation (T_{on}) and zero input otherwise. We assume the model starts with all species inactive. In order to reduce numerical inaccuracies that can arise due to the sharp change in input, stimulating and non-stimulating sub-intervals are integrated consecutively, setting as initial condition for the next sub-interval the variable values of the last time point of the previous sub-interval. In Python, we integrated using the *odeint* routine from Scipy [163]. In C++, we integrated using the function `integrate const` from `boost`'s `odeint` library [164]. For each sub-interval, integration is initially performed with a relatively large maximum step size (10^{-2}) which is successively lowered down to 10^{-6} in case of integration failure.

Given the diversity of habituation times for different parameter values, for a given parameter set and stimulation protocol, at each stimulus we tested whether or not the system has habituated, and simulated only until that point. We only considered parameter sets that did habituate within 50 stimuli.

The final simulations shown in this thesis were performed in both C++ and Python and the coincidence of the habituation and recovery times doublechecked across the two methods.

A.3   Parameter search

Given a model, we searched for a suitable set of parameter values that would yield habituation, recovery, frequency and intensity sensitivity. We did not

specifically search for the rest of hallmarks, but found that they were also satisfied for the selected parameter sets.

(i) Definition of a suitable region in parameter space

For each model we first define a region of the parameter space where habituating trajectories are obtained. For that purpose, we initially chose frequencies in the ranges 5-20 and intensities in the ranges 5-20 and subsequently reduced or amplified them if needed. Analogously we did the same with T_{on} in the range 0.5-1.2. Then, we integrate for a maximum of 50 stimuli the system for random parameter values. For each period between two stimuli, the peaks and troughs of the output trajectory are extracted as the maxima and minima of the trajectory. This gives an array of peaks and troughs, respectively, on which the following filters were applied. If the parameter set satisfies all following points, the solution is considered "habituating", and if not, "non-habituating".

1) The array of peaks must not be empty.

2) The highest peak must not be found later than at the third position. This allows for some sensitization for the very first stimuli, which is a phenomenon that has been observed experimentally in habituating organisms [2, 89].

3) The first peak must not be much lower than the highest peak (by default not lower than 50% of highest peak).

4) All peaks after the highest peak must be monotonically decreasing.

5) There must be at least two peaks after the highest peak.

6) There must be a substantial difference between the highest and the lowest peak (by default at least 20% signal decrease).

7) There must be a substantial difference between the first few peaks and troughs (by default the difference between each normalized peak and trough must be at least 0.05). This serves the purpose of filtering out smoothly decaying curves.

8) Trough levels must not be too high (by default not higher than 60% of the highest peak).

9) The last trough must be almost zero (by default not higher than 2% of the highest peak).

10) The number of high troughs is limited (by default there must

not be more than five troughs which are higher than 10% of the
highest peak).

By analyzing the clusters of habituating and non-habituating solutions
in the space of pairs of parameters, we iteratively restrain each param-
eter range to encompass ranges where all responses are habituating.
The corresponding ranges for each model are shown in Table A.2
for the concatenated IFF model, Table A.3 for the concatenated NF
model, Table A.4 for the single IFF model, Table A.5 for the single
NF model, Table A.6 for the Receptor + IFF model and Table A.7 for
the Receptor + NF cascade model.

(ii) Search for parameters that enable frequency and intensity sensitivity
After defining the suitable region of the parameter space, we searched
for parameter sets that would yield habituating responses that sat-
isfy frequency and intensity sensitivity using an evolutionary algo-
rithm that iteratively modifies a population of solutions (parameter
sets) by mutating each parameter and evaluating the performance of
each solution with a cost function described below. In particular,
we used the implementation of the full Evolution-Strategy with self-
adaptive mutation mechanism from the open-source Paradiseo frame-
work [165, 166]. This method adjusts in an online manner the stan-
dard deviation of the distribution used to mutate the parameters in the
evolutionary search. For a detailed explanation of this algorithm we
refer the reader to the Paradiseo tutorial on this algorithm [167].

Each evaluated parameter set is simulated with three frequencies $f_i =
1/T_i$, ($\frac{1}{T_1} > \frac{1}{T_2} > \frac{1}{T_3}$) for a fixed intensity S, and the correspond-
ing habituation times (ht_1^f, ht_2^f, ht_3^f) are calculated. Analogously, we
simulate the system for three intensities ($S_1 < S_2 < S_3$) at fixed
frequency, and compute the habituation times (ht_1^S, ht_2^S, ht_3^S).

The cost function that we minimize with the evolutionary algorithm
is given by:

$$\text{Cost function} = \frac{ht_1^f}{ht_2^f} + \frac{ht_2^f}{ht_3^f} + \frac{ht_1^S}{ht_2^S} + \frac{ht_2^S}{ht_3^S} \tag{A.1}$$

If each of the first two terms of eq. (A.1) are less than one, the habit-
uation times are monotonically increasing for decreasing frequencies
($ht_1^f < ht_2^f < ht_3^f$) which is a necessary condition for frequency sen-
sitivity (higher frequency leads to faster habituation, ie smaller ht).
Analogously, intensity sensitivity requires the last two terms of eq.
(A.1) being less than one (higher intensity leads to slower habituation,

ie higher ht). The evolutionary algorithm minimizes the cost function of eq. (A.1), and assigns each parameter set its respective cost value. Only the solutions with a cost function lower than $4 \cdot 0.95 = 3.8$ are analyzed further.

Note that the cutoff does not ensure that the conditions for both frequency and intensity sensitivity are met, since small ratios (< 1) in some of the fractions may compensate larger ratios (> 1) for others. Moreover, frequency sensitivity requires also that recovery is faster with higher frequencies. However, at this step we do not check recovery times because the algorithm to compute the recovery time is quite time-consuming. All this is checked at a final filtering step as explained in the next point.

(iii) Final filtering
Finally, we keep only the $\approx$20 fittest parameter sets resultant from the evolutionary algorithm (the solutions with the 20 lowest cost function values). For each one of them we check if they are frequency and intensity sensitive. A model and its parameter set were considered frequency sensitive if habituation and recovery times were strictly monotonically increasing with the three increasing frequencies for the tested intensity. Analogously, intensity sensitive systems are strictly monotonically increasing in habituation time with increasing intensities for a fixed frequency.

If there is more than one solution meeting the frequency and intensity sensitivity criteria, we chose to show here the one with the lowest cost function value.

A.4 Potentiation of habituation and subliminal accumulation

In order to test our models for the hallmark of potentiation of habituation, we first choose a frequency and intensity and simulate the system to calculate habituation (ht) and recovery time (rt). We then i) simulate the system starting from the standard initial condition until it habituates, ii) starting from the habituated state, we let the system recover ($S = 0$) for a fraction $f \in (0, 1)$ of the recovery time, and iii) starting from the partially recovered state, we execute the habituation protocol again, yielding a new habituation time (ht'). We consider $ht' < ht$ as potentiation of habituation.

In order to test for the hallmark of subliminal accumulation, we first calculate habituation and recovery in the standard way, considering that habitu-

ation is reached when the relative peak difference is less than 0.01, which gives a given ht and rt. We simulate again for the same conditions, but considering a smaller threshold (0.005) to define habituation. Effectively, this means that the system is simulated beyond ht for a few more peaks. We then calculate recovery from this state (rt'). We consider that the criterion for subliminal accumulation is fulfilled if $rt' > rt$.

A.5 Sensitivity analysis

A.5.1 Perturbation analysis

In nature, parameters such as catalytic rate constants and Michaelis-Menten constants are often subject to fluctuations due to changes in temperature, intracellular pH, or conformational changes and mutations of the corresponding enzymes. Maintaining unrestricted functionality under different conditions requires that the general behavior of cells must be unaffected by these parameter fluctuations.

We performed a sensitivity analysis in order to test how much the parameters of the model in question can be changed without losing frequency and intensity sensitivity (since we found that if these hallmarks are fulfilled, the others as well). Each parameter was individually multiplied by a perturbation factor (between 0.1 and 10.0) and the new system was tested for frequency and intensity sensitivity.

To test frequency sensitivity we used the same frequencies and intensity as in the parameter search of Section A.3. The new parameter set (with a single perturbed parameter) was simulated with three frequencies $f_i = 1/T_i$, ($\frac{1}{T_1} > \frac{1}{T_2} > \frac{1}{T_3}$) for a fixed intensity S, and the corresponding habituation times (ht_1^f, ht_2^f, ht_3^f) and recovery times (rt_1^f, rt_2^f, rt_3^f) are calculated. If $\frac{ht_1^f}{ht_2^f} < thr$, $\frac{ht_2^f}{ht_3^f} < thr$, and $\frac{rt_1^f}{rt_2^f} < thr$, $\frac{rt_2^f}{rt_3^f} < thr$, the system is considered to be frequency sensitive. The threshold (thr) in all cases was chosen as 0.95 for all the models, except for the recovery times in the concatenated NF model, where $thr = 0.97$.

Analogously, we simulate the system with the perturbed parameter for three intensities ($S_1 < S_2 < S_3$) at fixed frequency, and compute the habituation times (ht_1^S, ht_2^S, ht_3^S). If $\frac{ht_1^S}{ht_2^S} < thr$ and $\frac{ht_2^S}{ht_3^S} < thr$, the system is considered to be intensity sensitive. For all the models we chose $thr = 0.95$.

The maximal perturbations which did not affect these hallmarks are displayed on a $\log_{10}$ scale in Fig. 2.13 for the concantenated IFF model, Fig. 2.14 for the concantenated NF model, Fig. 2.15 for the receptor + IFF model, and

Fig. 2.16 for the receptor + NF cascade model.

A.5.2   Check for intermediate frequencies and intensities

We also performed some extra check-ups for the parameter set found for
each model. For frequency sensitivity, we tested if habituation and recov-
ery times were strictly monotonically increasing for intermediate frequen-
cies between the three chosen increasing ones ($\frac{1}{T_3} < \frac{1}{T_2} < \frac{1}{T_1}$). We only
checked for all intermediate integer values of frequencies. All the studied
models passed this test.

Analogously, for intensity sensitivity, we tested if habituation times were
strictly monotonically increasing for all the intermediate integer values of
intensities between the three chosen increasing ones ($S_1 < S_2 < S_3$). All
the studied models passed this test.

A.5.3   Check for habituation's threshold

We also explored whether frequency and intensity sensitivity are preserved
for the parameter set of each model when we modify the threshold between
two neighboring peaks to define when a system has habituated (see Section
2.2.1). For each model we lowered this threshold (starting from the one we
used: 0.01) and tested if the system still is frequency or intensity sensitive.
The minimum threshold which did not affect frequency or intensity sensi-
tivity is shown in Table A.1 for each model. In this case we applied a more
permissive definition of frequency or intensity sensitivity by choosing the
threshold defined in Section A.5.1 as $\mathrm{thr} = 1.0$.

Model	Min. habituation threshold	
	Freq. sens.	Inten. sens.
Concatenated IFF	0.006	0.002
Concatenated NF	0.005	0.002
Receptor + IFF	0.007	0.004
Receptor + NF cascade	0.008	0.006

Table A.1: **Robustness of habituation threshold.** Minimum threshold values for
the definition of habituation time that maintain frequency or intensity sensitivity.

A.6   Parameter values for each model

Parameter	Search range	Best solution
k_{Ia1}	[0.01; 0.25]	0.023
k_{Ii1}	[30.0; 50.0]	34.44
k_{Ma1}	[8.0; 20.0]	17.71
k_{Mi1}	[0.01; 0.1]	0.0382
k_{Ra1}	[57.0; 80.0]	57.92
k_{Ri1}	[1.00; 2.10]	1.39
K_1	[0.00025; 0.002]	0.000534
k_{Ia2}	[0.012; 0.12]	0.0160
k_{Ii2}	[0.873; 20.0]	14.3
k_{Ma2}	[2.52; 20.0]	4.34
k_{Mi2}	[0.001; 0.01]	0.00147
k_{Ra2}	[1.976; 49.7]	26.2
k_{Ri2}	[12.77; 49.7]	45.99
K_2	[0.75; 2.0]	0.791

Table A.2: **Parameter values of the concatenated IFF model.** For frequency sensitivity the periods tested were: $T = 15, 20, 25$ with stimulus intensity $S = 10$. For intensity sensitivity the intensities tested were: $S = 10, 20, 30$ with period $T = 15$. In all cases $T_{on} = 1.11$.

Parameter	Search range	Best solution
k_{Ia1}	[0.0225; 0.0235]	0.023
k_{Ii1}	[30.0; 50.0]	33.97
k_{Ma1}	[0.04; 0.076]	0.049
k_{Mi1}	[0.02; 0.046]	0.0211
k_{Ra1}	[5.80; 15.90]	7.74
k_{Ri1}	[15.40; 35.50]	18.19
K_1	[0.00025; 0.002]	0.000691
k_{Ia2}	[0.03; 0.06]	0.0373
k_{Ii2}	[14.0; 37.0]	15.94
k_{Ma2}	[0.5; 2.03]	1.026
k_{Mi2}	[0.00014; 0.0018]	0.000423
k_{Ra2}	[4.71; 18.8]	7.51
k_{Ri2}	[12.77; 49.7]	22.39
K_2	[0.5; 1.58]	1.147

Table A.3: **Parameter values of the concatenated NF model.** For frequency sensitivity the periods tested were: $T = 5, 10, 15$ with stimulus intensity $S = 15$. For intensity sensitivity the intensities tested were: $S = 10, 15, 20$ with period $T = 10$. In all cases $T_{on} = 1.11$.

Parameter	Search range	Best solution
k_{Ia1}	[0.15; 0.25]	0.214
k_{Ii1}	[6.0; 9.0]	6.85
k_{Ma1}	[0.001; 0.01]	0.00995
k_{Mi1}	[0.01; 0.1]	0.0249
k_{Ra1}	[0.01; 0.1]	0.0118
k_{Ri1}	[0.01; 0.6]	0.30
K_1	[0.0001; 0.001]	0.000279

Table A.4: **Parameter values of the single IFF model.** For intensity sensitivity the intensities tested were: $S = 4.5, 9.0, 13.5$ with period $T = 5$. In all cases $T_{on} = 0.5$.

Parameter	Search range	Best solution
k_{Ia1}	[0.15; 0.25]	0.15
k_{Ii1}	[6.0; 9.0]	6.85
k_{Ma1}	[0.1; 1.0]	0.214
k_{Mi1}	[0.01; 0.1]	0.0249
k_{Ra1}	[0.01; 0.1]	0.0236
k_{Ri1}	[5.0; 10.0]	9.00
K_1	[0.0001; 0.001]	0.00279

Table A.5: **Parameter values of the single NF model.** For intensity sensitivity the intensities tested were: $S = 2.0, 4.5, 9.0$ with period $T = 5$. In all cases $T_{on} = 0.5$.

Parameter	Search range	Best solution
k_a	[0.1; 5.0]	1.497
k_r	[0.001; 0.01]	0.00830
k_i	[0.01; 1.0]	0.1255
k_{Ia2}	[0.012; 0.12]	0.01519
k_{Ii2}	[0.1; 20.0]	11.20
k_{Ma2}	[2.52; 20.0]	7.65
k_{Mi2}	[0.0001; 0.01]	0.00079
k_{Ra2}	[1.976; 49.7]	25.96
k_{Ri2}	[12.77; 49.7]	36.52

Table A.6: **Parameter values of the receptor + IFF model.** For frequency sensitivity the periods tested were: $T = 10, 15, 25$ with stimulus intensity $S = 5$. For intensity sensitivity the intensities tested were: $S = 2, 5, 15$ with period $T = 25$. In all cases $T_{on} = 1.0$.

Parameter	Search range	Best solution
k_a	[0.1; 5.0]	0.773
k_r	[0.01; 0.5]	0.1046
k_i	[0.01; 1.0]	0.1236
k_{FB}	[0.01; 1.0]	0.9039
k_{a1}	[0.012; 1.5]	1.033
k_{i1}	[0.1; 20.0]	5.046
k_{a2}	[0.1; 2.0]	1.002
k_{i2}	[0.1; 10.0]	5.757
k_{a3}	[1.0; 5.0]	2.52
k_{i3}	[0.0001; 0.001]	0.000594

Table A.7: **Parameter values of the receptor + NF cascade model.** For frequency sensitivity the periods tested were: $T = 5, 10, 15$ with stimulus intensity $S = 10$. For intensity sensitivity the intensities tested were: $S = 3, 5, 10$ with period $T = 10$. In all cases $T_{on} = 1.0$.

Appendix B.   Computation of Lyapunov exponents

To ascertain whether a dynamical system exhibits ordered or chaotic dynamics, a common approach involves examining the average sensitivity to perturbations in its initial conditions [112, 114]. The underlying logic is that small differences in the initial conditions of two otherwise identical systems should eventually diminish if the system is in the ordered phase, or persist (and amplify) if it is in the chaotic phase. The Lyapunov (characteristic) exponent (LE) serves as a measure for the exponential divergence of two trajectories in the state space of a dynamical system with very small initial separation. Although a spectrum of Lyapunov exponents is defined, the rate of divergence is predominantly influenced by the largest exponent. It is defined as:

$$\lambda = \lim_{k \to \infty} \frac{1}{k} \ln \left(\frac{\gamma_k}{\gamma_0} \right), \tag{B.1}$$

with γ_0 being the initial distance between the perturbed and the unperturbed trajectory, and γ_k being the distance at time k. Thus, super-critical or chaotic dynamics is typically associated with a positive MLE ($\lambda > 0$), while for sub-critical systems (ordered phase) $\lambda < 0$. A phase transition thus occurs at $\lambda \approx 0$ (called the critical point, or *edge of chaos*).

Since, this is an asymptotic quantity, it has to be estimated for most dynamical systems. We employ the approach outlined in ref. [168] (Chap. 5.6). Two identical networks are simulated for a duration of 1,000 steps (although longer durations were experimented with, they were determined to have an insignificant impact). Following this initial period designed to eliminate transient random initialization effects, the procedure is as follows:

1. Introduce a minor perturbation into a unit n of one network, while leaving the other network unperturbed. This results in a separation between the state of the perturbed network ($\mathbf{x^2}$) and the state of the unperturbed network ($\mathbf{x^1}$) by an amount represented by γ_0. This initial separation has to be chosen carefully. It should be as small as possible, but still large enough so that its influence will be measurable with limited numerical precision on a computer. We found 10^{-2}

to be a robust value in our simulations.

2. Advance the simulation one step and record the resulting state difference for this kth step $\gamma_k = \left\| \mathbf{x^1}(k) - \mathbf{x^2}(k) \right\|$. The norm $\|\cdot\|$ denotes the Euclidean norm in our case, but can be chosen differently.

3. Reset the state of the perturbed network $\mathbf{x^2}$ to $\mathbf{x^1}(k) + (\gamma_0/\gamma_k)(\mathbf{x^2}(k) - \mathbf{x^1}(k))$. This renormalization step keeps the two trajectories close to avoid numerical overflows.

We repeat these simulation and renormalization steps for a total of 1,000 times (again, longer durations were tested, but found not to change results significantly), and then average the logarithm of the distances along the trajectory as $\lambda_n = \left\langle \ln(\frac{\gamma_k}{\gamma_0}) \right\rangle_k$.

For a reservoir with N units that is tested, we calculate N different λ_n values, choosing a different reservoir unit n to be perturbed each time. These values are then averaged to yield a final estimate of the Lyapunov exponent $\lambda = \langle \lambda_n \rangle_n$.

Appendix C.   Contributions

C.1   Publications

1 **Maria Sol Vidal-Saez**, Oscar Vilarroya and Jordi Garcia-Ojalvo, "A multiscale sensorimotor model of experience-dependent behavior in a minimal organism". Submitted to Biochemical and Biophysical Research Communications, Feb. 2024. Available on arXiv: `https://arxiv.org/abs/2402.05251`.

2 Lina Eckert[*], **Maria Sol Vidal-Saez**[*], Ziyuan Zhao[*,1], Jordi Garcia-Ojalvo, Rosa Martinez-Corral and Jeremy Gunawardena, "Learning in Single Cells: Molecular Models of Habituation". To be submitted, 2024.

3 **Maria Sol Vidal-Saez**, Oscar Vilarroya and Jordi Garcia-Ojalvo, "Biological computation through recurrence". Submitted to Biochemical and Biophysical Research Communications, Feb. 2024. Available on arXiv: `https://arxiv.org/abs/2402.05243`.

4 **Maria Sol Vidal-Saez** and Jordi Garcia-Ojalvo, "Memory encoding in gene regulatory networks: local topology and dynamics approach". In preparation.

C.2   Software

1 Github repository associated with publication [1]. https://github.com/dsb-lab/experience_dependent_c_elegans.

2 Github repository associated with publication [4]. https://github.com/dsb-lab/memory-encoding-GRN.

---

[1]* These authors contributed equally to the publication.

C.3 Communications in conferences

1 **Maria Sol Vidal-Saez**, Oscar Vilarroya and Jordi Garcia-Ojalvo, "State and context-dependent decision making in *C. elegans*". Poster presentation at Barcelona Computational, Cognitive and Systems Neuroscience (BARCCSYN) meeting, Barcelona, Spain (2022).

2 **Maria Sol Vidal-Saez**, Oscar Vilarroya and Jordi Garcia-Ojalvo, "Context-dependent decision making in *C. elegans*". Poster presentation at The Future of the Physics of Life, AMOLF, Amsterdam, Netherlands (2022).

3 **Maria Sol Vidal-Saez**, Lina Eckert, Ziyuan Zhao, Jeremy Gunawardena, Rosa Martinez-Corral and Jordi Garcia-Ojalvo, "Hallmarks of habituation: a biochemically-plausible model". Poster presentation at Symposium of the Barcelona Collaboratorium. Intelligence: natural, artificial and synthetic, Barcelona, Spain (2023).

4 **Maria Sol Vidal-Saez**, Lina Eckert, Ziyuan Zhao, Jeremy Gunawardena, Rosa Martinez-Corral and Jordi Garcia-Ojalvo, "Hallmarks of habituation: a biochemically-plausible model". Poster presentation at XXIV Congreso de Física Estadística (FisEs'23), Pamplona, Spain (2023).

5 **Maria Sol Vidal-Saez** and Jordi Garcia-Ojalvo, "Temporal information-processing and memory in gene regulatory networks". Poster presentation at Workshop on Transport Phenomena and Fluctuations in Small Complex Systems, Buenos Aires, Argentina (2023).

Bibliography

[1] A. B. Barron, E. A. Hebets, T. A. Cleland, C. L. Fitzpatrick, M. E. Hauber, and J. R. Stevens, "Embracing multiple definitions of learning," *Trends in Neurosciences*, vol. 38, no. 7, pp. 405–407, Jul. 2015. [Online]. Available: https://doi.org/10.1016/j.tins.2015.04.008

[2] C. H. Rankin, T. Abrams, R. J. Barry, S. Bhatnagar, D. F. Clayton, J. Colombo, G. Coppola, M. A. Geyer, D. L. Glanzman, S. Marsland, F. K. McSweeney, D. A. Wilson, C.-F. Wu, and R. F. Thompson, "Habituation revisited: An updated and revised description of the behavioral characteristics of habituation," *Neurobiology of Learning and Memory*, vol. 92, no. 2, pp. 135–138, 2009. [Online]. Available: https://doi.org/10.1016/j.nlm.2008.09.012

[3] R. F. Thompson and W. A. Spencer, "Habituation: A model phenomenon for the study of neuronal substrates of behavior," *Psychological Review*, vol. 73, no. 1, pp. 16–43, 1966. [Online]. Available: https://doi.org/10.1037/h0022681

[4] J. E. R. Staddon, "On rate-sensitive habituation," *Adaptive Behavior*, vol. 1, no. 4, pp. 421–436, 1993. [Online]. Available: https://doi.org/10.1177/105971239300100402

[5] B. E. Adelman, "On the conditioning of plants: A review of experimental evidence," *Perspectives on Behavior Science*, vol. 41, no. 2, pp. 431–446, 2018. [Online]. Available: https://doi.org/10.1007/s40614-018-0173-6

[6] M. Gagliano, V. V. Vyazovskiy, A. A. Borbély, M. Grimonprez, and M. Depczynski, "Learning by association in plants," *Scientific Reports*, vol. 6, no. 1, p. 38427, 2016. [Online]. Available: https://doi.org/10.1038/srep38427

[7] P. B. Applewhite, "Behavioral plasticity in the sensitive plant, Mimosa," *Behavioral Biology*, vol. 7, no. 1, pp. 47–53, 1972. [Online]. Available: https://doi.org/10.1016/S0091-6773(72)80187-1

[8] M. Gagliano, C. I. Abramson, and M. Depczynski, "Plants learn and remember: lets get used to it," *Oecologia*, vol. 186, no. 1, pp. 29–31, 2018. [Online]. Available: https://doi.org/10.1007/s00442-017-4029-7

[9] D. L. Glanzman, "Habituation in Aplysia: The Cheshire Cat of neurobiology," *Neurobiology of Learning and Memory*, vol. 92, no. 2, pp. 147–154, 2009. [Online]. Available: https://doi.org/10.1016/j.nlm.2009.03.005

[10] E.-L. Yap and M. E. Greenberg, "Activity-regulated transcription: Bridging the gap between neural activity and behavior," *Neuron*, vol. 100, no. 2, pp. 330–348, 2018. [Online]. Available: https://doi.org/10.1016/j.neuron.2018.10.013

[11] V. F. Castellucci and E. R. Kandel, "A quantal analysis of the synaptic depression underlying habituation of the gill-withdrawal reflex in aplysia," *Proceedings of the National Academy of Sciences*, vol. 71, no. 12, pp. 5004–5008, 1974. [Online]. Available: https://doi.org/10.1073/pnas.71.12.5004

[12] R. S. Zucker, "Crayfish escape behavior and central synapses. ii. physiological mechanisms underlying behavioral habituation." *Journal of neurophysiology*, vol. 35, no. 5, pp. 621–637, 1972. [Online]. Available: https://doi.org/10.1152/jn.1972.35.5.621

[13] P. B. Farel, "Dual processes control response habituation across a single synapse," *Brain Research*, vol. 72, no. 2, pp. 323–327, 1974. [Online]. Available: https://doi.org/10.1016/0006-8993(74)90874-9

[14] S. K. Tang and W. F. Marshall, "Cell learning," *Current Biology*, vol. 28, no. 20, pp. R1180–R1184, 2018. [Online]. Available: https://doi.org/10.1016/j.cub.2018.09.015

[15] B. Gelber, "Investigations of the behavior of paramecium aurelia: I. modification of behavior after training with reinforcement," *Journal of Comparative and Physiological Psychology*, vol. 45, no. 1, pp. 58–65, 1952. [Online]. Available: https://doi.org/10.1037/h0063093

[16] T. M. Hennessey, W. B. Rucker, and C. G. McDiarmid, "Classical conditioning in paramecia," *Animal Learning & Behavior*, vol. 7, no. 4, pp. 417–423, 1979. [Online]. Available: https://doi.org/10.3758/BF03209695

[17] S. J. Gershman, P. E. Balbi, C. R. Gallistel, and J. Gunawardena, "Reconsidering the evidence for learning in single cells," *eLife*,

vol. 10, pp. 1–15, 2021. [Online]. Available: https://doi.org/10.7554/eLife.61907

[18] J. Gunawardena, "Learning outside the brain: Integrating cognitive science and systems biology," *Proceedings of the IEEE*, vol. 110, no. 5, pp. 590–612, 2022. [Online]. Available: https://doi.org/10.1109/JPROC.2022.3162791

[19] I. M. De la Fuente, C. Bringas, I. Malaina, M. Fedetz, J. Carrasco-Pujante, M. Morales, S. Knafo, L. Martínez, A. Pérez-Samartín, J. López, G. Pérez-Yarza, and M. D. Boyano, "Evidence of conditioned behavior in amoebae," *Nature Communications*, vol. 10, no. 1, p. 3690, 2019. [Online]. Available: https://doi.org/10.1038/s41467-019-11677-w

[20] H. S. Jennings, *Behavior of the Lower Organisms.* New York, NY, USA: Columbia Univ. Press, 1906. [Online]. Available: https://doi.org/10.1037/10817-000

[21] J. P. Dexter, S. Prabakaran, and J. Gunawardena, "A complex hierarchy of avoidance behaviors in a single-cell eukaryote," *Current Biology*, vol. 29, no. 24, pp. 4323–4329, 2019. [Online]. Available: https://doi.org/10.1016/j.cub.2019.10.059

[22] D. C. Wood, "Electrophysiological correlates of the response decrement produced by mechanical stimuli in the protozoan, stentor coeruleus," *Journal of Neurobiology*, vol. 2, no. 1, pp. 1–11, 1970. [Online]. Available: https://doi.org/10.1002/neu.480020102

[23] ——, "Parametric studies of the response decrement produced by mechanical stimuli in the protozoan stentor coeruleus," *Journal of Neurobiology*, vol. 1, no. 3, pp. 345–360, 1970. [Online]. Available: https://doi.org/10.1002/neu.480010309

[24] R. P. Boisseau, D. Vogel, and A. Dussutour, "Habituation in non-neural organisms: Evidence from slime moulds," *Proceedings of the Royal Society B: Biological Sciences*, vol. 283, no. 1829, pp. 2–8, 2016. [Online]. Available: https://doi.org/10.1098/rspb.2016.0446

[25] M. Bonzanni, N. Rouleau, M. Levin, and D. L. Kaplan, "Optogenetically induced cellular habituation in non-neuronal cells," *PLOS ONE*, vol. 15, no. 1, pp. 1–14, 01 2020. [Online]. Available: https://doi.org/10.1371/journal.pone.0227230

[26] P. N. McFadden and D. E. Koshland, "Habituation in the single cell: diminished secretion of norepinephrine with repetitive

depolarization of pc12 cells," *Proceedings of the National Academy of Sciences*, vol. 87, no. 5, pp. 2031–2035, 1990. [Online]. Available: https://doi.org/10.1073/pnas.87.5.2031

[27] L. Cheever and D. Koshland, "Habituation of neurosecretory responses to extracellular atp in pc12 cells," *Journal of Neuroscience*, vol. 14, no. 8, pp. 4831–4838, 1994. [Online]. Available: https://doi.org/10.1523/JNEUROSCI.14-08-04831.1994

[28] P. N. McFadden and D. E. Koshland, "Parallel pathways for habituation in repetitively stimulated pc12 cells," *Neuron*, vol. 4, no. 4, pp. 615–621, 1990. [Online]. Available: https://doi.org/10.1016/0896-6273(90)90119-Z

[29] L. Cheever and D. E. Koshland, "Retention of habituation in pc12 cells," *Proceedings of the National Academy of Sciences*, vol. 89, no. 21, pp. 10 084–10 088, 1992. [Online]. Available: https://doi.org/10.1073/pnas.89.21.10084

[30] B. H. Morimoto and D. E. Koshland, "Short-term and long-term memory in single cells," *The FASEB Journal*, vol. 5, no. 7, pp. 2061–2067, 1991. [Online]. Available: https://doi.org/10.1096/fasebj.5.7.2010059

[31] P. T. Martin and D. E. Koshland, "Neurosecretory habituation in pc12 cells: modulation during parallel habituation." *Proceedings of the National Academy of Sciences*, vol. 92, no. 11, pp. 5052–5056, 1995. [Online]. Available: https://doi.org/10.1073/pnas.92.11.5052

[32] ——, "The biochemistry of the neuron. neurosecretory habituation to repetitive depolarizations in pc12 cells." *Journal of Biological Chemistry*, vol. 266, no. 12, pp. 7388–7392, 1991. [Online]. Available: https://doi.org/10.1016/S0021-9258(20)89459-9

[33] U. Alon, *An Introduction to Systems Biology: Design Principles of Biological Circuits*.   CRC Press, Jul. 2019. [Online]. Available: https://doi.org/10.1201/9780429283321

[34] J. E. Ferrell, "Perfect and near-perfect adaptation in cell signaling," *Cell Systems*, vol. 2, no. 2, p. 62–67, Feb. 2016. [Online]. Available: http://dx.doi.org/10.1016/j.cels.2016.02.006

[35] M. H. Khammash, "Perfect adaptation in biology," *Cell Systems*, vol. 12, no. 6, p. 509–521, Jun. 2021. [Online]. Available: http://dx.doi.org/10.1016/j.cels.2021.05.020

[36] W. Ma, A. Trusina, H. El-Samad, W. A. Lim, and C. Tang, "Defining network topologies that can achieve biochemical adaptation," *Cell*, vol. 138, no. 4, p. 760–773, Aug. 2009. [Online]. Available: http://dx.doi.org/10.1016/j.cell.2009.06.013

[37] W. Shi, W. Ma, L. Xiong, M. Zhang, and C. Tang, "Adaptation with transcriptional regulation," *Scientific Reports*, vol. 7, no. 1, feb 2017. [Online]. Available: http://dx.doi.org/10.1038/srep42648

[38] T.-M. Yi, Y. Huang, M. I. Simon, and J. Doyle, "Robust perfect adaptation in bacterial chemotaxis through integral feedback control," *Proceedings of the National Academy of Sciences*, vol. 97, no. 9, p. 4649–4653, apr 2000. [Online]. Available: http://dx.doi.org/10.1073/pnas.97.9.4649

[39] U. S. Bhalla and R. Iyengar, "Emergent Properties of Networks of Biological Signaling Pathways," *Science*, vol. 283, no. 5400, pp. 381–387, Jan. 1999. [Online]. Available: https://doi.org/10.1126/science.283.5400.381

[40] T. Helikar, J. Konvalina, J. Heidel, and J. A. Rogers, "Emergent decision-making in biological signal transduction networks," *Proceedings of the National Academy of Sciences*, vol. 105, no. 6, pp. 1913–1918, Feb. 2008. [Online]. Available: https://doi.org/10.1073/pnas.0705088105

[41] J. S. Mattick, "Non-coding RNAs: the architects of eukaryotic complexity," *EMBO reports*, vol. 2, no. 11, pp. 986–991, Nov. 2001. [Online]. Available: https://doi.org/10.1093/embo-reports/kve230

[42] J. Stelling, S. Klamt, K. Bettenbrock, S. Schuster, and E. D. Gilles, "Metabolic network structure determines key aspects of functionality and regulation," *Nature*, vol. 420, no. 6912, pp. 190–193, Nov. 2002. [Online]. Available: https://doi.org/10.1038/nature01166

[43] D. R. Chialvo, "Emergent complex neural dynamics," *Nature Physics*, vol. 6, no. 10, pp. 744–750, Oct. 2010. [Online]. Available: https://doi.org/10.1038/nphys1803

[44] W. Maass, T. Natschläger, and H. Markram, "Real-Time Computing Without Stable States: A New Framework for Neural Computation Based on Perturbations," *Neural Computation*, vol. 14, no. 11, pp. 2531–2560, Nov. 2002. [Online]. Available: https://doi.org/10.1162/089976602760407955

[45] H. Jaeger, *Short term memory in echo state networks*. GMD Forschungszentrum Informationstechnik, 2001. [Online]. Available: https://doi.org/10.24406/publica-fhg-291107

[46] D. Rumelhart, G. Hinton, and R. Williams, "Learning internal representations by error propagation," in *Readings in Cognitive Science*. Elsevier, 1988, pp. 399–421. [Online]. Available: https://doi.org/10.1016/b978-1-4832-1446-7.50035-2

[47] D. V. Buonomano and W. Maass, "State-dependent computations: spatiotemporal processing in cortical networks," *Nature Reviews Neuroscience*, vol. 10, no. 2, pp. 113–125, Feb. 2009. [Online]. Available: https://doi.org/10.1038/nrn2558

[48] M. Lukoševičius and H. Jaeger, "Reservoir computing approaches to recurrent neural network training," *Computer Science Review*, vol. 3, no. 3, pp. 127–149, Aug. 2009. [Online]. Available: https://doi.org/10.1016/j.cosrev.2009.03.005

[49] D. Verstraeten, B. Schrauwen, M. D'Haene, and D. Stroobandt, "An experimental unification of reservoir computing methods," *Neural Networks*, vol. 20, no. 3, pp. 391–403, Apr. 2007. [Online]. Available: https://doi.org/10.1016/j.neunet.2007.04.003

[50] P. Werbos, "Backpropagation through time: what it does and how to do it," *Proceedings of the IEEE*, vol. 78, no. 10, pp. 1550–1560, 1990. [Online]. Available: https://doi.org/10.1109/5.58337

[51] R. J. Williams and D. Zipser, "A learning algorithm for continually running fully recurrent neural networks," *Neural Computation*, vol. 1, no. 2, pp. 270–280, 1989. [Online]. Available: https://doi.org/10.1162/neco.1989.1.2.270

[52] K. Doya, "Bifurcations in the learning of recurrent neural networks," *IEEE International Symposium on Circuits and Systems*, vol. 6, pp. 2777–2780, 1992. [Online]. Available: https://doi.org/10.1109/ISCAS.1992.230622

[53] H. Jaeger, M. Lukoševičius, D. Popovici, and U. Siewert, "Optimization and applications of echo state networks with leaky-integrator neurons," *Neural Networks*, vol. 20, no. 3, pp. 335–352, Apr. 2007. [Online]. Available: https://doi.org/10.1016/j.neunet.2007.04.016

[54] J. N. T. John Graham White, Eileen Southgate and S. Brenner, "The structure of the nervous system of the nematode caenorhabditis

elegans," *Philosophical Transactions of the Royal Society of London. B, Biological Sciences*, vol. 314, no. 1165, p. 1–340, Nov. 1986. [Online]. Available: http://dx.doi.org/10.1098/rstb.1986.0056

[55] T. C. elegans Sequencing Consortium, "Genome sequence of the nematode c. elegans: A platform for investigating biology," *Science*, vol. 282, no. 5396, p. 2012–2018, 1998. [Online]. Available: http://dx.doi.org/10.1126/science.282.5396.2012

[56] J. E. Sulston, E. Schierenberg, J. G. White, and J. N. Thomson, "The embryonic cell lineage of the nematode Caenorhabditis elegans," *Developmental Biology*, vol. 100, no. 1, pp. 64–119, Nov. 1983. [Online]. Available: https://doi.org/10.1016/0012-1606(83)90201-4

[57] H. A. Colbert and C. I. Bargmann, "Odorant-specific adaptation pathways generate olfactory plasticity in c. elegans," *Neuron*, vol. 14, no. 4, pp. 803–812, 1995. [Online]. Available: https://doi.org/10.1016/0896-6273(95)90224-4

[58] S. Saeki, M. Yamamoto, and Y. Iino, "Plasticity of chemotaxis revealed by paired presentation of a chemoattractant and starvation in the nematode caenorhabditis elegans," *Journal of Experimental Biology*, vol. 204, no. 10, pp. 1757–1764, 2001. [Online]. Available: https://doi.org/10.1242/jeb.204.10.1757

[59] I. Mori and Y. Ohshima, "Neural regulation of thermotaxis in caenorhabditis elegans," *Nature*, vol. 376, no. 6538, pp. 344–348, 1995. [Online]. Available: https://doi.org/10.1038/376344a0

[60] S. Ward, "Chemotaxis by the nematode caenorhabditis elegans: identification of attractants and analysis of the response by use of mutants," *Proceedings of the National Academy of Sciences*, vol. 70, no. 3, pp. 817–821, 1973. [Online]. Available: https://doi.org/10.1073/pnas.70.3.817

[61] R. K. Hukema, S. Rademakers, M. P. Dekkers, J. Burghoorn, and G. Jansen, "Antagonistic sensory cues generate gustatory plasticity in Caenorhabditis elegans," *The EMBO Journal*, vol. 25, no. 2, pp. 312–322, Jan. 2006. [Online]. Available: https://doi.org/10.1038/sj.emboj.7600940

[62] R. K. Hukema, S. Rademakers, and G. Jansen, "Gustatory plasticity in C. elegans involves integration of negative cues and NaCl taste mediated by serotonin, dopamine, and glutamate," *Learning & Memory*, vol. 15, no. 11, pp. 829–836, Jan. 2008. [Online]. Available: https://doi.org/10.1101/lm.994408

[63] G. Jansen, D. Weinkove, and R. H. Plasterk, "The G-protein gamma subunit gpc-1 of the nematode *C. elegans* is involved in taste adaptation," *The EMBO Journal*, vol. 21, no. 5, pp. 986–994, Mar. 2002. [Online]. Available: https://doi.org/10.1093/emboj/21.5.986

[64] M. Tomioka, T. Adachi, H. Suzuki, H. Kunitomo, W. R. Schafer, and Y. Iino, "The insulin/pi 3-kinase pathway regulates salt chemotaxis learning in caenorhabditis elegans," *Neuron*, vol. 51, no. 5, pp. 613–625, 2006. [Online]. Available: https://doi.org/10.1016/j.neuron.2006.07.024

[65] H. Kunitomo, H. Sato, R. Iwata, Y. Satoh, H. Ohno, K. Yamada, and Y. Iino, "Concentration memory-dependent synaptic plasticity of a taste circuit regulates salt concentration chemotaxis in caenorhabditis elegans," *Nature communications*, vol. 4, no. 1, pp. 1–11, 2013. [Online]. Available: https://doi.org/10.1038/ncomms3210

[66] S. Kato, Y. Xu, C. E. Cho, L. Abbott, and C. I. Bargmann, "Temporal responses of c. elegans chemosensory neurons are preserved in behavioral dynamics," *Neuron*, vol. 81, no. 3, p. 616–628, Feb. 2014. [Online]. Available: http://dx.doi.org/10.1016/j.neuron.2013.11.020

[67] E. Niebur and P. Erdös, "Theory of the locomotion of nematodes," *Biophysical Journal*, vol. 60, no. 5, p. 1132–1146, Nov. 1991. [Online]. Available: http://dx.doi.org/10.1016/S0006-3495(91)82149-X

[68] G. J. Stephens, B. Johnson-Kerner, W. Bialek, and W. S. Ryu, "Dimensionality and dynamics in the behavior of c. elegans," *PLoS Computational Biology*, vol. 4, no. 4, p. e1000028, Apr. 2008. [Online]. Available: http://dx.doi.org/10.1371/journal.pcbi.1000028

[69] M. Xu, T. A. Jarrell, Y. Wang, S. J. Cook, D. H. Hall, and S. W. Emmons, "Computer Assisted Assembly of Connectomes from Electron Micrographs: Application to Caenorhabditis elegans," *PLOS ONE*, vol. 8, no. 1, p. e54050, Jan. 2013. [Online]. Available: https://doi.org/10.1371/journal.pone.0054050

[70] B. Szigeti, P. Gleeson, M. Vella, S. Khayrulin, A. Palyanov, J. Hokanson, M. Currie, M. Cantarelli, G. Idili, and S. Larson, "OpenWorm: an open-science approach to modeling Caenorhabditis elegans," *Frontiers in Computational Neuroscience*, vol. 8, 2014. [Online]. Available: http://dx.doi.org/10.3389/fncom.2014.00137

[71] P. A. Appleby, "A model of chemotaxis and associative learning in c. elegans," *Biological Cybernetics*, vol. 106, no. 6–7, p.

373–387, Jul. 2012. [Online]. Available: http://dx.doi.org/10.1007/s00422-012-0504-8

[72] T. C. Ferrée and S. R. Lockery, "Computational rules for chemotaxis in the nematode *C. elegans*," *Journal of Computational Neuroscience*, vol. 6, no. 3, p. 263–277, 1999. [Online]. Available: http://dx.doi.org/10.1023/a:1008857906763

[73] E. J. Izquierdo and S. R. Lockery, "Evolution and analysis of minimal neural circuits for klinotaxis in caenorhabditis elegans," *Journal of Neuroscience*, vol. 30, no. 39, pp. 12 908–12 917, 2010. [Online]. Available: https://doi.org/10.1523/JNEUROSCI.2606-10.2010

[74] E. J. Izquierdo and R. D. Beer, "Connecting a connectome to behavior: an ensemble of neuroanatomical models of c. elegans klinotaxis," *PLoS computational biology*, vol. 9, no. 2, p. e1002890, 2013. [Online]. Available: https://doi.org/10.1371/journal.pcbi.1002890

[75] N. A. Dunn, S. R. Lockery, J. T. Pierce-Shimomura, and J. S. Conery, "A neural network model of chemotaxis predicts functions of synaptic connections in the nematode caenorhabditis elegans," *Journal of Computational Neuroscience*, vol. 17, no. 2, p. 137–147, Sep. 2004. [Online]. Available: https://doi.org/10.1023/b:jcns.0000037679.42570.d5

[76] N. Dunn, J. Pierce-Shimomura, J. Conery, and S. Lockery, "Clustered neural dynamics identify motifs for chemotaxis in caenorhabditis elegans," in *The 2006 IEEE International Joint Conference on Neural Network Proceedings*. IEEE, 2006. [Online]. Available: http://dx.doi.org/10.1109/IJCNN.2006.246730

[77] R. E. Brown and P. M. Milner, "The legacy of Donald O. Hebb: more than the Hebb Synapse," *Nature Reviews Neuroscience*, vol. 4, no. 12, pp. 1013–1019, Dec. 2003. [Online]. Available: https://doi.org/10.1038/nrn1257

[78] N. Caporale and Y. Dan, "Spike Timing–Dependent Plasticity: A Hebbian Learning Rule," *Annual Review of Neuroscience*, vol. 31, no. 1, pp. 25–46, 2008. [Online]. Available: https://doi.org/10.1146/annurev.neuro.31.060407.125639

[79] T. Takeuchi, A. J. Duszkiewicz, and R. G. M. Morris, "The synaptic plasticity and memory hypothesis: encoding, storage and persistence," *Philosophical Transactions of the Royal Society B:*

Biological Sciences, vol. 369, no. 1633, p. 20130288, Jan. 2014. [Online]. Available: https://doi.org/10.1098/rstb.2013.0288

[80] C. I. Abramson and A. M. Chicas-Mosier, "Learning in plants: Lessons from Mimosa pudica," *Frontiers in Psychology*, vol. 7, no. MAR, pp. 1–9, 2016. [Online]. Available: https://doi.org/10.3389/fpsyg.2016.00417

[81] D.-A. Jirenhed, A. Rasmussen, F. Johansson, and G. Hesslow, "Learned response sequences in cerebellar Purkinje cells," *Proceedings of the National Academy of Sciences*, vol. 114, no. 23, pp. 6127–6132, Jun. 2017. [Online]. Available: https://doi.org/10.1073/pnas.1621132114

[82] D. Rajan, T. Makushok, A. Kalish, L. Acuna, A. Bonville, K. C. Almanza, B. Garibay, E. Tang, M. Voss, A. Lin, K. Barlow, P. Harrigan, M. M. Slabodnick, and W. F. Marshall, "Single-cell analysis of habituation in stentor coeruleus," *Current Biology*, vol. 33, no. 2, pp. 241–251, 2023. [Online]. Available: https://doi.org/10.1016/j.cub.2022.11.010

[83] P. T. Martin and D. E. Koshland, "Regulation of neurosecretory habituation in pc12 cells: parallel pathways used by camp and calcium." *Proceedings of the National Academy of Sciences*, vol. 89, no. 21, pp. 10 257–10 261, 1992. [Online]. Available: https://doi.org/10.1073/pnas.89.21.10257

[84] J. R. Keath and E. W. Westhead, "Factors affecting habituation of PC12 cells to ATP," *European Journal of Biochemistry*, vol. 271, no. 20, pp. 4034–4041, 2004. [Online]. Available: https://doi.org/10.1111/j.1432-1033.2004.04341.x

[85] J. Staddon and J. Higa, "Multiple time scales in simple habituation." *Psychological Review*, vol. 103, no. 4, pp. 720–733, 1996. [Online]. Available: https://doi.org/10.1037/0033-295X.103.4.720

[86] E. del Rosal, L. Alonso, R. Moreno, M. Vázquez, and J. Santacreu, "Simulation of habituation to simple and multiple stimuli," *Behav. Processes*, vol. 73, no. 3, pp. 272–277, 2006. [Online]. Available: https://doi.org/10.1016/j.beproc.2006.06.007

[87] M. Bonzanni, N. Rouleau, M. Levin, and D. L. Kaplan, "On the Generalization of Habituation: How Discrete Biological Systems Respond to Repetitive Stimuli: A Novel Model of Habituation That Is Independent of Any Biological System,"

BioEssays, vol. 41, no. 7, pp. 1–8, 2019. [Online]. Available: https://doi.org/10.1002/bies.201900028

[88] D. C. Wood, "Habituation in Stentor: a response-dependent process," *Journal of Neuroscience*, vol. 8, no. 7, pp. 2248–2253, Jul. 1988. [Online]. Available: https://doi.org/10.1523/JNEUROSCI.08-07-02248.1988

[89] P. M. Groves and R. F. Thompson, "Habituation: A dual-process theory," *Psychological Review*, vol. 77, no. 5, pp. 419–450, 1970. [Online]. Available: https://doi.org/10.1037/h0029810

[90] E. N. Sokolov, *The central nervous system and behavior III: Neuronal models and the orienting influence*. Macy foundation, New York, 1960. [Online]. Available: https://wellcomecollection.org/works/u3u9uwvc

[91] A. R. Wagner, *Habituation and memory. Mechanisms of learning and motivation: A memorial volume for Jerzy Konorski*. Erlbaum Hillsdale, NJ, 1979. [Online]. Available: https://doi.org/10.4324/9781315802435

[92] E. Ahissar and M. Zacksenhouse, "Chapter 6 Temporal and spatial coding in the rat vibrissal system," in *Progress in Brain Research*, ser. Advances in Neural Population Coding. Elsevier, Jan. 2001, vol. 130, pp. 75–87. [Online]. Available: https://doi.org/10.1016/S0079-6123(01)30007-9

[93] I. Tagkopoulos, Y.-C. Liu, and S. Tavazoie, "Predictive Behavior Within Microbial Genetic Networks," *Science*, vol. 320, no. 5881, pp. 1313–1317, Jun. 2008. [Online]. Available: https://doi.org/10.1126/science.1154456

[94] S. Schild, R. Tamayo, E. J. Nelson, F. Qadri, S. B. Calderwood, and A. Camilli, "Genes Induced Late in Infection Increase Fitness of Vibrio cholerae after Release into the Environment," *Cell Host & Microbe*, vol. 2, no. 4, pp. 264–277, Oct. 2007. [Online]. Available: https://doi.org/10.1016/j.chom.2007.09.004

[95] D. M. Wolf, L. Fontaine-Bodin, I. Bischofs, G. Price, J. Keasling, and A. P. Arkin, "Memory in Microbes: Quantifying History-Dependent Behavior in a Bacterium," *PLOS ONE*, vol. 3, no. 2, p. e1700, Feb. 2008. [Online]. Available: https://doi.org/10.1371/journal.pone.0001700

[96] T. I. Lee, N. J. Rinaldi, F. Robert, D. T. Odom, Z. Bar-Joseph, G. K. Gerber, N. M. Hannett, C. T. Harbison, C. M. Thompson, I. Simon, J. Zeitlinger, E. G. Jennings, H. L. Murray, D. B. Gordon, B. Ren, J. J. Wyrick, J.-B. Tagne, T. L. Volkert, E. Fraenkel, D. K. Gifford, and R. A. Young, "Transcriptional Regulatory Networks in Saccharomyces cerevisiae," *Science*, vol. 298, no. 5594, pp. 799–804, Oct. 2002. [Online]. Available: https://doi.org/10.1126/science.1075090

[97] A. Martinez-Antonio and J. Collado-Vides, "Identifying global regulators in transcriptional regulatory networks in bacteria," *Current Opinion in Microbiology*, vol. 6, no. 5, pp. 482–489, Oct. 2003. [Online]. Available: https://doi.org/10.1016/j.mib.2003.09.002

[98] B. Jones, D. Stekel, J. Rowe, and C. Fernando, "Is there a Liquid State Machine in the Bacterium Escherichia Coli?" in *2007 IEEE Symposium on Artificial Life*, Apr. 2007, pp. 187–191. [Online]. Available: https://doi.org/10.1109/ALIFE.2007.367795

[99] M. Gabalda-Sagarra, L. B. Carey, and J. Garcia-Ojalvo, "Recurrence-based information processing in gene regulatory networks," *Chaos: An Interdisciplinary Journal of Nonlinear Science*, vol. 28, no. 10, p. 106313, Oct. 2018. [Online]. Available: https://doi.org/10.1063/1.5039861

[100] H. Jaeger, *The 'echo state' approach to analysing and training recurrent neural networks*. GMD Forschungszentrum Informationstechnik, 2001. [Online]. Available: https://publica.fraunhofer.de/handle/publica/291111

[101] I. M. Keseler, J. Collado-Vides, A. Santos-Zavaleta, M. Peralta-Gil, S. Gama-Castro, L. Muñiz-Rascado, C. Bonavides-Martinez, S. Paley, M. Krummenacker, T. Altman, P. Kaipa, A. Spaulding, J. Pacheco, M. Latendresse, C. Fulcher, M. Sarker, A. G. Shearer, A. Mackie, I. Paulsen, R. P. Gunsalus, and P. D. Karp, "EcoCyc: a comprehensive database of Escherichia coli biology," *Nucleic Acids Research*, vol. 39, no. suppl_1, pp. D583–D590, Jan. 2011. [Online]. Available: https://doi.org/10.1093/nar/gkq1143

[102] H. Jaeger and H. Haas, "Harnessing Nonlinearity: Predicting Chaotic Systems and Saving Energy in Wireless Communication," *Science*, vol. 304, no. 5667, pp. 78–80, Apr. 2004. [Online]. Available: https://doi.org/10.1126/science.1091277

[103] F. Triefenbach, A. Jalalvand, B. Schrauwen, and J.-p. Martens, "Phoneme recognition with large hierarchical reservoirs," in *Advances in Neural Information Processing Systems*, J. Lafferty, C. Williams, J. Shawe-Taylor, R. Zemel, and A. Culotta, Eds., vol. 23. Curran Associates, Inc., 2010. [Online]. Available: https://dl.acm.org/doi/abs/10.5555/2997046.2997153

[104] D. Verstraeten, B. Schrauwen, and D. Stroobandt, "Reservoir-based techniques for speech recognition," *The 2006 IEEE International Joint Conference on Neural Network Proceedings*, pp. 1050–1053, 2006. [Online]. Available: https://doi.org/10.1109/IJCNN.2006.246804

[105] A. Rodan and P. Tino, "Minimum Complexity Echo State Network," *IEEE Transactions on Neural Networks*, vol. 22, no. 1, pp. 131–144, Jan. 2011. [Online]. Available: https://doi.org/10.1109/TNN.2010.2089641

[106] F. Wyffels, B. Schrauwen, and D. Stroobandt, "Stable Output Feedback in Reservoir Computing Using Ridge Regression," in *Artificial Neural Networks - ICANN 2008*, ser. Lecture Notes in Computer Science, V. Kůrková, R. Neruda, and J. Koutník, Eds. Berlin, Heidelberg: Springer, 2008, pp. 808–817. [Online]. Available: https://doi.org/10.1007/978-3-540-87536-9_83

[107] R. Legenstein and W. Maass, "Edge of chaos and prediction of computational performance for neural circuit models," *Neural Networks*, vol. 20, no. 3, pp. 323–334, Apr. 2007. [Online]. Available: https://doi.org/10.1016/j.neunet.2007.04.017

[108] J. M. Beggs, "The criticality hypothesis: how local cortical networks might optimize information processing," *Philosophical Transactions of the Royal Society A: Mathematical, Physical and Engineering Sciences*, vol. 366, no. 1864, pp. 329–343, Aug. 2007. [Online]. Available: https://doi.org/10.1098/rsta.2007.2092

[109] J. M. Beggs and D. Plenz, "Neuronal Avalanches in Neocortical Circuits," *Journal of Neuroscience*, vol. 23, no. 35, pp. 11 167–11 177, Dec. 2003. [Online]. Available: https://doi.org/10.1523/JNEUROSCI.23-35-11167.2003

[110] D. R. Chialvo, "Critical brain networks," *Physica A: Statistical Mechanics and its Applications*, vol. 340, no. 4, pp. 756–765, Sep. 2004. [Online]. Available: https://doi.org/10.1016/j.physa.2004.05.064

[111] I. B. Yildiz, H. Jaeger, and S. J. Kiebel, "Re-visiting the echo state property," *Neural Networks*, vol. 35, pp. 1–9, Nov. 2012. [Online]. Available: https://doi.org/10.1016/j.neunet.2012.07.005

[112] N. Bertschinger and T. Natschläger, "Real-Time Computation at the Edge of Chaos in Recurrent Neural Networks," *Neural Computation*, vol. 16, no. 7, pp. 1413–1436, Jul. 2004. [Online]. Available: https://doi.org/10.1162/089976604323057443

[113] J. Boedecker, O. Obst, J. T. Lizier, N. M. Mayer, and M. Asada, "Information processing in echo state networks at the edge of chaos," *Theory in Biosciences*, vol. 131, no. 3, pp. 205–213, Sep. 2012. [Online]. Available: https://doi.org/10.1007/s12064-011-0146-8

[114] B. Derrida and Y. Pomeau, "Random Networks of Automata: A Simple Annealed Approximation," *Europhysics Letters*, vol. 1, no. 2, p. 45, Jan. 1986. [Online]. Available: https://dx.doi.org/10.1209/0295-5075/1/2/001

[115] R. Milo, S. Shen-Orr, S. Itzkovitz, N. Kashtan, D. Chklovskii, and U. Alon, "Network Motifs: Simple Building Blocks of Complex Networks," *Science*, vol. 298, no. 5594, pp. 824–827, Oct. 2002. [Online]. Available: https://doi.org/10.1126/science.298.5594.824

[116] S. S. Shen-Orr, R. Milo, S. Mangan, and U. Alon, "Network motifs in the transcriptional regulation network of Escherichia coli," *Nature Genetics*, vol. 31, no. 1, pp. 64–68, May 2002. [Online]. Available: https://doi.org/10.1038/ng881

[117] G. Deco, A. Ponce-Alvarez, P. Hagmann, G. L. Romani, D. Mantini, and M. Corbetta, "How Local Excitation–Inhibition Ratio Impacts the Whole Brain Dynamics," *Journal of Neuroscience*, vol. 34, no. 23, pp. 7886–7898, Jun. 2014. [Online]. Available: https://doi.org/10.1523/JNEUROSCI.5068-13.2014

[118] S. Ghatak, M. Talantova, S. R. McKercher, and S. A. Lipton, "Novel Therapeutic Approach for Excitatory/Inhibitory Imbalance in Neurodevelopmental and Neurodegenerative Diseases," *Annual Review of Pharmacology and Toxicology*, vol. 61, no. 1, pp. 701–721, 2021. [Online]. Available: https://doi.org/10.1146/annurev-pharmtox-032320-015420

[119] S. Kirischuk, "Keeping Excitation–Inhibition Ratio in Balance," *International Journal of Molecular Sciences*, vol. 23, no. 10, p. 5746, Jan. 2022. [Online]. Available: https://doi.org/10.3390/ijms23105746

[120] H. Jaeger, "Adaptive Nonlinear System Identification with Echo State Networks," in *Advances in Neural Information Processing Systems*, vol. 15. MIT Press, 2002. [Online]. Available: https://proceedings.neurips.cc/paper/2002/hash/426f990b332ef8193a61cc90516c1245-Abstract.html

[121] A. Atiya and A. Parlos, "New results on recurrent network training: unifying the algorithms and accelerating convergence," *IEEE Transactions on Neural Networks*, vol. 11, no. 3, pp. 697–709, May 2000. [Online]. Available: https://doi.org/10.1109/72.846741

[122] G. B. Morales and M. A. Muñoz, "Optimal input representation in neural systems at the edge of chaos," *Biology*, vol. 10, no. 8, p. 702, Jul. 2021. [Online]. Available: http://dx.doi.org/10.3390/biology10080702

[123] M. A. Casal, S. Galella, O. Vilarroya, and J. Garcia-Ojalvo, "Soft-wired long-term memory in a natural recurrent neuronal network," *Chaos: An Interdisciplinary Journal of Nonlinear Science*, vol. 30, no. 6, Jun. 2020. [Online]. Available: http://dx.doi.org/10.1063/5.0009709

[124] T. Fukushi and R. Wehner, "Navigation in wood ants formica japonica: context dependent use of landmarks," *Journal of Experimental Biology*, vol. 207, no. 19, pp. 3431–3439, 2004. [Online]. Available: https://doi.org/10.1242/jeb.01159

[125] C. T. Hemingway, M. J. Ryan, and R. A. Page, "State-dependent learning influences foraging behaviour in an acoustic predator," *Animal behaviour*, vol. 163, pp. 33–38, 2020. [Online]. Available: https://doi.org/10.1016/j.anbehav.2020.02.004

[126] J. Luo and D. S. Portman, "Sex-specific, pdfr-1-dependent modulation of pheromone avoidance by food abundance enables flexibility in c. elegans foraging behavior," *Current Biology*, vol. 31, no. 20, pp. 4449–4461, 2021. [Online]. Available: https://doi.org/10.1016/j.cub.2021.07.069

[127] S. Brenner, "The genetics of caenorhabditis elegans," *Genetics*, vol. 77, no. 1, pp. 71–94, 1974. [Online]. Available: https://doi.org/10.1093/g3journal/jkad111

[128] L. Byerly, R. Cassada, and R. Russell, "The life cycle of the nematode caenorhabditis elegans: I. wild-type growth and reproduction," *Developmental biology*, vol. 51, no. 1, pp. 23–33, 1976. [Online]. Available: https://doi.org/10.1016/0012-1606(76)90119-6

[129] R. M. Durbin, "Studies on the development and organisation of the nervous system of caenorhabditis elegans," 1987. [Online]. Available: https://www.wormatlas.org/Durbin/Durbin1987partII.html

[130] M. d. Bono and A. Villu Maricq, "Neuronal substrates of complex behaviors in c. elegans," *Annu. Rev. Neurosci.*, vol. 28, pp. 451–501, 2005. [Online]. Available: https://doi.org/10.1146/annurev.neuro.27.070203.144259

[131] P. Sengupta and A. D. Samuel, "Caenorhabditis elegans: a model system for systems neuroscience," *Current opinion in neurobiology*, vol. 19, no. 6, pp. 637–643, 2009. [Online]. Available: https://doi.org/10.1016/j.conb.2009.09.009

[132] H. Ohno, N. Sakai, T. Adachi, and Y. Iino, "Dynamics of presynaptic diacylglycerol in a sensory neuron encode differences between past and current stimulus intensity," *Cell reports*, vol. 20, no. 10, pp. 2294–2303, 2017. [Online]. Available: https://doi.org/10.1016/j.celrep.2017.08.038

[133] H. Sato, H. Kunitomo, X. Fei, K. Hashimoto, and Y. Iino, "Glutamate signaling from a single sensory neuron mediates experience-dependent bidirectional behavior in caenorhabditis elegans," *Cell Reports*, vol. 35, no. 8, p. 109177, 2021. [Online]. Available: https://doi.org/10.1016/j.celrep.2021.109177

[134] S. Hiroki, H. Yoshitane, H. Mitsui, H. Sato, C. Umatani, S. Kanda, Y. Fukada, and Y. Iino, "Molecular encoding and synaptic decoding of context during salt chemotaxis in c. elegans," *Nature Communications*, vol. 13, no. 1, pp. 1–15, 2022. [Online]. Available: https://doi.org/10.1038/s41467-022-30279-7

[135] L. Luo, Q. Wen, J. Ren, M. Hendricks, M. Gershow, Y. Qin, J. Greenwood, E. R. Soucy, M. Klein, H. K. Smith-Parker *et al.*, "Dynamic encoding of perception, memory, and movement in a c. elegans chemotaxis circuit," *Neuron*, vol. 82, no. 5, pp. 1115–1128, 2014. [Online]. Available: https://doi.org/10.1016/j.neuron.2014.05.010

[136] T. Wakabayashi, I. Kitagawa, and R. Shingai, "Neurons regulating the duration of forward locomotion in caenorhabditis elegans," *Neuroscience research*, vol. 50, no. 1, pp. 103–111, 2004. [Online]. Available: https://doi.org/10.1016/j.neures.2004.06.005

[137] P. A. Garrity, M. B. Goodman, A. D. Samuel, and P. Sengupta, "Running hot and cold: behavioral strategies, neural circuits, and the

molecular machinery for thermotaxis in c. elegans and drosophila," *Genes & development*, vol. 24, no. 21, pp. 2365–2382, 2010. [Online]. Available: https://doi.org/10.1101/gad.1953710

[138] Y. Iino and K. Yoshida, "Parallel use of two behavioral mechanisms for chemotaxis in caenorhabditis elegans," *Journal of Neuroscience*, vol. 29, no. 17, pp. 5370–5380, 2009. [Online]. Available: https://doi.org/10.1523/JNEUROSCI.3633-08.2009

[139] E. J. Izquierdo and R. D. Beer, "The whole worm: brain–body–environment models of c. elegans," *Current Opinion in Neurobiology*, vol. 40, pp. 23–30, 2016. [Online]. Available: https://doi.org/10.1016/j.conb.2016.06.005

[140] H. Suzuki, T. R. Thiele, S. Faumont, M. Ezcurra, S. R. Lockery, and W. R. Schafer, "Functional asymmetry in caenorhabditis elegans taste neurons and its computational role in chemotaxis," *Nature*, vol. 454, no. 7200, pp. 114–117, 2008. [Online]. Available: https://doi.org/10.1038/nature06927

[141] M. P. Dekkers, F. Salfelder, T. Sanders, O. Umuerri, N. Cohen, and G. Jansen, "Plasticity in gustatory and nociceptive neurons controls decision making in c. elegans salt navigation," *Communications biology*, vol. 4, no. 1, pp. 1–14, 2021. [Online]. Available: https://doi.org/10.1038/s42003-021-02561-9

[142] M. Adler and U. Alon, "Fold-change detection in biological systems," *Current Opinion in Systems Biology*, vol. 8, pp. 81–89, 2018. [Online]. Available: https://doi.org/10.1016/j.coisb.2017.12.005

[143] D. M. Ferkey, P. Sengupta, and N. D. L'Etoile, "Chemosensory signal transduction in caenorhabditis elegans," *Genetics*, vol. 217, no. 3, p. iyab004, 2021. [Online]. Available: https://doi.org/10.1093/genetics/iyab004

[144] D. Ventimiglia and C. I. Bargmann, "Diverse modes of synaptic signaling, regulation, and plasticity distinguish two classes of c. elegans glutamatergic neurons," *Elife*, vol. 6, p. e31234, 2017. [Online]. Available: https://doi.org/10.7554/eLife.31234

[145] A. Narayan, G. Laurent, and P. W. Sternberg, "Transfer characteristics of a thermosensory synapse in caenorhabditis elegans," *Proceedings of the National Academy of Sciences*, vol. 108, no. 23, pp. 9667–9672, 2011. [Online]. Available: https://doi.org/10.1073/pnas.1106617108

[146] T. H. Lindsay, T. R. Thiele, and S. R. Lockery, "Optogenetic analysis of synaptic transmission in the central nervous system of the nematode caenorhabditis elegans," *Nature communications*, vol. 2, no. 1, pp. 1–9, 2011. [Online]. Available: https://doi.org/10.1038/ncomms1304

[147] M. Usuyama, C. Ushida, and R. Shingai, "A model of the intracellular response of an olfactory neuron in caenorhabditis elegans to odor stimulation," *PLoS ONE*, vol. 7, no. 8, p. e42907, Aug. 2012. [Online]. Available: http://dx.doi.org/10.1371/journal.pone.0042907

[148] E. Mirzakhalili, B. I. Epureanu, and E. Gourgou, "A mathematical and computational model of the calcium dynamics in caenorhabditis elegans ash sensory neuron," *PloS one*, vol. 13, no. 7, p. e0201302, 2018. [Online]. Available: https://doi.org/10.1371/journal.pone.0201302

[149] S. Woldemariam, J. Nagpal, T. Hill, J. Li, M. W. Schneider, R. Shankar, M. Futey, A. Varshney, N. Ali, J. Mitchell, K. Andersen, B. Barsi-Rhyne, A. Tran, W. S. Costa, M. C. Krzyzanowski, Y. V. Yu, C. Brueggemann, O. S. Hamilton, D. M. Ferkey, M. VanHoven, P. Sengupta, A. Gottschalk, and N. L'Etoile, "Using a robust and sensitive gfp-based cgmp sensor for real-time imaging in intact caenorhabditis elegans," *Genetics*, vol. 213, no. 1, p. 59–77, Sep. 2019. [Online]. Available: http://dx.doi.org/10.1534/genetics.119.302392

[150] M. Eigenthaler, C. Nolte, M. Halbrugge, and U. Walter, "Concentration and regulation of cyclic nucleotides, cyclic-nucleotide-dependent protein kinases and one of their major substrates in human platelets. estimating the rate of camp-regulated and cgmp-regulated protein phosphorylation in intact cells," *European Journal of Biochemistry*, vol. 205, no. 2, p. 471–481, Apr. 1992. [Online]. Available: http://dx.doi.org/10.1111/j.1432-1033.1992.tb16803.x

[151] A. D. Samuel, V. N. Murthy, and M. O. Hengartner, "Calcium dynamics during fertilization in c. elegans," *BMC Developmental Biology*, vol. 1, no. 1, Apr. 2001. [Online]. Available: http://dx.doi.org/10.1186/1471-213X-1-8

[152] H. Schoeny, E. Rampler, D. Binh Chu, A. Schoeberl, L. Galvez, M. Blaukopf, P. Kosma, and G. Koellensperger, "Achieving absolute molar lipid concentrations: A phospholipidomics cross-validation study," *Analytical Chemistry*, vol. 94, no. 3, p. 1618–1625, Jan.

2022. [Online]. Available: http://dx.doi.org/10.1021/acs.analchem.1c03743

[153] R. D. Blakely and R. H. Edwards, "Vesicular and plasma membrane transporters for neurotransmitters," *Cold Spring Harbor Perspectives in Biology*, vol. 4, no. 2, p. a005595–a005595, Dec. 2011. [Online]. Available: http://dx.doi.org/10.1101/cshperspect.a005595

[154] J. T. Pierce-Shimomura, T. M. Morse, and S. R. Lockery, "The fundamental role of pirouettes in caenorhabditis elegans chemotaxis," *Journal of Neuroscience*, vol. 19, no. 21, pp. 9557–9569, 1999. [Online]. Available: https://doi.org/10.1523/jneurosci.19-21-09557.1999

[155] Y. Okochi, K. D. Kimura, A. Ohta, and I. Mori, "Diverse regulation of sensory signaling by c. elegans npkc-epsilon/eta ttx-4," *The EMBO journal*, vol. 24, no. 12, pp. 2127–2137, 2005. [Online]. Available: https://doi.org/10.1038/sj.emboj.7600697

[156] M. Tsunozaki, S. H. Chalasani, and C. I. Bargmann, "A behavioral switch: cgmp and pkc signaling in olfactory neurons reverses odor preference in c. elegans," *Neuron*, vol. 59, no. 6, pp. 959–971, 2008. [Online]. Available: https://doi.org/10.1016/j.neuron.2008.07.038

[157] A. Rahmani and Y. L. Chew, "Investigating the molecular mechanisms of learning and memory using caenorhabditis elegans," *Journal of Neurochemistry*, vol. 159, no. 3, pp. 417–451, 2021. [Online]. Available: https://doi.org/10.1111/jnc.15510

[158] M. Fenckova, L. E. R. Blok, L. Asztalos, D. P. Goodman, P. Cizek, E. L. Singgih, J. C. Glennon, J. IntHout, C. Zweier, E. E. Eichler, C. R. v. Reyn, R. A. Bernier, Z. Asztalos, and A. Schenck, "Habituation Learning Is a Widely Affected Mechanism in Drosophila Models of Intellectual Disability and Autism Spectrum Disorders," *Biological Psychiatry*, vol. 86, no. 4, pp. 294–305, Aug. 2019. [Online]. Available: https://doi.org/10.1016/j.biopsych.2019.04.029

[159] S. J. Rahi, J. Larsch, K. Pecani, A. Y. Katsov, N. Mansouri, K. Tsaneva-Atanasova, E. D. Sontag, and F. R. Cross, "Oscillatory stimuli differentiate adapting circuit topologies," *Nature Methods*, vol. 14, no. 10, pp. 1010–1016, Oct. 2017. [Online]. Available: https://doi.org/10.1038/nmeth.4408

[160] L. Büsing, B. Schrauwen, and R. Legenstein, "Connectivity, Dynamics, and Memory in Reservoir Computing with Binary

and Analog Neurons," *Neural Computation*, vol. 22, no. 5, pp. 1272–1311, May 2010. [Online]. Available: https://doi.org/10.1162/neco.2009.01-09-947

[161] J. Dambre, D. Verstraeten, B. Schrauwen, and S. Massar, "Information Processing Capacity of Dynamical Systems," *Scientific Reports*, vol. 2, no. 1, p. 514, Jul. 2012. [Online]. Available: https://doi.org/10.1038/srep00514

[162] G. Tanaka, T. Yamane, J. B. Héroux, R. Nakane, N. Kanazawa, S. Takeda, H. Numata, D. Nakano, and A. Hirose, "Recent advances in physical reservoir computing: A review," *Neural Networks*, vol. 115, pp. 100–123, Jul. 2019. [Online]. Available: https://doi.org/10.1016/j.neunet.2019.03.005

[163] P. Virtanen, R. Gommers, T. E. Oliphant, M. Haberland, T. Reddy, D. Cournapeau, E. Burovski, P. Peterson, W. Weckesser, J. Bright, S. J. van der Walt, M. Brett, J. Wilson, K. J. Millman, N. Mayorov, A. R. J. Nelson, E. Jones, R. Kern, E. Larson, C. J. Carey, İ. Polat, Y. Feng, E. W. Moore, J. VanderPlas, D. Laxalde, J. Perktold, R. Cimrman, I. Henriksen, E. A. Quintero, C. R. Harris, A. M. Archibald, A. H. Ribeiro, F. Pedregosa, P. van Mulbregt, and SciPy 1.0 Contributors, "SciPy 1.0: Fundamental Algorithms for Scientific Computing in Python," *Nature Methods*, vol. 17, pp. 261–272, 2020. [Online]. Available: https://doi.org/10.1038/s41592-019-0686-2

[164] K. Ahnert and M. Mulansky, "Odeint – Solving Ordinary Differential Equations in C++," *AIP Conference Proceedings*, vol. 1389, no. 1, pp. 1586–1589, Sep. 2011. [Online]. Available: https://doi.org/10.1063/1.3637934

[165] M. Keijzer, J. J. Merelo, G. Romero, and M. Schoenauer, "Evolving Objects: A General Purpose Evolutionary Computation Library," in *Artificial Evolution*, ser. Lecture Notes in Computer Science, P. Collet, C. Fonlupt, J.-K. Hao, E. Lutton, and M. Schoenauer, Eds. Berlin, Heidelberg: Springer, 2002, pp. 231–242. [Online]. Available: https://doi.org/10.1007/3-540-46033-0_19

[166] J. Dreo, A. Liefooghe, S. Verel, M. Schoenauer, J. J. Merelo, A. Quemy, B. Bouvier, and J. Gmys, "Paradiseo: From a modular framework for evolutionary computation to the automated design of metaheuristics: 22 years of paradiseo," in *Proceedings of the Genetic and Evolutionary Computation Conference Companion*. New York, NY, USA: Association for Computing Machinery, 2021,

p. 1522–1530. [Online]. Available: https://doi.org/10.1145/3449726. 3463276

[167] M. Schoenauer. Tutorial lesson 4: ready-to-use fully operational ea - esea. [Online]. Available: https://eodev.sourceforge.net/eo/tutorial/ html/eoLesson4.html

[168] J. C. Sprott, *Chaos and time-series analysis*. London, England: Oxford University Press, Feb. 2003. [Online]. Available: https: //doi.org/10.5860/choice.41-3492